Soft Particle Model for Diblock Copolymers

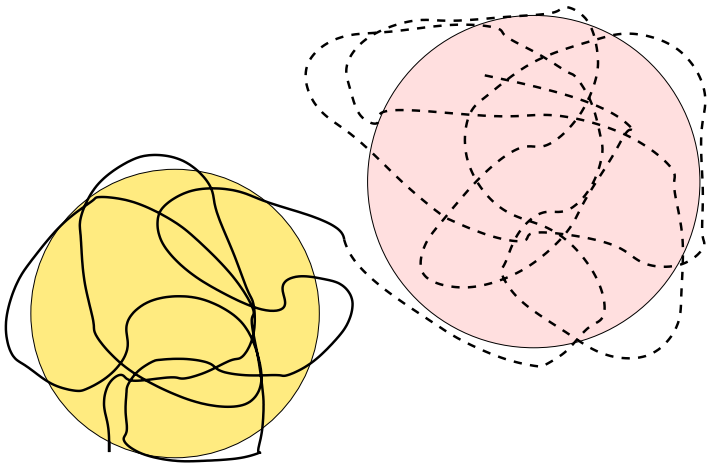

Dissertation
zur Erlangung des akademischen Grades
des Doktors der Naturwissenschaften (Dr. rer. nat.)
an der Universität Konstanz
Fachbereich Physik

vorgelegt von

Alexei Karatchentsev

Tag der mündlichen Prüfung: 8. Juni 2009
Referent: Prof. Dr. Philipp Maaß
Referent: Prof. Dr. Georg Maret

Konstanzer Online-Publikations-System (KOPS)
URN: http://nbn-resolving.de/urn:nbn:de:bsz:352-opus-81629
URL: http://kops.ub.uni-konstanz.de/volltexte/2009/8162/

Zusammenfassung

In vielen Bereichen der statistischen Physik werden vergröberte Modelle verwendet, mit deren Hilfe man versucht, wesentliche Eigenschaften der Systeme mit einer reduzierten Anzahl an Parametern zu beschreiben. Untersucht man die Entmischungskinetik in einer dichten binären Mischung von langkettigen Polymeren, so ist die Bewegung der einzelnen Monomere, die auf mikropischen Zeit- und Längenskalen stattfindet, für den Gesamtvorgang weitgehend irrelevant. In den gängigen numerischen Simulationsverfahren bilden jedoch die elementaren mikroskopischen Bewegungsschritte den Ausgangspunkt, so dass der Vorstoß zu den eigentlich interessierenden räumlichen und zeitlichen Strukturen unter Umständen jeden vertretbaren Rechenaufwand übersteigt.

Dabei ist ein detailiertes Verständnis für Entmischungsprozesse vom großem Interesse, da Polymere eine zunehmende Rolle in der Mikroelektronik bei der Herstellung kleiner Strukturen mit Hilfe der polymeren Lithographie spielen. Einige Beispiele findet man bei der Produktion von mikroskopischen Schaltkreisen, Speicherkarten und Siliziumkondensatoren. Ionenleitende Polymere mit polaren Grundmolekülen wendet man als feste Elektrolyte in wiederaufladbaren Lithium-Polymer Batterien an. Weitere Möglichkeiten bieten Diblockcopolymere an. Die chemische Bindung zwischen den beiden Blöcken solcher Moleküle verhindert Entmischung der beiden Komponenten bei tiefen Temperaturen und führt zur Entstehung von geordneten Mikrostrukturen wie Sphären, Zylinder und Lamellen, deren Form und Dimensionen man leicht durch das Molekülgewicht und die Komposition kontrollieren kann. Auf Oberflächen mit einem entsprechenden periodischen Muster bilden solche Strukturen dünne Filme mit weitreichender Ordnung, die weiterhin als lithographische Masken benutzt werden können.

Der Hauptteil dieser Arbeit befasst sich mit der Entwicklung eines Modells weicher, d.h. durchdringungsfähiger Teilchen für Diblockcopolymere, das von F. Eurich vorgeschlagen wurde [Eudiss]. In dieser Beschreibung wird das Molekül auf zwei sich durchdringende sphärische Teilchen mit fluktuierenden Gyrationsradien und Abstandvektor zwischen ihren Mittelpunkten abgebildet. Dieses Modell ist in der Lage, polymere Eigenschaften auf Längen– und Zeitskalen gleich oder größer als der Gyrationsradius R_G und die Diffusionszeit $\tau_D \simeq R_G^2/D$ zu beschreiben, wobei D den Diffusionskoeffizient der Moleküle bezeichnet.

Die notwendigen mikroskopischen Eingangsgrößen für das Modell sind Wahrscheinlichkeitsverteilungen für die Gyrationsradien und die Abstände der Massenmittelpunke sowie bedingte Monomerdichten für die beiden Blöcke A und B. Diese Verteilungen sind aus einem zu Grunde liegenden mikroskopischen Kettenmodel zu bestimmen. Der Arbeit von Eurich [Eudiss] folgend wird das Modell Gauß'scher Ketten benutzt. Der Vorteil besteht in einfachen analytischen Ausdrücken für die geforderten Eingangsgrößen; "Excluded Volume" Effekte lassen sich im Rahmen einer Mean-field Theorie beruecksichtigen. Das Modell beschreibt korrekt dichte polymere Schmelzen, die auch in dieser Arbeit untersucht werden. Um die Kinetik des Ensembles weicher Teilchen zu verfolgen, wird ein Monte-Carlo Algorithmus eingesetzt. Die hierbei verwendete Freie Energie des Systems ist dementsprechend von den Gyrationsradien und

Massenmittelpunkabständen der einzelnen Teilchen abhängig und wird in einen intramolekularen und einen intermolekularen Anteil zerlegt. Der intramolekulare Anteil ist durch die inneren Freiheitsgrade definiert; der intermolekulare Anteil enthält das Überlappintegral der Monomerdichten.

Zuerst verwenden wir das Modell zur Beschreibung dichter Schmelzen von Diblockcopolymeren im freien Raum. Es zeigt sich, dass der Strukturfaktor, der Fluktuationen der Monomerdichte einer der Komponenten widerspiegelt, in der ungeordneten Schmelze gut durch einen modifizierten Strukturfaktor nach Leibler [Kar07] dargestellt wird. Bei höheren Werten des Wechselwirkungsparameters χ zwischen den beiden Komponenten werden die lamellare Phase für die symmetrische Komposition sowie die zylindrische und die bcc-Phase bei asymmetrischen Kompositionen gefunden. Weiterhin finden wir, dass die lamellare Periode λ bei starker Segregation mit χ und dem Polymerisationsgrad N als $\lambda/N^{0.5} \sim (\chi N)^n$ skaliert, wobei der Exponent $n = 0.22$ etwas höher ist als die theoretische Vorhersage $n = 1/6$ [Bin94]. Die Gauß'sche Skalierung $\lambda \sim N^{0.5}$ gilt bei schwacher Segregation. Das Modell wird zusätzlich bezüglich der Diffusionseigenschaften der Moleküle beim Durchgang durch den Ordnung-Unordnung Übergang geprüft; theoretische Ergebnisse [Bar91] sowie Simulationsuntersuchungen [Hof97a] werden bestätigt.

Als nächstes wird die Bildung von Mikrostrukturen in eingeschränkten Geometrien beschrieben. Es zeigt sich, dass die parallele Orientierung der Teilchen in der Nähe von planaren und hinsichtlich der Wechselwirkung mit den A- und B-Komponenten neutralen Wänden lokal geordnete senkrechte Lamellen erzeugt [Kar07]. Im Fall homogener Wände, die eine der Komponenten bevorzugen, orientieren sich die Lamellen parallel zu den Wänden. Ist die Wand mit einem Streifenmuster der Periode L_p strukturiert, welches die A- und B-Komponenten abwechselnd bevorzugt, so bilden sich senkrechte, global geordnete Lamellen.

Berechnungen des zeitabhängigen lateralen Strukturfaktors liefern detaillierte Vorhersagen über den Verlauf der Strukturbildung. So wird gezeigt, wie der Strukturtransfer vom Substrat her von der spontanen Strukturbildung in der Mitte des Films beeinflusst wird. Falls die Periode L_p mit der lamellaren Periode λ übereinstimmt, wird die spontane Strukturbildung von den global geordneten senkrechten Lamellen völlig unterdrückt. Sind die beiden Perioden inkommensurabel, so koennen sich unterschiedliche stabile Strukturen im Gleichgewicht ausbilden: senkrechte Lamellen mit der Periode L_p unweit des Substrates und lokal geordnete senkrechte Lamellen mit der Periode λ im Rest des Filmes.

Schließlich wird die Tracerdiffusion durch Polymere untersucht, die als dynamisch ungeordnetes Netzwerk aufgefasst werden. Die Tracerbewegung und die Reorganisation des Netzwerks finden auf gleicher Zeitskala statt. Dennoch erweist es sich als möglich, einen weiteren Vergröberungsschritt in die Modellierung einzuführen. Hierzu wird die dynamische Perkolationstheorie (DP) [Dru85] herangezogen. Es bietet sich an, die Idee von Duerr et al. [Dür02] aufzugreifen, indem man das komplizierte Problem in zwei einfachere Teilprobleme zerlegt, und zwar *i*) die Tracerbewegung in einem eingefrorenen polymeren Medium und *ii*) die Bestimmung einer Wartezeitverteilung für die Reorganisation des Netzwerks aus den lokalen Fluktuationen der Polymerdichte in der Nähe eines festgehaltenen Tracers.

Unter Verwendung des Algorithmus von Verdier-Stockmayer haben diese Autoren gezeigt, dass der Tracer-Korrelationsfaktor, berechnet in der DP-Theorie, gut mit dem Ergebnis von Simulationen des Gesamtsystems übereinstimmt. In der vorliegenden Arbeit wird der "Fluctuation site-bond" Algorithmus (FSB) [Schu05] verwendet. Mit dessen Hilfe ist es möglich,

die Polymerdynamik bei sehr hohen Dichten zu beschreiben und somit das DP-Konzept allgemeiner zu testen. Es zeigt sich, dass der Tracer-Korrelationsfaktor bei diesen hohen Dichten zwar stark abgesenkt wird, aber doch noch höher liegt als der aus vollen Simulationen berechnete [Kar06]. Weiterhin wird im zeitabhängigen Diffusionskoeffizienten innerhalb eines intermediaeren Zeitbereichs ein Potenz-Verhalten gefunden, welches sich mit Experimenten an polymeren Elektrolyten [Mar05], [Not02] vergleichen läßt.

Contents

1 Introduction

Polymer materials have become over decades an intriguing field of research due to their distinctive properties which are widely utilized in numerous technological applications. Fabrication of nanoelectronic devices such as nanowires, flash memory cards and silicon capacitors makes use of lithographic technique based on structure formation in blends of incompatible polymers or microphase separation in copolymer melts. Patterning templates used in this technique are made up of thin nanostructured polymer films whose pattern dimensions and shape are easily tuned by the molecular weight and composition of polymers. Another application encountered in lithium-polymer recheargable batteries emloys ion conductive polymers where polymer chains with repeating polar segments function as network enviroment for ionic motion.

A detailed unrderstanding of the physical processes involved is facilitated by the fact that only semi-microscopical length and time scales are relevant in both structure formation and microphase separation, whereas for conductive polymers, the internal degrees of freedom of the chains are irrelative to the ion diffusion. It is therefore conclusive to implement coarse grained models where the irrelevant degrees of freedom are eliminated from the description. Such models are developed and tested in this dissertation.

In the following we present a short introduction into elementary polymer theories and physics of copolymers. The main part of the work deals with processes of structure formation in diblock copolymers with emphasis on its kinetics in thin films which are studied by means of a soft particle model for diblock copolymers. At the end some results are shown concerning ion diffusion in polymer networks.

1.1 Simple Polymer Chain Models

A chain polymer molecule consists of a sequence of repeating units (monomers) of the same or variable type. In the most simple statistical model, one assumes a coarse grained representation of the chain in terms of a sequence of beads connected by bonds such that there is no correlation between bonds connecting adjacent beads of the chain and that all bond directions have the same probability. Clearly, all interactions between chain beads are then neglected. This model of a freely jointed chain is equivalent to an uncorrelated random walk with fixed step length.

In the simplest case, one can consider lattice chains equivalent to a random walk on a regular lattice with the coordination number z [Doi96]. Let us assume that the polymer chain is made up of N successive bond vectors $\vec{r}_n$ $(n = 1, ..., N)$ with $|\vec{r}_n| = b$ and b being the nearest distance between two neighboring sites of the lattice. One can treat the length of the end-to-end vector $\vec{R}$ connecting two ends of the chain as a measure of the extent to which the chain spreads out

$$\vec{R} = \sum_{n=1}^{N} \vec{r}_n \,. \tag{1.1}$$

The average of $\vec{R}$ is zero because the system is isotropic. Therefore, we define the size of the chain as $\langle \vec{R}^2 \rangle^{1/2}$ with

$$\langle \vec{R}^{\,2} \rangle = \sum_{n=1}^{N} \sum_{m=1}^{N} \langle \vec{r}_n \vec{r}_m \rangle \ . \tag{1.2}$$

Bonds of the chains are uncorrelated, therefore $\langle \vec{r}_n \vec{r}_m \rangle = 0$ for $n \neq m$ and

$$\langle \vec{R}^{\,2} \rangle = \sum_{n=1}^{N} \langle \vec{r}_n^{\,2} \rangle = Nb^2 \, . \tag{1.3}$$

Thus, for a polymer chain, the mean size of the molecule $R = \langle \vec{R}^2 \rangle^{1/2} = bN^{1/2}$ is much smaller than the total length of the chain $L = bN$. In other words, the equilibrium state of the chain due to its flexibility corresponds to a randomly shaped coil.

Let us assume that one end of the chain is fixed at the origin and calculate the probability distribution function $P(\vec{R}, N)$ that the end-to-end vector of the chain reaches the value $\vec{R}$ after N successive steps. As the chain beads can only occupy the sites of the regular lattice with the coordination number z, the bond vector of the chain can take with probability $1/z$ a set of possible values $\vec{b}_i$ $(i = 1, ..., z)$. Therefore, to reach the position $\vec{R}$ after N steps, the end-to-end vector at the $(N-1)$th step must coincide with probability $1/z$ with one of the positions $\vec{R} - \vec{b}_i$ so that

$$P(\vec{R}, N) = \frac{1}{z} \sum_{i=1}^{N} P(\vec{R} - \vec{b}_i, N-1) \, . \tag{1.4}$$

For very long chains, $N \gg 1$, we have $|\vec{R}| \gg |\vec{b}_i|$, and $P(\vec{R} - \vec{b}_i, N-1)$ can be expanded as

$$P(\vec{R} - \vec{b}_i, N-1) \simeq P(\vec{R}, N) - \frac{\partial P}{\partial N} - \sum_{\alpha=x,y,z} \frac{\partial P}{\partial R_\alpha} b_{i\alpha} + \sum_{\alpha,\beta=x,y,z} \frac{1}{2} \frac{\partial^2 P}{\partial R_\alpha \partial R_\beta} b_{i\alpha} b_{i\beta} \, , \tag{1.5}$$

where $b_{i\alpha}$, R_α are the cartesian components of $\vec{b}$, $\vec{R}$. Summing (1.5) over i and noting that

$$\sum_{i=1}^{z} b_{i\alpha} = 0 \, , \tag{1.6}$$

$$\sum_{i=1}^{z} b_{i\alpha} b_{i\beta} = \frac{\delta_{\alpha\beta} b^2}{3} \, , \tag{1.7}$$

we obtain finally the following equation for $P(\vec{R}, N)$ from (1.4),

$$\frac{\partial P}{\partial N} = \frac{b^2}{6} \frac{\partial^2 P}{\partial \vec{R}^2} \, . \tag{1.8}$$

The solution of this equation under the condition $P(\vec{R}, N = 0) = \delta(|\vec{R}|)$ is the Gaussian distribution

$$P(\vec{R}, N) = \left(\frac{3}{2\pi N b^2} \right)^{3/2} \exp\left(-\frac{3\vec{R}^2}{2Nb^2} \right) \, , \tag{1.9}$$

where the prefactor $(\frac{3}{2\pi Nb^2})^{3/2}$ is found from the normalization condition $\int d^3R P(\vec{R}, N) = 1$. The first moment of the distribution (1.9) coincides with (1.3)

More complicated off-lattice models of the ideal chain explicitly account for flexibility mechanisms. They take into account "short-range interactions" which occur between neighboring segments along the chain but ignore "long-range interactions" between segments belonging to widely separated parts. However, there is a common general feature of these models that the orientational correlations between the bonds exponentially decay along the chain and become negligible over the persistence length $\tilde{l}$ of the chain

$$\langle \vec{r}_n \vec{r}_m \rangle \simeq b^2 \exp\left(-s/\tilde{l}\right) , \tag{1.10}$$

where s is the distance between the segments n and m along the chain and $\langle ... \rangle$ stands for averaging over all possible configurations of the chain. A section of the polymer chain whose length is smaller than $\tilde{l}$ is practically stiff, whereas two sections separated by a distance larger than $\tilde{l}$ are independent of each other. Because the persistence length is hard to measure in the experiment, one usually defines the Kuhn segment length l from the mean squared end-to-end vector $\langle \vec{R}^2 \rangle = (L/l)l^2 = Ll$ which is of the same order of magnitude as the persistence length. Considering the whole polymer as an effective freely jointed chain of L/l practically stiff segments, one can again obtain the Gaussian distribution for the end-to-end vector. Evidently, the vector connecting two points of the chain which lie at a distance s larger than l also satisfies the Gaussian distribution.

A model that is made up of uncorrelated bond vectors is called the Gaussian model of the polymer chains. Let us write the position of the n-th bead of the chain as $\vec{R}_n$, where $n = 0, ..., N$ so that bond vectors become

$$\vec{r}_n = \vec{R}_n - \vec{R}_{n-1} , \tag{1.11}$$

A state of the Gaussian chain is defined by the set of the bead positions $\left\{\vec{R}_n\right\} = (\vec{R}_0, \vec{R}_1, ..., \vec{R}_N)$ which is realized with the probability

$$P\left(\left\{\vec{R}_n\right\}\right) = \left(\frac{3}{2\pi\tilde{b}^2}\right)^{3N/2} \exp\left(-\frac{3}{2\tilde{b}^2}\sum_{n=1}^{N}(\vec{R}_n - \vec{R}_{n-1})^2\right) , \tag{1.12}$$

where $\tilde{b}$ is the mean length of the bond vector.

One can think of (1.12) as the probability distribution in the canonical ensemble of N harmonic springs linked together. The energy of the chain can then be written as

$$U = \frac{1}{2}k\sum_{n=1}^{N}(\vec{R}_n - \vec{R}_{n-1})^2 \tag{1.13}$$

with the spring constant $k = 3k_BT/b^2 of the entropic origin$. The Gaussian model is often called the bead-spring model; it is very useful because of its simple mathematical formulation.

A more convenient measure of the polymer size which is readily accessible in experiments based on light scattering is the radius of gyration defined by

$$R_G^2 = \frac{1}{N}\sum_{n=1}^{N}\left\langle(\vec{R}_n - \vec{R}_{cm})^2\right\rangle , \tag{1.14}$$

where $\vec{R}_{cm}$ is the center of mass of the chain

$$\vec{R}_{cm} = \frac{1}{N}\sum_{n=1}^{N}\vec{R}_n\,. \tag{1.15}$$

The radius of gyration for the ideal chain in the limit $N \to \infty$ reads

$$R_G^2 = \frac{1}{6}N\tilde{b}^2\,. \tag{1.16}$$

The Fourier transform of the pair correlation function of the chain

$$g(\vec{r}) = \frac{1}{N}\sum_{n=1}^{N}\sum_{m=1}^{N}\left\langle \delta(\vec{r} - (\vec{R}_m - \vec{R}_n))\right\rangle \tag{1.17}$$

can be easily calculated for the Gaussian chain; the final result reads

$$g(\vec{q}) = \int d^3r g(\vec{r})e^{i\vec{q}\vec{r}} = N\frac{2}{x^4}\left(\exp(-x^2) - 1 + x^2\right)\,, \tag{1.18}$$

where $x = q\ R_G$ and the function in the brackets with the prefactor $2/x^4$ is the Debye scattering function. It is clearly seen from (1.18) that the scattered intensity from the chain which is proportional to $g(\vec{q})$ involves only one microscopic length scale, namely R_G. In the limit $qR_G \gg 1$ one can find

$$g(\vec{q}) \simeq \frac{2N}{q^2R_G^2}\,, \tag{1.19}$$

and for $qR_G \ll 1$ one has $g(\vec{q}) \simeq N$.

More complicated models of the polymer chain take into account excluded volume effects, which produce repulsive interactions between beads separated by an arbitrary distance along the chain. In order to avoid unfavorable contacts between the beads, the chain favors swollen states as opposite to the ideal chain. A number of ideal chain configurations are disallowed due to excluded volume effects and the average size of such chains become larger than that of the ideal chain. The radius of gyration of the excluded volume chain depends stronger on the number of beads,

$$R_G \sim N^{\nu} \tag{1.20}$$

with $\nu > 1/2$. The exponent ν obtained in computer simulations on self-avoiding chains with large lengths in the three-dimensional space was found to be approximately 0.588, see [Doi96]. A simple mean field argument due to Flory [deGen] leads to $\nu = 3/5$.

1.2 Rouse Dynamics

So far we considered the equilibrium properties of the polymer chain. Polymer systems are very interesting objects regarding their dynamic properties such as viscoelasticity which makes them irreplaceble materials in the industry. In this section we review a simple model describing the polymer dynamics where the polymer coils are supposed to be free of excluded volume effects

and topological constraints which forbid the intersection of different links. The solvent is assumed to be an imobile medium whose influence on the monomer motion is accounted for by a friction coefficient. The model is based on the underlying Gaussian chain and is known as the Rouse model.

We concentrate on an isolated chain in the medium. The equation of motion of the nth bead can be written as

$$m\frac{\partial^2 \vec{R}_n}{\partial t^2} = \vec{f}_n^{(ch)} + \vec{f}_n^{(fr)} + \vec{f}_n^{(r)}\,, \tag{1.21}$$

where m is the mass of the bead. The first term on the right side of (1.21) describes the force experienced from the neighboring beads. This force can be found from the potential energy of the Gaussian chain (1.13),

$$\vec{f}_n^{(ch)} = \frac{3k_BT}{b^2}(\vec{R}_{n+1} - 2\vec{R}_n + \vec{R}_{n-1})\,. \tag{1.22}$$

$\vec{f}_n^{(fr)}$ is the friction force which is assumed to be proportional to the velocity of the bead

$$\vec{f}_n^{(fr)} = \zeta\frac{\partial \vec{R}_n}{\partial t}\,, \tag{1.23}$$

where ζ is the friction coefficient. The last term in (1.21) describes a stochastic force caused by collisions of the bead with the solvent molecules. As in the theory of Brownian motion, it is assumed that this force is Gaussian distributed and delta correlated

$$\langle f_{n\alpha}^{(r)}(t) f_{m\beta}^{(r)}(t')\rangle = 2\zeta k_BT\delta_{nm}\delta_{\alpha\beta}\delta(t-t')\,, \tag{1.24}$$

where α and β are the coordinate components and $\delta_{\alpha\beta}$ is the Kroneckers' symbol.

In the large friction limit the inertia forces can be neglected so that the equations of motion are reduced to

$$\zeta\frac{\partial \vec{R}_n}{\partial t} = \frac{3k_BT}{b^2}(\vec{R}_{n+1} - 2\vec{R}_n + \vec{R}_{n-1}) + \vec{f}_n^{(r)}\,. \tag{1.25}$$

This set of coupled Langevin equations can be rewritten in the continuum limit as

$$\zeta\frac{\partial \vec{R}_n}{\partial t} = \frac{3k_BT}{b^2}\frac{\partial^2 \vec{R}_n}{\partial n^2} + \vec{f}_n^{(r)}\,, \tag{1.26}$$

where n is now a continuous variable along the chain. With the help of a Fourier representation

$$\vec{x}_p = \frac{1}{N}\int_0^N dn\cos\left(\frac{\pi np}{N}\right)\vec{R}_n(t)\,, \quad p = 0,1,2,... \tag{1.27}$$

the Langevin equations become decoupled,

$$\zeta\frac{\partial}{\partial t}\vec{x}_p = -\frac{\zeta}{\tau_p}\vec{x}_p + \vec{f}_p \quad (p \neq 0)\,, \tag{1.28}$$

$$\zeta\frac{\partial}{\partial t}\vec{x}_0 = \vec{f}_0\,, \tag{1.29}$$

where

$$\tau_p = \frac{N^2 b^2 \zeta}{3\pi^2 k_B T p^2} \quad (p \neq 0) \tag{1.30}$$

are a characteristic set of relaxation times. The variables $\vec{x}_p$ are called the Rouse mode amplitudes. One can calculate their correlation functions from (1.28),

$$\langle x_{p\alpha}(t) x_{q\beta}(0)\rangle = \delta_{pq}\delta_{\alpha\beta}\frac{3k_B T\tau_p}{2N\zeta}\exp\left(-\frac{t}{\tau_p}\right) \quad (p>0)\,, \tag{1.31}$$

For the mode $\vec{x}_0(t)$ one has

$$\langle x_{0\alpha}(t) x_{0\beta}(0)\rangle = \delta_{\alpha\beta}\frac{2k_B T}{N\zeta}t\,. \tag{1.32}$$

The physical meaning of the Rouse modes is quite simple, for example the mode $\vec{x}_0$ represents the center of mass

$$\vec{R}_{cm} = \frac{1}{N}\int_0^N dn\vec{R}_n = \vec{x}_0\,, \tag{1.33}$$

while for $p \neq 0$ they describe the internal structure of the chain. From (1.32) the motion of the center of mass is diffusive,

$$\left\langle (\vec{R}_{cm}(t) - \vec{R}_{cm}(0))^2 \right\rangle = 6Dt \tag{1.34}$$

with the diffusion coefficient

$$D = \frac{k_B T}{N\zeta}\,. \tag{1.35}$$

Note that the Rouse model predicts the diffusion coefficient to be inversely proportional to the chain length N.

The end-to-end vector of the chain, which we now denote by $\vec{P}$, can be expressed by the sum

$$\vec{P}(t) = -4\sum_{p=1,3,5,\ldots}\vec{x}_p(t) \tag{1.36}$$

and its correlation function reflects the rotational behavior. At large times $t \geq \tau_1$ the correlation function of $\vec{P}$ decreases as

$$\left\langle \vec{P}(t)\vec{P}(0)\right\rangle \sim \exp\left(-\frac{t}{\tau_r}\right) \tag{1.37}$$

with

$$\tau_r = \frac{\zeta N^2 b^2}{3\pi^2 k_B T}\,. \tag{1.38}$$

From the Rouse model, one can calculate the mean square displacement of the n-th bead as

$$\left\langle (\triangle\vec{R}_n(t))^2\right\rangle \simeq 6Dt + 2b\sqrt{\frac{3k_B T}{\pi\zeta}t} \tag{1.39}$$

As opposite to normal diffusion, the mean square displacement increases at short times as $t^{1/2}$. Note also that the short time behavior is N–independent.

The Rouse model neglects hydrodynamic interactions which influence the polymer dynamics in the dilute solutions. One measures there the following scalings of the diffusion constant and the relaxation time of the end-to-end vector relative to N: $D \sim N^{-1/2}$, $\tau_1 \sim N^{3/2}$. The Zimm model which takes into account the hydrodynamic interactions, correctly reproduces these scalings. However, the Rouse model becomes surprisingly valid for polymers in the melt, see Section 1.3. Computer simulations of dense melts based on the bond fluctuation model found features consistent with the Rouse dynamics [Kre01], where, for example, lower Rouse modes were observed.

1.3 Polymer Solutions and Melts

The properties considered so far are valid for individual chains or chains in dilute solutions, where the macromolecules do not overlap and only rarely interact with each other. When we, however, increase the volume fraction of the polymer molecules in a solution, it passes through two distinct regimes: *i*) a semidilute solution where the chains are strongly overlapping but the polymer volume fraction is still small; *ii*) a concentrated solution or polymer melt with volume fraction near unity. The critical concentration of monomers c^* at which the dilute solution becomes a semidilute one can be estimated as follows. The chains in a polymer solution start to overlap at the concentrations

$$c \geq c^* \sim \frac{N}{R_G^3} = N^{1-3\nu} \tag{1.40}$$

where ν is the scaling exponent of R_G with the chain length N according to (1.20). For chains with excluded volume effects ($\nu \simeq 0.6$) it holds that $c^* \sim N^{-0.8}$ so that the chains with larger lengths overlap at lower concentrations.

A remarkable feature of the concentrated polymer solutions is that the individual chains behave on large spatial scales like the Gaussian coil. An immediate consequence of this statement known as the Flory theorem is that the radius of gyration scales with $N^{1/2}$ [deGen].

Such behavior of the chain in concentrated solutions can be easily understood within the self-consistent field approximation [deGen]. In this approximation all interactions experienced by a monomer in a concentrated solution are represented through a potential U whose value at the monomer position is proportional to the average local concentration of all other monomers at that point. Let us consider the forces acting on the monomer at $\vec{r}$ belonging to the chain s. Let $U_s(\vec{r})$ be the potential field created at $\vec{r}$ by all monomers of the same chain s. The force of this field $-\frac{\partial U_s(\vec{r})}{\partial \vec{r}}$ points outward of the molecule because the concentration of the monomers of the sth chain $c_s(\vec{r})$ decreases with the distance from its center. $U_w(\vec{r})$ is the field created by all other monomers in the solution; this field causes a force $-\frac{\partial U_w(\vec{r})}{\partial \vec{r}}$ pointing inside the molecule because the concentration of such monomers decreases in the region occupied by the chain s. In a homogeneous concentrated solution, the total monomer density $c(\vec{r}) = c_s(\vec{r}) + c_w(\vec{r})$ (with $c_w(\vec{r})$ being the concentartion of all monomers not belonging to the sth chain) is a constant coordinate-independent quantity. Therefore, the total force $-\frac{\partial U_s(\vec{r})}{\partial \vec{r}} - \frac{\partial U_w(\vec{r})}{\partial \vec{r}}$ acting on the monomer at $\vec{r}$ is zero and the whole chain neither shrinks nor swells.

1.4 Polymer Mixtures

A mixture of two polymers of different types A and B can phase separate forming macroscopic regions pure in A and B monomers. Here we study thermodynamic conditions needed for polymer demixing.

We follow the Flory-Huggins treatment [Doi96] of polymers where each A (B) molecule occupies N_A (N_B) connected points on a rectangular lattice with the coordination number z. We assume that there are no solvent molecules in the system (which are otherwise modelled as vacancies). One site of the lattice is allowed to be occupied only by one monomer, so that the volume fractions of the A and B components are

$$\phi_A = \frac{n_A N_A}{M}\,, \quad \phi_B = \frac{n_B N_B}{M}\,. \tag{1.41}$$

Here n_A, n_B are the numbers of chains of type A, and B and M is the total number of sites of the lattice. The interaction energy of two monomers is nonzero only if they occupy neighboring sites; it is equal to ϵ_{AA}, ϵ_{BB} for monomers of the same type, respectively, and ϵ_{AB} if the monomers are of different types.

The free energy of mixing per lattice site of the system described above has the following form

$$\frac{f_{FH}}{k_B T} = \frac{\phi_A}{N_A}\ln\phi_A + \frac{\phi_B}{N_B}\ln\phi_B + \chi\,\phi_A\,\phi_B\,, \tag{1.42}$$

where the first two terms describe the translational entropy and the third term accounts for the interaction between monomers. The parameter χ defined as

$$\chi = \frac{z}{k_B T}\left(\epsilon_{AB} - \frac{\epsilon_{AA}+\epsilon_{BB}}{2}\right) \tag{1.43}$$

is called the Flory-Huggins interaction parameter. Positive values indicate a net repulsion between A and B species leading to demixing whereas negative ones imply a tendency towards mixing. The parameter χ has values in the range $10^{-4} < \chi < 10^{-1}$.

The critical point where the homogeneous $A-B$ mixture under the incompressibility condition $\phi_A + \phi_B = 1$ becomes unstable against phase separation can be calculated from the requirement that f_{FH} passes from a single minimum to a double minimum structure. With the help of the equation $\frac{\partial^2 f_{FH}}{\partial \phi_A^2} = 0$ this leads to critical values

$$\chi_c = \frac{(N_A^{1/2}+N_B^{1/2})^2}{2N_A N_B}\,, \qquad \phi_A^{(cr)} = \frac{N_B^{1/2}}{N_A^{1/2}+N_B^{1/2}}\,, \quad \phi_B^{(cr)} = \frac{N_A^{1/2}}{N_A^{1/2}+N_B^{1/2}}\,. \tag{1.44}$$

It follows from the first equation in (1.44) that a very small value of χ would be enough to separate two species of polymers with large lengths N_A and N_B. In practice, there are very few polymers which satisfy the condition $\chi < \chi_c$ and which can be found in a mixed state. The Flory-Huggins treatment ignores specific polymer properties. More detailed theories of phase separation in polymer mixtures are reviewed for example in [Bin94]. Some aspects are discussed in Section 1.5 in the context of soft particle models.

1.5 Soft Particle Models

The fact that a polymer molecule consists of a large number of identical units makes it possible to treat this object in terms of statistical physics. Coarse graining by elimination of irrelevant degrees of freedom is a central problem in many areas of statistical physics, especially when modelling diffusion and phase kinetics processes in polymer systems [Bin94]. Important processes are phase separation in polymer melts with incompatible components, see Section 1.4 which occur on time and length scales many orders of magnitude larger than those related to the motion of individual monomers, or microphase separation in block copolymers as described in Section 1.6. A detailed understanding of such processes is required in present-day attempts to utilize polymers in the design of new materials and in the production of tailored micro- or nanoscale structures through selforganization, see [Bin94], [Böl98].

From the theoretical viewpoint this poses the problem to eliminate internal degrees of freedom of polymer chains, which largely become irrelevant in such processes, and to seek for a coarse grained description of the phase kinetics in terms of a smaller number of collective degrees of freedom. In order to cover effects of chain length, monomer interactions, possible heterogeneities of chains e.g. in the case of copolymers, and wall interactions in the case of confinement [Bas95], such theories have to be based on appropriate microscopic input.

A promising approach is to represent the random coil built by a polymer chain simply by one "soft particle", an idea that is based on the fact that polymers in the melt strongly interpenetrate. This soft-particle picture should be valid for length and time scales similar to or larger than the radius of gyration R_G and the diffusion time $\tau_D \simeq R_G^2/D_{CM}$, respectively, where D_{CM} denotes the center-of-mass diffusion constant.

For homopolymers, Murat and Kremer have proposed a soft ellipsoid model, where ellipsoids can change their position, shape and orientation [Mur98a]. Instead of using the bead-spring model as microscopic input for the soft ellipsoid model, Eurich and Maass suggested to derive the parameters for the intra- and interchain free energies from a model of Gaussian chains [Eur01]. This choice is motivated by the fact that chains in dense melts become nearly Gaussian. With this theory structural and kinetic properties of both one-component melts and binary mixtures were studied successfully for bulk systems. In a subsequent extension to confined systems it was shown how spinodal decomposition in polymer blends becomes modified in thin films, including situations of periodically patterned walls [Eur02]. In earlier work, soft spheres instead ellipsoids were considered and effective interactions between spheres in the melt were derived by an explicit elimination procedure for monomer degrees of freedom [Lik01]. Also, concepts from liquid structure theory were used to relate the input parameters of soft particle models to microscopic properties (see papers [Yab04], [Yab05], [Bol01]).

One of the advantages of the soft particle models over those based on the Flory-Huggins treatment described in the previous section 1.4 is that they are continuous-space models. That means that they are free of a spatial anisotropy introduced by the underlying lattice structure. Effects of the lattice can be relevant for example when studying demixing of polymer mixtures in confined geometries, see Section 2.4.2 or microphase separation in thin films of diblock copolymers, 1.8. Another issue is the absence of the vacancies otherwise required in the lattice algorithms to allow local and reptational moves. The absence of the vacansies is crucial in the mixture of asymmetric polymers with different monomer volumes.

1.6 Diblock Copolymers

A block copolymer consists of two or more chemically distinct blocks which are covalently bound to form one molecule. Depending on the number of blocks and the chemical conditions under which the molecules are produced, the blocks can be connected in linear (for example ABC copolymer) or branched (star and grafted) sequences, Fig. 1.1.

Because of the covalent bonds between the blocks, a melt of copolymer molecules cannot demix on macroscopic scales at low temperatures as in polymer blends but phase separates in mesoscopic structures whose length scales are typically $10 - 100$ nm.

Here we only consider diblock copolymers made up of N_A monomers of type A and N_B monomers of type B, the total number of monomers in the chain being $N = N_A + N_B$. For diblock copolymer melts, the geometry of microphase separated regions is essentially controlled by two parameters: the volume fraction of A-monomers $f_A = N_A/(N_A + N_B)$ and the Flory-Huggins parameter χ. It was found that the phase behavior depends primarily on f_A and the product χN. For $\chi N < (\chi N)_c$ the system is homogeneous and its thermodynamic properties are similar to those of the polymer blends. At larger values of χN, above the order-disorder transition (ODT) curve, four ordered microphase structures are predicted to have regions of thermodynamic stability, see Fig. 1.2.

The lamellar phase consisting of alternating flat A- and B-rich layers is stable for nearly symmetric molecules, while a hexagonally packed cylindrical phase is stable for molecules with an intermediate level of compositional asymmetry. In the cylindrical phase with $f_A > 0.5$, the smaller B-blocks pack into the interiors of the cylinders, whereas the longer A-blocks reside on the outer side of the cylinders which allows them to have more configurational entropy. With still higher asymmetry, the melt is ordered into a body-centered cubic spherical phase where the minority blocks form spheres.

Close to the ODT and in a narrow region between the lamellar and cylindrical phases, the bicontinuous gyroid morphology can emerge where the minority domains form two interweaving three-fold coordinated lattices. There are two other complex microstructures observed in the experiment [Ham99], one of which being the perforated lamellar phase where the minority layers have hexagonally ordered bridges connecting the majority layers. Another structure is the double-diamond phase similar to the gyroid one, but where the interweaving lattices are four-fold coordinated.

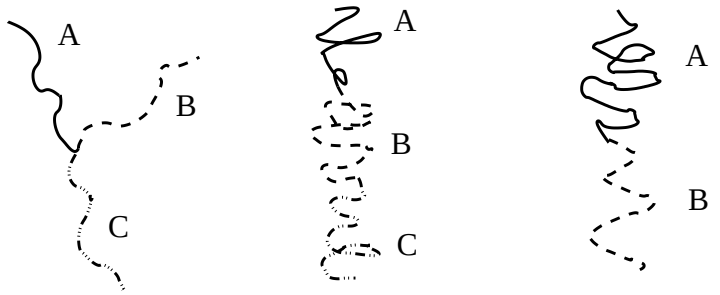

Figure 1.1: Schematic representation of block copolymer architecture: star triblock copolymer (left), linear triblock copolymer (center) and diblock copolymer (right).

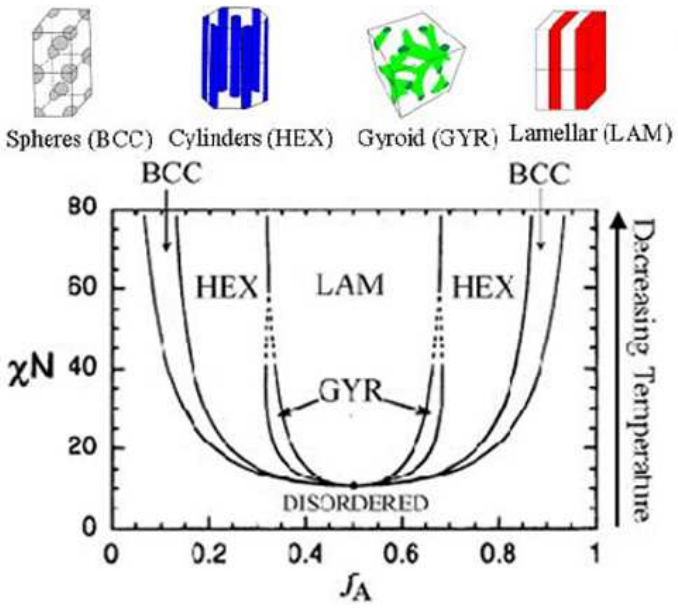

Figure 1.2: Schematic diblock copolymer phase diagram. f_A is the volume fraction of A-monomers, χ is the Flory-Huggins interaction parameter and N is the polymerization degree. Diagram is adapted from [Bat99].

For symmetric diblock copolymers in the ordered lamellar phase with the lamellar periodicity λ, one distingishes two limiting cases: *i*) weak segregation where χ is close to the ODT and the ordered structure can be described by a single sinusoidal concentration profile and *ii*) strong segregation limit (large values of χ) where nearly pure A and B domains are separated by fairly sharp interfaces.

In the weak segregation regime, the molecule configurations are assumed to be undisturbed Gaussian coils, so that the characteristic length λ of the sinusoidal fluctuations scales with the chain length N as $\lambda \sim R_G \sim N^{1/2}$. In the opposite case of the strong segregation, the chains become stretched in the direction perpendicular to the interfaces to avoid energetically unfavorable contacts between A and B monomers. The free energy of the chain which is extended to a half-period in the lamellae with the covalent linkage located at the interface can be split into two parts [Bin94],

$$\frac{F_{lam}}{k_B T} = \frac{3}{2}\frac{(\lambda/2)^2}{Nb^2} + \frac{\gamma S}{k_B T}\,, \tag{1.45}$$

where the first term is the stretching energy which is assumed to be the same as for the Gaussian chain. The second term describes the interfacial energy between A- and B-rich domains, where γ is the A-B interfacial tension and S is the interfacial area per chain determined from the incompressibility condition $S\lambda/2 = Nb^3$. The interfacial tension depends on the interaction parameter χ only, $\gamma = (k_B T/b^2)\sqrt{\chi/6}$. With the help of these results, minimization of the free energy leads to the following scaling law

$$\lambda \sim \chi^{1/6} N^{2/3} \tag{1.46}$$

which shows significant stretching of the chain in the direction perpendicular to the interface.

1.7 Theoretical Approaches

1.7.1 Leibler Mean Field Theory

After the overview on the phase behavior, we now turn to a brief description of existing analytic theories and simulations. The first mean-field theory of Landau type for weakly segregated diblock copolymer melts was developed by Leibler in 1980 [Lei80]. It assumes that the melt is incompressible $\varrho_A(\vec{r}) + \varrho_B(\vec{r}) = 1$, where $\varrho_A(\vec{r})$ and $\varrho_B(\vec{r})$ are local densities of A and B monomers. The order parameter can be defined as

$$\psi(\vec{r}) = \varrho_A(\vec{r}) - f_A\,; \tag{1.47}$$

its average is zero in the disordered melt, but displays a periodic spatial modulations about zero in the ordered phases.

Following the presentation in [Mat02], the free energy of the melt is expanded in powers of the order parameter $\psi(\vec{r})$ as

$$\begin{aligned}\frac{F[\phi]}{k_BT} &= \chi N f_A(1-f_A) + \frac{V}{2!(2\pi)k_BT}\int d^3q_1\, S^{-1}(\vec{q}_1)\phi(\vec{q}_1)\phi(-\vec{q}_1) + \\ &+ \frac{V^2}{3!(2\pi)^2k_BT}\int d^3q_1\, d^3q_2\, \Gamma_3(\vec{q}_1,\vec{q}_2)\phi(\vec{q}_1)\phi(\vec{q}_2)\phi(-\vec{q}_1-\vec{q}_2) + \\ &+ \frac{V^3}{4!(2\pi)^3k_BT}\int d^3q_1\, d^3q_2\, d^3q_3\, \Gamma_4(\vec{q}_1,\vec{q}_2,\vec{q}_3)\phi(\vec{q}_1)\phi(\vec{q}_2)\phi(\vec{q}_3)\phi(-\vec{q}_1-\vec{q}_2-\vec{q}_3) + \dots\,,\end{aligned} \tag{1.48}$$

where $\phi(\vec{q})$ is the Fourier transform of $\psi(\vec{r})$

$$\phi(\vec{q}) = \frac{1}{V}\int d^3r\psi(\vec{r})e^{\mathrm{i}\vec{q}\vec{r}}\,, \tag{1.49}$$

and $S(\vec{q})$ is the structure factor defined through the density-density correlations

$$S(\vec{q}) = \frac{1}{V}\int d^3r\,\langle\psi(\vec{r})\psi(0)\rangle\, e^{-\mathrm{i}\vec{q}\vec{r}}\,, \tag{1.50}$$

and V is the system volume. The functions $\Gamma_3(\vec{q}_1,\vec{q}_2)$, $\Gamma_4(\vec{q}_1,\vec{q}_2,\vec{q}_3)$ in the expantion (1.48) are determined through the Fourier transforms of multiparticle correlation functions.

To proceed further, one considers the weak segregation limit and assumes that the coil configurations are not disturbed by the A-B monomer repulsion and hence obey Gaussian statistics (the random-phase approximation). Consider the first two terms in the expansion (1.48), where the structure factor is orientationally invariant and can then be shown to have the form

$$NS^{-1}(q) = F(f_A,x) - 2\chi N\,, \tag{1.51}$$

where $x = qR_G$ and

$$\begin{aligned}F(f_A,x) &= g(1,x)/\left[g(f_A,x)g(1-f_A,x) - h^2(f_A,x)h^2(1-f_A,x)\right]\,,\\ g(s,x) &= 2\left[sx^2 + \exp(-sx^2) - 1\right]/x^4\,,\\ h(s,x) &= \left[1-\exp(-sx^2)\right]/x^2\,.\end{aligned} \tag{1.52}$$

The function $F(f_A, x)$ is positive and has a minimum at $x^* = q^* R_G$ leading to a peak in the structure factor at $q = q^*$. This means that in the disordered melt at lower values of χN, the free energy is minimized at the monomer density modulations with the characteristic length $2\pi/q^*$ which does not depend on the value of χN. With increasing χN, the hight of the structure factor peak increases until a spinodal curve is encountered where $S(q)$ diverges. In the vicinity of the spinodal, the ordered structures are those that satisfy $|\vec{q}| = q^*$, where q^* depends on the composition f_A. An important issue of the Leibler theory is that the equilibrium state of the diblock copolymer melt is completely determined by two parameters: the product χN and the composition f_A.

The structure factor for symmetric diblock copolymers is obtained from (1.51) with $f_A = 1/2$ and has the following form:

$$N S^{-1}(q) = F(q\, R_G) - 2\chi\, N\,, \tag{1.53}$$

where

$$F(x) = \frac{x^4}{2}\left(\frac{x^2}{4} + e^{-x^2/2} - \frac{1}{4}e^{-x^2} - \frac{3}{4}\right)^{-1}\,. \tag{1.54}$$

It shows a maximum at

$$q^* = 1.95/R_G \tag{1.55}$$

in the disordered phase with a height that diverges at the critical point

$$(\chi N)_c \simeq 10.5\,. \tag{1.56}$$

A study of the higher order terms in the Landau expansion (1.48) reveals that the fourth order term is always positive. The third order term is absent for symmetric diblock copolymers because otherwise the free energy would depend on interchanging physically similar A and B components. Hence, symmetric copolymers undergo a second order phase transition at the ODT. For asymmetric diblock copolymers, the third term in (1.48) is present and the phase transition is of first order. In this way one finds the lamellar, hexagonal or body-centered cubic phases.

It turns out in the experiment [Bat88] and computer simulations [Bin91] of symmetric diblock copolymers that the position of the structure factor peak q^* shifts towards smaller values of q when increasing the parameter χN in the disordered phase. This means that the diblock copolymer gets deformed and does not behave like a Gaussian chain even in the disordered phase. The ODT point as estimated from extrapolation of the inverse structure factor to zero values also lies above the Leibler prediction $(\chi N)_c \simeq 10.5$. However, a slightly modified Leibler structure factor of the form [Bin91]

$$N\, S_{fit}^{-1}(q) = \frac{1}{\alpha}\left[F(q\,\tilde{R}_G) - \delta\right]\,, \tag{1.57}$$

where α, $\tilde{R}_G$ and δ are treated as free parameters, nicely fits the data obtained in the experiment and simulations.

Fredrickson and Helfand [Fre87] went beyond the mean-field approximation used in the Leibler theory and included compositional fluctuations within Hartree corrections. These corrections are of importance in the vicinity of the ODT. They predicted a shift of the ODT point towards higher values of χN in the form

$$(\chi N)_c^{\mathrm{FH}} = 10.5 + 41.0 N^{-1/3} \tag{1.58}$$

showing an additional dependence of the thermodynamic properties on the chain length N. A strong increase of the local fluctuations near the ODT drives the phase transition of the symmetric diblock copolymers to be of the first order. Another prediction of the theory is the direct transition to the lamellar phase from the disordered melt for nearly symmetric molecules, whereas in the Leibler theory, one encounters regions of the bcc and the cylindrical structures.

This theory also leads to a modification of the structure factor

$$NS_{FH}^{-1}(q, \chi N, N) = NS^{-1}(q, \chi N) + A[\tau N]^{-1/2}\,, \tag{1.59}$$

where A is a constant and τ is to be determined from

$$\tau = F(x^*) - 2\chi N + A[\tau N]^{-1/2}\,. \tag{1.60}$$

The inverse of the maximum of the corrected structure factor does not vanish at the ODT, but displays a a monotonous decay characteristic for a weak first order phase transition when increasing χN, in agreement with experimental and simulation results [Bin94]. The Leibler theory predictions are recovered in the limit of very long chains $N \to \infty$.

Another mean field like theory based of the free energy functional similar to that of Leibler with an additional term describing the long-range interaction of the local monomer concentration deviations was proposed by Ohta and Kawasaki [Oht86] for the strong segregation limit. They studied lamellar, cylindrical and spherical geometries and predicted the power law $\lambda \sim N^{2/3}$ with an exponent 2/3 for the scaling of the periodicity with the chain length N.

1.7.2 Simulations

Among the theoretical treatments, computer simulations have become an important tool in the study of polymer and diblock copolymer systems [Bin95], providing more insight into the microscopic properties of the individual chains than available from experiment. The simplest and the most widely used method with low equilibration time and capable of simulating large systems has been the lattice Monte-Carlo method. Fried and Binder [Bin91] have applied this technique to study a dense melt of symmetric diblock copolymers near the ODT. Their model assumed fixed bond length. They monitored static properties such as the structure factor and the radius of gyration and found a shift of the peak position of the structure factor towards smaller values of q in the disordered phase, attributed to deformations of the molecules. The structure factor they found could perfectly be fitted by the generalized Leibler form (1.57).

The bond fluctuation model, where the length of bond vectors is allowed to take a set of possible values, has been used by Hoffmann et al. to study the influence of the ODT and the geometry of the ordered structures on various dynamic and static properties in a broad range of interactions for symmetric [Hof97a] and asymmetric [Hof97b] diblock copolymers.

Lattice models considered so far are limited in the sense that the underlying lattice structure introduces a spatial anisotropy in the properties of otherwise isotropic systems. To overcome this problem, continuous-space molecular dynamics studies were carried out where chains were treated by the bead-spring model. These simulations provide insight into the detailed changes of chain conformation near phase boundaries ([Gre96], [Mur98b], and [Mur99]), the internal energy and entropy [Schu02]. More sophisticated is the "dissipative particle dynamics" (DPD) method

that includes hydrodynamic forces between effective beads of polymers [Gro98], [Gro99]. The DPD has also been generelized to the entangled state of copolymers [Mas06].

So far, we considered models which describe diblock copolymer systems in equilibrium. There are several approaches to the far-from-equilibrium dynamics based on evolution equations for monomer densities. One of them is an extension of the Cahn-Hilliard model used to study phase separation in binary alloys, see for example [Cha91]. In this model, one writes the time variation of the concentration field $\phi(\vec{r},t)$ in terms of a variational derivative of a free-energy functional given by the generalized Ginzburg-Landau expression

$$F[\phi] = \int d^3r \left[-\frac{b}{2}\phi^2 + \frac{u}{4}\phi^4 + \frac{K}{2}|\nabla\phi|^2 + B\int d^3r' G(\vec{r},\vec{r}')\phi(\vec{r},t)\phi(\vec{r}',t') \right] . \tag{1.61}$$

This leads to

$$\frac{\partial\phi(\vec{r},t)}{\partial t} = M\nabla^2\left(-b\phi + u\phi^4 - K\nabla^2\phi\right) - B\phi\,. \tag{1.62}$$

Here M, b, u, K, and B are phenomenological parameters of the model; the last term in (1.61) and (1.62) originates from the diblock structure of the molecule. $G(\vec{r},\vec{r}')$ is the Green function to the Laplace equation. In this way, these terms supress long wave length fluctuations in $\phi(\vec{r},t)$. They favor the state $\phi = 0$ relative to the phase-separated states with $\phi \neq 0$.

A powerful extension of this method is the self-consistent field model which proved successful in studying diblock copolymer properties in the strong and intermediate segregation regimes [Mül05a] and [Lud05].

1.8 Diblock Copolymers in Confined Geometries

The microphase separation of the diblock copolymers in the bulk leads to polydomain structures with random orientations. To obtain materials with desired directional properties, it is essential to control macroscale order. Active processing with applied flow fields can extend self-assembled order to macroscopic dimensions [Wan97]. Block copolymers confined to thin films are also often characterized by highly oriented domains. This orientation is a direct result of surface and interfacial energy minimization. Generally, films of thickness $d > \lambda$ exhibit full lamellae oriented parallel to the substrate if the confining surfaces are homogeneous and attractive to one of the components of the molecule. These surface-parallel lamellae optimize the interfacial free energy by minimizing the A-B interface area while maintaining the lamellar periodicity. If the same block is found at each boundary, the copolymer film is said to exhibit symmetric wetting. Otherwise, films that express different blocks at each surface are called asymmetric. At equilibrium, symmetric systems exhibit a series of stable films when $d = n\lambda$ $(n = 1, 2, 3, ...)$, whereas asymmetric films exhibit a series of stable films when $d = (n + 1/2)\lambda$.

One can realize symmetric boundary conditions experimentally in the free-standing films or when films are confined between two identical substrates. Confined systems were first used in the work [Lam94], [Kon95] to probe confinement effects on block copolymer film morphologies. In these studies, confining walls were strongly attractive to one of the copolymer blocks. As the film thickness was forced to values incommensurate with multiples of λ, contraction and expansion of the lamellar period were observed. Kellogg and coworkers were the first to induce surface-perpendicular lamellar orientations through symmetric boundary conditions in

diblock films [Kel96]. Neutral boundary conditions for polystyrene-b-poly(methylmethacrylate) (PS-b-PMMA) were created by confining this material between films of an equimolar random copolymer of styrene and MMA. This technique was later improved by Huang et al. [Hua99]. Using a better estimate of the random copolymer composition required for surface-energy neutrality in the PS-PMMA system as reported by Mansky and coworkers [Man97], highly oriented perforated-lamellar [Hua98] and surface-perpendicular cylindrical domains [Thu00] were observed.

In experiment, diblock copolymers are often cast onto a substrate with the opposite side of the film being open to the air. The existence of the free surface has important consequences on the film geometry. When the film thickness is incommensurate with the lamellar periodicity, $n\lambda < d < (n+a)\lambda$ with $n \geq 1$ and $0 < a < 1$, then upon annealing the morphology of the film develops such that a bifurcation into film regions appears with two different thicknesses that represent the closest conditions of stability, i.e. $n\lambda$ and $(n+1)\lambda$. Accordingly, the free surface forms plateaus of the height λ on a film with the thickness $n\lambda$, [Cou90], [Aus90]. The film area fractions of these domains mirror the degree of mismatch so that the amount of the thicker film is about $a/(n+1)\lambda$, whereas the thinner film fraction is $1 - a/(n+1)\lambda$, [Cou90]. In film systems that exhibit a thickness gradient, this effect leads to a series of step-like terraces of the height λ which accomodate the change in the thickness. The terracing was most studied for symmetric copolymers but the effect was also found for asymmetric molecules as well [Rad96], [Har98].

The orientation of domains in block copolymer films depends highly on the surface energy boundary conditions imposed on the system. Surfaces that are neutral with respect to each of the blocks induce the formation of microphase domains perpendicular to the surface [Wal94]. This effect was studied by Huang and coworkers to impart a surface-perpendicular orientation in both lamellar and cylindrical PS-b-PMMA systems, see [Hua99], [Man97].

Substrates imparted with chemical or topographic patterns can be used to direct microphase separation in diblock copolymer films. By using such substrates, local domain orientation, film surface morphology, and long-range order can be affected and sometimes controlled. Diblock films deposited onto chemically heterogeneous surfaces have received significant attention. There were many publications reporting theoretical treatments of diblock copolymer films on chemically patterned substrates, such as a Cahn-Hilliard type coarse grained model of Chakrabarty and coworkers, [Cha98] and the self-consistent field theory of Petera and Muthukumar [Pet98]. Wang et al [Wan00b] have performed intensive Monte-Carlo simulations on a simple cubic lattice to study commensurability effects in thin diblock copolymer films. These studies considered the effect of the substrate pattern periodicity on film morphology. In particular, when the period of the substrate pattern approaches the lamellar periodicity in the bulk, these studies predict a surface-perpendicular orientation of the block domains.

Pattern induced microphase separation in thin diblock copolymer films was also studied experimentally. Heier and coworkers ([Hei97], [Hei99], [Hei00]) examined the effect of micro-scale substrate chemical heterogeneity on symmetric diblock copolymer films. It was demonstrated that patterns with alternating wetting behaviors across patterned substrates induces a surface pattern of islands and holes that mirrors the substrate periodicity, [Hei99]. They have used this effect to study the kinetics of island formation and coarsening, [Hei00]. Yang and coworkers [Yan00] have used an X-ray lithography technique to examine similar effects on the submicron scale.

Rockford et al [Roc99] made the first observations of diblock films (compositionally symmetric PS-b-PMMA) on heterogeneous substrates with nanoscopic periodicity. The substrates had alternating stripes of gold and silicon, selectively attractive to PS and PMMA, respectively. They found that the perforated lamellar morphology formed when the copolymer and pattern periods matched. Moreover, the only defects in this perpendicular morphology were due to flaws in the substrate pattern itself. When the substrate period was longer or shorter than λ, diblock recognition of the underlying pattern was diminished. Stoykovich et al. [Sto03] have patterned a substrate with alternating lines and spaces with period between 45 and 55 nm using extreme ultraviolet interferometric lithography. Symmetric polystyrene-block-methyl methacrylate which was spin-coated and annealed on the substrate has formed perpendicular defect-free lamellae in register with the patterns of the substrate.

1.9 Polymer Electrolytes

Polymers can be an interesting subject of research when studying charge transport [Sko98], [Kan90]. Polymers which possess an electronic conductivity have become famous since 1990 as they were used in light-emitting diods [Sko98]. They are produced by doping where electrons are partially removed (oxidation) or added (reduction) to the *pi*-system of the polymer backbone of $trans-(CH)_x$ or polyaniline molecules. Another interesting class of conducting polymers are polymer electrolytes where chain backbones contain repeating electronegative atoms (anions) such as oxygen or nitrogen. Melts of such polymers dissolve certain salts because of the interaction between the cations of the salt and the polymer anions. An example of such ion conductive electrolytes are polyethers, e.g. polyethyle-oxide (PEO) complexed with Li salts which are mostly used in lithium-polymer rechargeable batteries. The salt cations attracted by the polar H_2O or NH_3 groups of the chain form shells around those groups building additional cross-links between polymer chains observed in molecular-dynamics simulations [Lee02]. Continuous motion of the molecules above the glass transition temperature places the polymer strands in and out of positions favourable for cation transfer between different polar groups. The dependence of the ion and chain diffusion on both the temperature and the ion concentration was studied with the help of a kinetic Monte-Carlo algorithm in [Dür04].

The conducting polymer materials are unique in that they combine many advantages of plastics, i.g. macroscopic mechanical stability, flexibility and processing from solution, with the additional advantage of conductivity either in the metallic or semiconducting regimes (synthetic metal), or significant ionic conductivities (polymer electrolytes). Ionic conductive polymers are widely utilized as solid electrolytes in various electrochemical devices [Gra91].

When treating the polymer electrolyte systems, one encounters another problem in addition to the coarse graining by omitting the irrelevant degrees of freedom discussed before in Section 1.5. Namely, the motion of the charge carrier (tracer) through the host enviroment occurs on the similar time scale as the disordered reorganizations of the medium which the tracer diffusion is actually coupled to. Such process can be thought of as random rearrangements of the available sites the tracer can occupy when moving through the medium.

It follows that ionic degrees of freedom and the much larger number of polymer degrees of freedom have to be treated on the same footing. Specifically, kinetic Monte Carlo (KMC) computer simulation of the diffusion coefficient of ions moving in a dynamically disordered

environment of polymer chains is hampered by the need to move every monomer (polymer bead or ion) with the same a priori probability. Therefore the positions of tracers remain unaffected by most of the Monte Carlo steps. A related situation arises in simulation studies of small neutral guest molecules passing through polymer membranes [Gus93]. Hence, the polymer electrolyte systems poses another challenge for the coarse-grained concept discussed above in Section 1.5.

In order to cope with this problem, it has been suggested long ago to employ dynamic percolation (DP) theory [Dru85], which generalizes the well-known problem of a random walk in a frozen percolating network to networks undergoing temporal renewals. In these early studies the renewal rate λ was regarded as a phenomenological parameter related to the polymer dynamics. Later it has been shown within a polymer lattice model that the DP-theory can be implemented in such a manner that diffusion of a tracer particle through a polymer matrix is reproduced with good quantitative accuracy [Dür02]. It was shown with the help of a generalized DP-theory [Dru88] that includes temporal correlations between renewal events through some waiting time distribution $\psi(t)$. The main idea in that treatment of diffusion through polymers was to determine $\psi(t)$ from local density fluctuations of the polymer network next to a frozen tracer particle, rather than considering $\psi(t)$ as phenomenological input [Dür02].

1.10 Goals of this Work

The major part of this work is aimed at the development of a soft particle model for diblock copolymer systems following initial steps due to F. Eurich [Eudiss]. The main point here is to show that the representation of the diblock copolymer as two soft spheres with the fluctuating radii of gyration and distance between their centers of mass can catch main features of the microphase separation in the bulk and in confined geometries on the length scale of the mean radius of gyration of one block $\langle R_X \rangle$ and on the time scale of the order $\tau_D = \langle R_X^2 \rangle / D_{CM}$, where D_{CM} is the diffusion coefficient of the molecule.

Following this aim, we first introduce the Gaussian Disphere Model (GDM) based on the previous work [Eudiss]. Then we test the model against the bulk properties of condenced melts of diblock copolymers which were reviewed in Section 1.6. It is shown that the structure factor, which mirrors the monomer number density fluctuations of one component, is well reproduced in the disordered melt by the modified Leibler structure factor (1.57), [Kar07].

Regarding the ordered phases, we find the lamellar structure (nearly symmetrical chains), the cylindrical and bcc phases (asymetrical chains) at higher values of χN. We show further that the lamellar period λ scales with χ and N as $\lambda / N^{0.5} \sim (\chi N)^n$ in the strong segregation with the exponent $n = 0.22$ being a little higher than the theoretical prediction 1/6, see [Bin94]. The scaling $\lambda \sim N^{0.5}$ is restored in the weak segregation regime of the lamellar phase. The model is also checked against the influence of the order-disorder transition on dynamic properties of the molecules. The results hereby confirm theoretical [Bar91] and simulation [Hof97a] studies.

After the model has been shown to successfully catch the bulk features, we turn to its application to the microphase ordering in thin films, see Section 1.8. Alignment of the molecules near the neutral walls induces the perpendicular oriented lamellae with a local order, [Kar07]. To obtaine a well ordered lamellar structure, the lower wall (substrate) of the film is patterned with alternating A and B-attractive stripes. Here the time dependent lateral structure factor

gives very detailed predictions on the ordering kinetics. It shows how the pattern transfer from the substrate is affected by the bulk-like ordering in the middle of the film. The perpendicular lamellae with the global order in register with the substrate are observed to overcome the spontaneous ordering when the pattern periodicity L_p is commensurate with the lamellar period in the bulk λ. If L_p differs from λ by 20% and more, one observes two stable structures: one in register with the alternating stripes in the vicinity of the substrate and another being the perpendicular lamellae of the bulk period λ with a local order in the rest of the film. The technique of the prepattering is of high interest because of its potential applications in nano fabrication such as optoelectronic devices, lithographic templating and surfaces with molecular recognition.

In addition, in a shorter part of this work, we study the tracer diffusion in the dynamically disordered polymer enviroment where the tracer motion occurs on the same time scale as the reorganisation of the host medium. It is shown that a significant additional coarse–grained step (beyond the standart chain models) can successfully be employed when studying tracer diffusion through a polymer network. This problem is of high relevance for polymer electrolytes (see Section 1.9). To treat it, we follow the idea of Dürr [Dür02] and divide the complicated problem into two simpler tasks of the tracer moving in the frosen polymer network and determining the waiting time distribution for the first renewal $\psi(t)$ which has to be calculated from local density fluctuations of the polymer network in the vicinity of the frozen tracer.

Employing the standart Verdier–Stockmayer algorithm, Dürr studied tracer diffusion at moderate densities c of the polymer network and found the tracer correlation factor $f(c)$ to be in agreement with results of the full simulations [Dür02]. We use the fluctuation site–bond Monte Carlo algorithm enabling us to concentrate on high densities of the polymer beads and so to test the method in this limit. We find the quantity $f(c)$ at least two times smaller than unity but still higher than those of the full simulation [Kar06]. We observe an intermediate regime in the time–dependent diffusion constant between the initial and the long–time behavior which may be compared with recent experiments on polymer electrolytes [Mar05], [Not02].

2 Soft Particle Models

In this section we give a general definition of the soft particle model and propose its application to block copolymers. We also review shortly main results obtained with a soft ellipsoid model when studying polymer melts and blends [Eur01], [Eur02]. Following the previous work of Eurich [Eudiss] we explore the possibility to map the internal degrees of freedom of a polymer molecule onto a finite set of variables **{X}** independent of the chain length N, allowing straightforward physical interpretation. In other words, it is attempted to coarsegrain as far as possible while keeping the most important structural characteristics of individual molecules. A concrete choice of the set **{X}** depends on the type and character of the problem the model is intended to be applied to. Because of its simplicity, this model should enable one to treat the time evolution of ordering structures, including surface-induced structures, in an efficient manner. Unlike simplified mean field type theories, it retains orientational effects and shape fluctuations of individual molecules, features, which again will be important when treating polymer systems in confined geometries. Moreover, a model of this type could become the basis for treating the phase behavior of more complex molecules.

In soft particle models for a single component system, the state of the particle is described by variables $\{\mathbf{X}\}$ and corresponds to some subvolume in the configurational space of the chain. Averaging the monomer number density of the chain over that subvolume produces the conditional monomer density of the soft particle $\varrho(\vec{x}|\mathbf{X})$ in the state $\{\mathbf{X}\}$. The density $\varrho(\vec{x}|\mathbf{X})$ is normalized by

$$\int \varrho(\vec{x}|\mathbf{X})\mathrm{d}^3x = N + 1\,, \tag{2.1}$$

where N is the number of bonds in the chain. Another input quantity is the probability distribution $P(\{\mathbf{X}\})$ for the soft particle to be found in the state $\{\mathbf{X}\}$. Both the monomer density $\varrho(\vec{x}|\mathbf{X})$ and $P(\{\mathbf{X}\})$ are to be calculated from the underlying microscopic chain model.

One can write the free energy of an ensemble of M otherwise identical molecules as the sum

$$F = F_{\mathrm{intra}} + F_{\mathrm{inter}}\,, \tag{2.2}$$

where the intramolecular part F_{intra} accounts for the entropic part of the free energy and is defined through the probability distribution $P(\{\mathbf{X}\})$ in the system with all the intermolecular interactions switched off,

$$F_{\mathrm{intra}} = \sum_{i=1}^{M} F_{\mathrm{intra}}^{(i)} = -k_B T \sum_{i=1}^{M} \ln P(\mathbf{X}_i)\,, \tag{2.3}$$

$\mathbf{X}_i$ being the state of the i-th particle. The intermolecular part F_{inter} is given by pairwise additive interaction between particles

$$F_{\mathrm{inter}} = \frac{1}{2}\sum_{i=1}^{M}\sum_{j\neq i}^{M} F_{\mathrm{inter}}^{(ij)} + \frac{1}{2}\sum_{i=1}^{M} F_{\mathrm{inter}}^{(ii)}\,, \tag{2.4}$$

where the second term describes the self-interaction of the particles actually treated on the same basis as the interaction between different particles.

The interaction between two soft particles is given in a mean field manner

$$F_{\text{inter}}^{(ij)} = \hat{\epsilon}\, b^3 \int d^3y \;\tilde{\varrho}_i(\vec{y})\,\tilde{\varrho}_j(\vec{y})\,, \tag{2.5}$$

with $\hat{\epsilon}$ and b^3 being a "contact energy" and a "contact volume", respectively. Here $\tilde{\varrho}_i(\vec{y})$ represents the monomer number density of the i-th particle in the laboratory coordinate system. The parameter b sets the microscopic length scale of the model and is used as length unit, $b = 1$.

The model can easily be generalized for description of polymer mixtures and copolymer melts. In a polymer blend containing components A and B with the polymerisation degree N_A, N_B respectively, polymers of the same type are assumed to interact with the interaction parameter $\epsilon_{AA} = \epsilon_{BB} = \hat{\epsilon}$. The interaction between different species is given by $\epsilon_{AB} = \hat{\epsilon}\,(1+\delta)$, where $\hat{\epsilon}\,\delta/k_BT$ corresponds to the Flory–Huggins parameter χ of the lattice model, see (1.43) in section 1

$$\chi = \frac{1}{k_{\text{B}}T}\left(\epsilon_{AB} - \frac{\epsilon_{AA}+\epsilon_{BB}}{2}\right). \tag{2.6}$$

Positive values of δ make the contacts between unlike monomers less favorable than between like ones. An application of the model to the blockcopolymers needs in addition a modification of the intramolecular part of the free energy accounting for the link connecting A and B blocks into one molecule.

The input quantities $P(\{\mathbf{X}\})$, $\varrho(\vec{x}|\mathbf{X})$ of the soft particle model have to be determined from the underlying microscopic chain model. The choice of the chain model depends on the character of problems to be solved. As this work is devoted to the study of diblock copolymers and it is known that the polymer molecules in the melt approximately behave as ideal chains obeying the Gaussian statistics, the Gaussian chain model is chosen for each block as the underlying microscopic model (see Section 2.2). Additional approximations are used when necessary in order to obtain simple analytical expressions for the input quantities. The kinetics of the phase separation processes is modelled by a discrete time Monte Carlo algorithm based on the actual realisation of the soft particle model.

2.1 Gaussian Sphere Model

The most simple realisation of the soft particle model for homopolymers with the minimal microscopic input is the Gaussian sphere model. We briefly review its main features as derived in [Eudiss]. In this model the polymer molecule is mapped onto a soft sphere with the radius of gyration R_G. The state of the sphere is fully determined by its space location and size, e.g. $\{\mathbf{X}\} = \{\vec{r}, R_G\}$. The input quantitities are the probability distribution $P(R_G, N)$ and the monomer density $\varrho_r(\vec{x}|R_G, N)$, where $\vec{x} = \vec{y} - \vec{r}$ is the position in the center of mass coordinate system. It is assumed that the probability distribution for R_G obeys the following scaling form for large N

$$P(R_G, N) \simeq \frac{1}{\sqrt{N}}\; p\left(\frac{R_G}{\sqrt{N}}\right) \tag{2.7}$$

with

$$\int_0^\infty p(u)\mathrm{d}u = 1\,. \tag{2.8}$$

It has been shown [Eudiss] that the scaling function $p\,(u)$ can be approximated by

$$p(u) = \frac{1}{u\,K_0(2\,d_R)} \exp\left(-\frac{u^2}{a} - d_R^2\frac{a}{u^2}\right)\,, \tag{2.9}$$

where $K_0(z)$ denotes the modified Bessel function of order zero and the coefficients a and d_R are known from fits to the exact moments of second and fourth order in the limit of large N : $\langle R^2\rangle \simeq N/6\,,\ \langle R^4\rangle \simeq (19/540)N^2\,,$ so that $a = 0.08020\,,\ d_R = 1.842$ and $K_0(2d_R) = 0.015923.$ The function (2.9) defines the states in which the particle is fully compressed or stretched as the most improbable.

Turning to the conditional monomer density, one can show that for large N ($N \gtrsim 30$) and for typical R_G (excluding highly stretched chains) the following scaling form applies

$$\varrho_r(\vec{x}|R_G) \simeq \frac{N+1}{R_G^3} f\left(\frac{x}{R_G}\right)\,, \tag{2.10}$$

with

$$f(v) = (3/2\pi)^{3/2}\exp(-3v^2/2) \tag{2.11}$$

that agrees well with Monte Carlo simulation for isolated chains. With the help of (2.10), (2.11) the conditional monomer density reads

$$\varrho_r\,(\vec{x}|R_G) = \frac{N+1}{R_G^3}\,\left(\frac{3}{2\pi}\right)^{3/2} \exp\left(-\frac{3}{2}\frac{\vec{x}^2}{R_G^2}\right)\,, \tag{2.12}$$

which obeys the normalisation condition (2.1). The simple form of $\varrho_r(\vec{x};R_G)$ allows direct integration of the interaction in the intermolecular free energy leading to a generalized Flory–Krigbaum potential [Flo50]

$$F_{\mathrm{inter}}^{(ij)} = \frac{\hat{\epsilon}b^3(N+1)^2}{\left[2\,\pi\sigma_r^2\left(R_G^{(i)\,2} + R_G^{(j)\,2}\right)\right]^{3/2}} \exp\left[-\frac{1}{2\,\sigma_r^2}\frac{(\vec{r}_i - \vec{r}_j)^2}{\left(R_G^{(i)\,2} + R_G^{(j)\,2}\right)}\right]\,, \tag{2.13}$$

for two soft spheres i and j with the gyration radii $R_G^{(i)}$ and $R_G^{(j)}$, located at $\vec{r}_j$ and $\vec{r}_j$, respectively. In (2.13) the parameter σ_r is defined as $\sigma_r^2 = 1/3\,.$

The kinetics of the model is driven by two different Monte Carlo moves:

1. A translation of the position of one particle $\vec{r}_i \to \vec{r}_i + \Delta\vec{r}_i$, where the components of $\Delta\vec{r}_i$ are drawn from a uniform distribution in the interval $[-\Delta r_{\max}/2, \Delta r_{\max}/2]\,,$ where $r_{\max}$ is usually chosen as $r_{\max} = 1/4(N/6)^{1/2}\,.$

2. A size change $R_G^{(i)} \to R_G^{(i)} + \Delta R_G^{(i)}$, where $\Delta R_G^{(i)}$ is uniformly distributed in the interval $[-\Delta R_{G\max}, \Delta R_{G\max}]$ with $\Delta R_{G\max} = 0.5(N/6)^{1/2}$ under the additional constraint $R_G^{(i)} > 0\,.$

We do not discuss this model further, but come back to the basic expressions (2.12), (2.13) when dealing with the disphere model.

2.2 Gaussian Disphere Model (GDM) for Diblock Copolymers

Following the basic idea in previous work [Eudiss] each block in an (AB)-diblock copolymer molecule is proposed to be mapped onto one soft sphere with radius of gyration R^X ($X = A$ or B), see Fig. 2.1. The molecules' orientation is given by the vector $\vec{r} = \vec{r}^A - \vec{r}^B$ connecting the two centers-of-mass of the spheres. Its magnitude $r = |\vec{r}|$ determines the stretching of the molecule under the AB-repulsion. In what follows, the three quantities R^A, R^B and $\vec{r}$ shall be regarded as the only parameters that represent the internal degrees of freedom of one particle and its spatial orientation, that is $\{\mathbf{X}\} = \{\vec{r}, R^A, R^B\}$. In order to express configurational fluctuations of a molecule in terms of these parameters, one has to specify

i) the joint probability densities $P(\vec{r}^A, \vec{r}^B, R^A, R^B)$ for given number of bonds in the A and B block, N_A and N_B, respectively.

ii) the conditional monomer densities $\rho_X(\vec{x}|\vec{r}, R^A, R^B)$ of the block X written in terms of the coordinate $\vec{x}$ relative to the center $\vec{r}^X$ of the sphere. The normalization condition is

$$\int \rho_X \mathrm{d}^3x = N_X + 1\,. \tag{2.14}$$

These densities P and ρ_X are to be derived from a microscopic model of an isolated chain, see below.

The free energy for an ensemble of M molecules is defined according to Eq. (2.2). The intramolecular part resulting from chain entropies with fixed values N_A and N_B reads

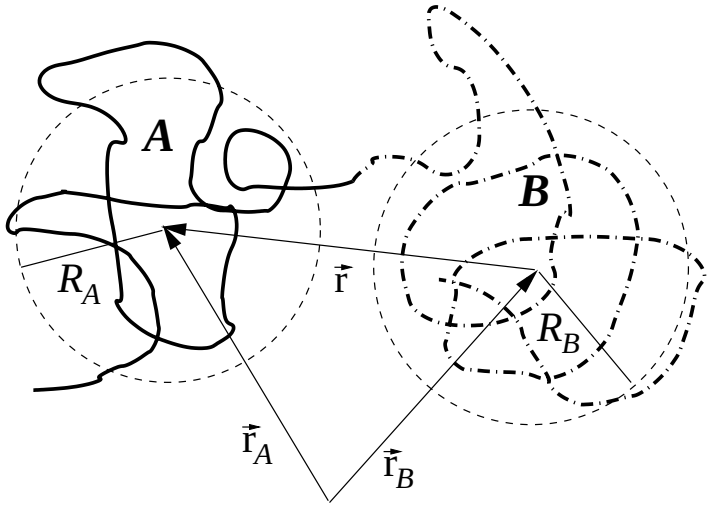

Figure 2.1: Schematic illustration of the Gaussian disphere model. Two blocks A and B of the diblock copolymer molecule are mapped onto two soft spheres with radii R^A, R^B located at $\vec{r}^A$, $\vec{r}^B$ respectively. The distance between the spheres is $\vec{r} = \vec{r}^A - \vec{r}^B$.

$$F_{\text{intra}} = -k_B T \sum_{i=1}^{M} \ln P\left(\vec{r}_i,\, R_i^A,\, R_i^B\right) . \tag{2.15}$$

The intermolecular part of the free energy includes interactions of strength ϵ_{XY} among the blocks of the same and different types ($X, Y = A$ or B),

$$F_{\text{inter}} = \frac{1}{2} \sum_{i,j=1}^{M} \sum_{X,Y=A}^{B} \epsilon_{XY} b^3 \int \mathrm{d}^3\mathrm{y} \rho_{\mathrm{X}}^{\prime(\mathrm{i})}(\tilde{\mathrm{y}}) \rho_{\mathrm{Y}}^{\prime(\mathrm{j})}(\tilde{\mathrm{y}}) \,. \tag{2.16}$$

In (2.16) $\rho_X^{\prime(i)}(\vec{y})$ denotes the X-monomer density of the i-th molecule in the laboratory frame,

$$\rho_X^{\prime(i)}(\vec{y}) = \rho_X\big(\vec{y} - \vec{r}_i^{\,X} | \vec{r}_i^{\,AB}, [R_i^A]^2, [R_i^B]^2\big) \tag{2.17}$$

In the context of microphase transitions, copolymers can be regarded as largely incompressible. Hence the total monomer density

$$\rho_{\text{tot}} = \sum_{i,X} \rho_X^{\prime(i)}(\vec{y}) \tag{2.18}$$

can be approximated by a constant, $\rho_{\text{tot}} = (N_A + N_B + 2)M/V$ with V being the volume of the system. Note that the corresponding constant entropy due to molecular translations need not be included in this approximation.

To complete the definition of the free energy, one has to specify the input functions P and ρ_X. Following the reasoning above, it was proposed to use Gaussian chains as microscopic input, with a few additional approximations that lead to simple analytic expressions. First we consider the probability density P. Here it is assumed that the radii R^A and R^B of one molecule are uncorrelated and described by distributions $P_X(R^X) \equiv P(R^X|N_X)$ obtained from homogeneous Gaussian chains. Thus one can write

$$P(\vec{r},\, R^A,\, R^B) = P_A(R^A) P_B(R^B) W(\vec{r}|R^A, R^B) \tag{2.19}$$

with the probability distribution for the gyration radius of one block in the limit of large N_X ($N_X \gtrsim 30$) of the same form as in the Gaussian sphere model, Eq. (2.7)

$$P_X(R^X) \simeq \frac{1}{\sqrt{N_X}} p\left(\frac{R^X}{\sqrt{N_X}}\right) . \tag{2.20}$$

For the scaling function $p(u)$, the same approximated expression is used as in Eq. (2.9).

For the conditional probability in (2.19), a Gaussian ansatz is made with respect to $\vec{r}$,

$$W(\vec{r}|R^A, R^B) = \frac{3}{2\pi \langle \vec{r}^{\,2} \rangle_{R^X}} \exp\left(-\frac{3\vec{r}^{\,2}}{2\langle \vec{r}^{\,2} \rangle_{R^X}}\right) , \tag{2.21}$$

where $\langle \vec{r}^{\,2} \rangle_{R^X}$ is the variance of $\vec{r}$ for given R^A and R^B which can be calculated exactly,

$$\langle \vec{r}^{\,2} \rangle_{R^X} = 2([R^A]^2 + [R^B]^2) \,. \tag{2.22}$$

Equation (2.21) has been tested in Monte Carlo simulations where the conditional probability $W(r|R^A)$ was obtained from (2.21) by intergrating over the orientations of $\vec{r}$ with $r = |\vec{r}|$ fixed, and by averaging over R^B. Regarding its dependence on R^A, averages were taken over each of eight successive intervals on the R^A axis chosen such that they have equal weights 1/8 with respect to the distribution (2.20). Results are shown in Fig. 2.2 by continuous curves, together with the simulation data represented by black squares. Note that with increasing R^A, the peak positions move to the right, showing that chain realizations with larger R^A imply larger stretchings of the whole molecules.The semilogarithmic plot in the inset confirms a fair agreement between the simulation data and the Gaussian approximation.

Second, we turn to the conditional monomer density ρ_X. As mentioned already, one assumes a spherical shape and ignores any dependence on $\vec{r}$ and on the size of the opposite block, i.e. one proposes $\rho_X = \rho_X(\vec{x}|R^X)$. Then for large N_X the scaling form

$$\rho_X(\vec{x}|R^X) \simeq \frac{N_X + 1}{[R^X]^3} f\left(\frac{x}{R^X}\right) \tag{2.23}$$

applies with the same scaling function $f(v)$ as in the soft sphere model, (2.11). The use of Eq. (2.23) as an approximation in the Gaussian disphere model directly follows the analogous reasoning in the soft ellipsoid model, described in detail in [Eudiss]. To complete the description of the model, we give the expression for the radius of gyration R_G of the total chain, to be

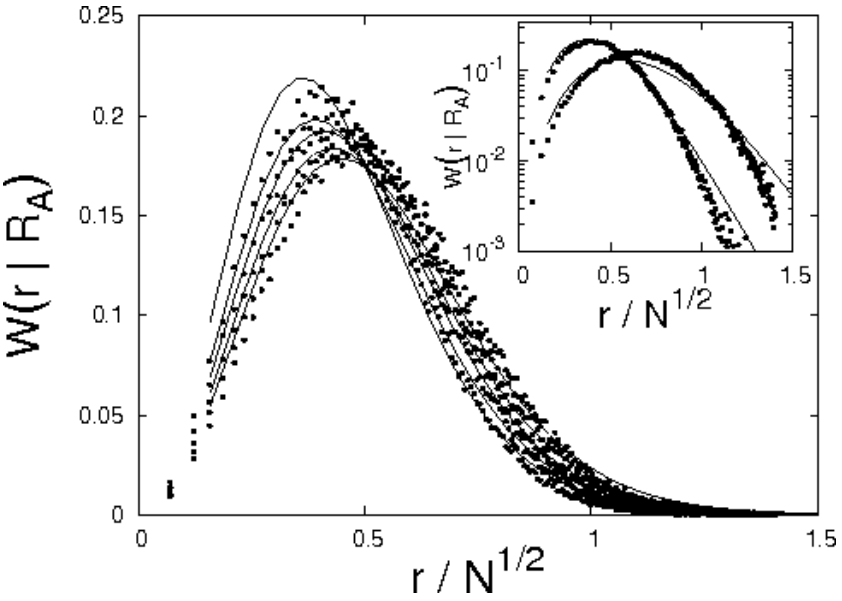

Figure 2.2: Comparision between the conditional probability $W(r|R^A)$ based on the Gaussian approximation (2.21) (continuous curves) with Monte Carlo data for symmetric chains with $N = 100$ (redrawn from [Eudiss], section 4). To display the dependence on R^A, averages have been taken over eight successive (R^A)-intervals, see the text. Different curves refer to the first five of these intervals. With inreasing R^A-values, distributions $W(r|R^A)$ shift towards larger r-values. The inset shows, in the semi-logarithmic representation, the results for the smallest and largest of these eight R^A-intervals, showing that the Gaussian approximation is satisfactory as long as $r^2 \lesssim N$.

derived by simple geometric considerations

$$R_G^2 = f_A[R^A]^2 + f_B[R^B]^2 + f_A f_B \vec{r}^2 \,, \tag{2.24}$$

where $f_X = N_X/N$ and $N = N_A + N_B$. It is clear that this type of the model can be extended to more complicated structures like triblock copolymers, but we will not pursue this here.

So far, for given external parameters N_X, M and V, a free energy F has been constructed which depends on the variables R_i^X and $\vec{r}_i^X$ (giving $\vec{r}_i = \vec{r}_i^A - \vec{r}_i^B$). To model kinetic properties, these variables are changed in a Monte Carlo process. Two types of elementary moves are considered:

1. block translations $\vec{r}_i^X \rightarrow \vec{r}_i^X + \Delta\vec{r}_i^X$ where the components of $\Delta\vec{r}_i^X$ are drawn from a uniform distribution in the interval $[\max(-\Delta\vec{r}_{\max}^X/2, -\vec{r}_i^X),\, \Delta\vec{r}_{\max}^X/2]$ with $\Delta r_{\max}^X = (3/4)(N_X/6)^{1/2}$;

2. size changes $R_i^X \rightarrow R_i^X + \Delta R_i^X$, again with ΔR_i^X uniformly distributed in the interval $[-\Delta R_{\max}^X/2,\, \Delta R_{\max}^X/2]$; $\Delta R_{\max}^X = 0.5(N_X/6)^{1/2}$, but with the additional restriction that $R_i^X > 0$.

All elementary steps have the same a priori probability. Acceptance probabilities are chosen according to the Metropolis algorithm based on the free energy (2.2). In this work we perform calculations using $\epsilon_{AA} = \epsilon_{BB} = \epsilon = k_B T$ and express results in terms of the reduced interaction strength $\chi = (\epsilon_{AB} - \epsilon)/k_B T$.

2.3 Gaussian Ellipsoid Model (GEM)

The soft sphere model for polymer molecules introduced above although being simple and time-saving in computer simulations, omits the orientational degree of freedom of the polymer which can be of interest in studying sufrace phenomena of polymer melts where the polymer was shown to be deformed. Below we describe the soft ellipsoid model for polymers which has been introduced by Eurich and Maass [Eur01], [Eur02] and present main results obtained with this model regarding both dynamic and static properties of polymers and polymer blends. This model accounts for a prolongated shape of the polymer molecule, a fact that was theoretically predicted by Kuhn [Kuh34] and observed in computer simulation [Sol71] and experiment [Hab00].

In this model, a polymer molecule is represented by an ellipsoid whose spatial extension is determined by the eigenvalues $\mathbf{S} = (S_1, S_2, S_3)$ of the gyration tensor $S_{\alpha\beta}$

$$S_{\alpha\beta} = \frac{1}{N+1} \sum_{k=0}^{N} \left(y_\alpha^{(k)} - r_\alpha \right) \left(y_\beta^{(k)} - r_\beta \right) \,, \tag{2.25}$$

where $y_\alpha^{(k)}$ is the α component of the position $\vec{y}^{(k)}$ of the monomer k in the laboratory system and $\vec{r}$ is the position of the center of mass of the chain. The state of the soft ellipsoid particle is determined by the vector $\vec{r}$, the spatial extension of the ellipsoid given by the eigenvalues $\mathbf{S} = (S_1, S_2, S_3)$ and the orientation of the principal axes given by the gyration tensor $S_{\alpha\beta}$, i.g.

$\{\mathbf{X}\} = \{\vec{r}, S_{\alpha\beta}\}$. The input quantity of the model are the distribution density $P(\mathbf{S})$ for the ellipsoid to have eigenvalues $\mathbf{S}$ and the conditional monomer density $\varrho_r(\vec{x}\,|\mathbf{S})$, where $\vec{x}$ is the position in the center of mass coordinate system.

The probability distribution for the eigenvalues $\mathbf{S}$ is assumed to split into probability distributions for the single eigenvalues obeying a simple scaling form similar to that of the soft sphere model

$$P(\mathbf{S}, N) = \prod_\alpha P_\alpha(S_\alpha, N) \sim \prod_\alpha \frac{1}{N}\, p_\alpha \left(\frac{S_\alpha}{N}\right) . \tag{2.26}$$

A similar separation ansatz was suggested for the monomer density

$$\varrho_r(\vec{x}|\mathbf{S}) = (N+1) \prod_\alpha \frac{1}{S_\alpha} f_\alpha \left(\frac{x_\alpha}{S_\alpha}\right) . \tag{2.27}$$

Eurich proposed simple analitical approximations for both scaling functions $p_\alpha\left(\frac{S_\alpha}{N}\right)$ and $f_\alpha\left(\frac{x_\alpha}{S_\alpha}\right)$ which allow direct calculation of the free energy of the system of ellipsoid particles [Eudiss]. The kinetics is modeled by a discrete time Monte-Carlo process, where three types of elementary moves are implemented:

1. translations of the center of mass of particles $\vec{r}_i \to \vec{r}_i + \Delta\vec{r}_i$, where the components of the vector $\triangle\vec{r}_i$ are randomly drawn from the interval $[-\Delta\vec{r}_{\max}/2,\, \Delta\vec{r}_{\max}/2]$ with $\Delta r_{\max} = (1/4)(N/6)^{1/2}$;

2. random rotations of particles in the steradian 4π;

3. changes in the particles shape $S_\alpha^{(i)} \to S_\alpha^{(i)} + \Delta S_\alpha$ with ΔS_α uniformly distributed in the interval $[\max(-\Delta S_{\max,\alpha}/2, -S_\alpha), S_{\max,\alpha}/2]$ where $\Delta S_{\max,\alpha} = 0.5\,\langle S_\alpha\rangle$, $\langle S_\alpha\rangle$ being the average ideal characteristic size along the α axis.

All the elementary moves are attempted with the same apriory probability.

2.4 Main Results Obtained with the Gaussian Ellipsoid Model

In this section we discuss the main results obtained with the Gaussian Ellipsoid Model (GEM) when studying static and dynamic properties of polymers and polymer mixtures both in the bulk and slab geometries [Eur01], [Eur02].

2.4.1 Homogeneous Systems

First a system of individual self-interacting ellipsoid particles is considered to simulate the properties of one separated polymer molecule. As the free energy is treated on a Flory-type footing with excluded volume effects, see Eqs. (2.2)-(2.5), one would expect that the mean gyration radius $\bar{R}_G$ scales with the chain length N and the interaction parameter ϵ as $\bar{R}_G^2 \sim \epsilon^{2/5} N^{6/5}$ [deGen]. This behaviour was indeed recovered in simulations, as shown in Fig. 2.3*a*

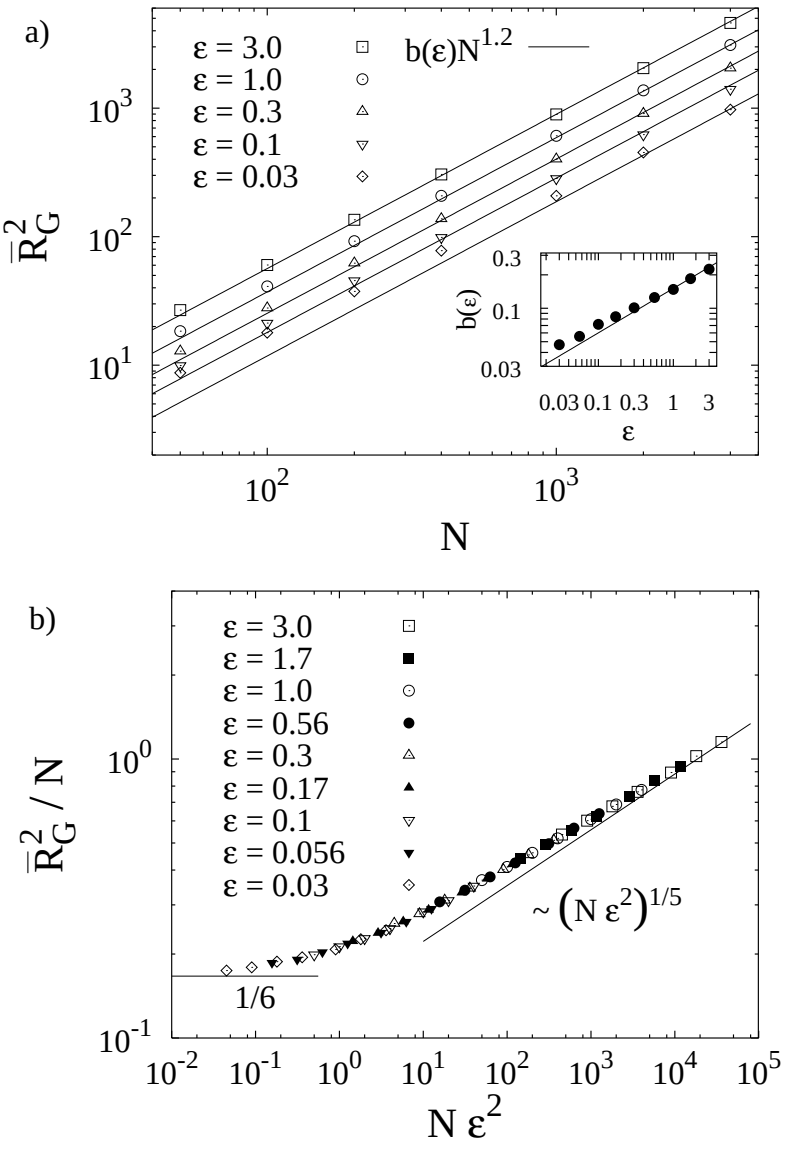

Figure 2.3: a) Mean squared radius of gyration of individual self–interacting ellipsoid particles versus the chain length N at different values of ϵ. The lines represent the Flory result $\bar{R}_G^2 = b(\epsilon)N^{6/5}$. The inset shows the dependence of the prefactor $b(\epsilon)$ on ϵ which turns out to be close to $b(\epsilon) \propto \epsilon^{2/5}$. b) Crossover from Gaussian (smaller values of ϵ) to Flory type (larger ϵ) behavior (after [Eudiss], section 5).

where the quantity $\bar{R}_G^2$ is plotted as a function of N ($N = 30, ..., 400$) at different values of the interaction parameter ϵ .

Fig. 2.3*b* shows a plot of $\bar{R}_G^2/N$ vs. $N\epsilon^2$ exhibiting a crossover from the Flory (large values of ϵ) to the Gaussian behavior (smaller values of ϵ) with $\bar{R}_G^2 \sim N^{1/2}$. All the data points perfectly fit on a single curve which tends to a constant value 1/6 at small $N\epsilon^2$ and the expected power law $(N\epsilon^2)^{1/5}$ at large $N\epsilon^2$.

Turning to the system with interacting particles in a melt, we note that at the dilute monomer

concentrations $c < c_*$ where $c_* \sim \epsilon^{-3/5} N^{-4/5}$ is some overlap concentration [deGen], one would expect the Flory type scaling $\bar{R}_G^2 \sim N^{6/5}$ because the particles almost do not interact with each other. When increasing c, the particles start to interpenetrate each other and at dense concentrations $c > c_*$, one enters a region where the intramolecular interactions are compensated by the intermolecular forces and the Gaussian scaling $\bar{R}_G^2 \sim N^{1/2}$ is recovered. The whole behavior can be represented by the following scaling formula:

$$\bar{R}_G^2(N, \epsilon, c) = \epsilon^{2/5} N^{6/5} f\left(c\, \epsilon^{3/5} N^{4/5}\right) , \tag{2.28}$$

where $f(u) \to$ const for $u \ll 1$ and $f(u) \to u^{-1/4}$ for $u \gg 1$, see [deGen]. This crossover was indeed observed in the simulations as depicted in Fig. 2.4 where the quantity $\bar{R}_G^2 / N^{6/5}$ is plotted against the product $c\, N^{4/5}$ for $\epsilon = 1.0$.

2.4.2 Polymer Mixtures

A binary mixture of polymers of types A and B was studied at the monomer concentration $c = 0.85$ (dense systems) and $\epsilon = 0.85$. The system consists of M_A A-particles and M_B B-particles with $M = M_A + M_B$ being the total number of particles. The particles are assumed to have the equal length $N_A = N_B = N$, so that the monomer concentrations of the respective components are $\phi_A = M_A/M$ and $\phi_B = M_B/M$. The simulations were carried out in the grand-canonical ensemble with M fixed and fluctuating ϕ_A and ϕ_B.

One can define the order parameter for the demixing of the two components by the quantity $\langle \phi \rangle = \langle |\phi_A - \phi_B| \rangle$ where the brackets mean the ensemble average. In the demixed phase $\langle \phi \rangle$ will be close to unity whereas in the homogeneous mixed phase $\langle \phi \rangle$ will tend to zero.

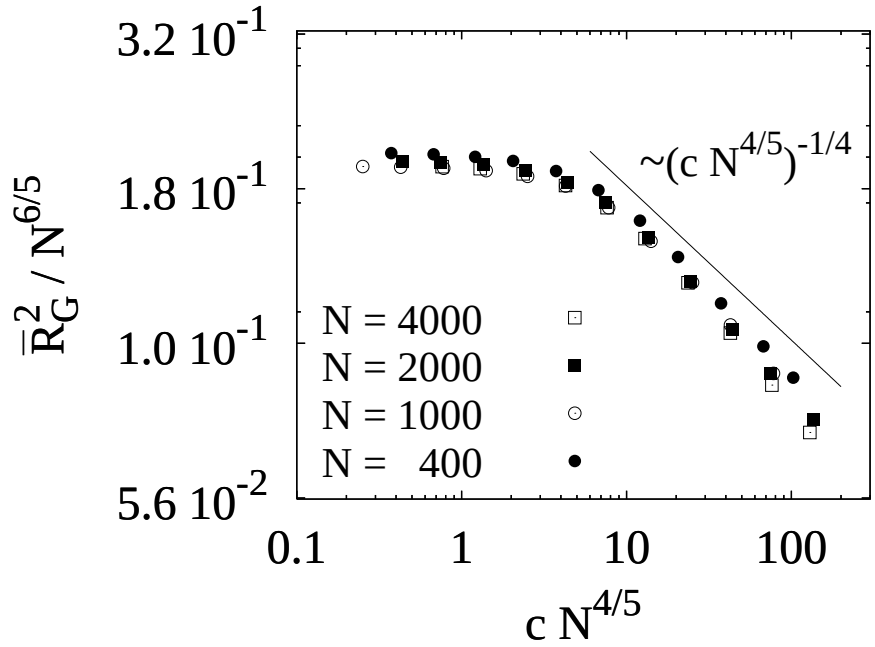

Figure 2.4: Crossover from dilute to dense systems of interacting ellipsoid particles showing overall behavior predicted by the scaling relation (2.28) (after [Eudiss], section 5).

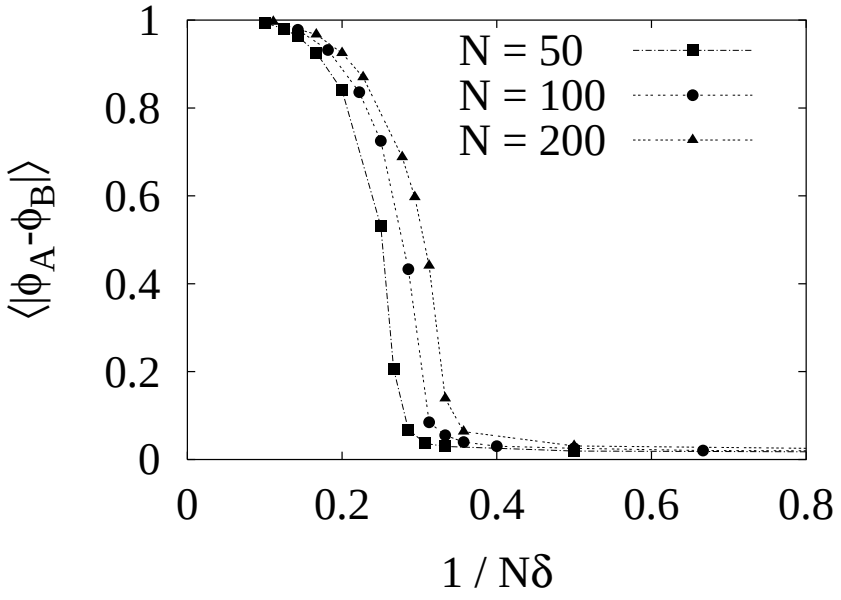

Figure 2.5: Coexistence curves shown in terms of the order parameter $\langle|\phi_A - \phi_B|\rangle$ versus $1/N\delta = k_{\mathrm{B}}T/N(\hat{\epsilon}_{AB} - \hat{\epsilon})$ in polymer mixtures $N_A = N_B = N$ with $N = 50, 100$ and 200 (after [Eudiss], section 5). The transition temperature scales roughly with $1/N$.

Fig. 2.5 shows the phase behavior in terms of the order parameter $\langle\phi\rangle$ and $1/N\delta$, where $\delta = (\hat{\epsilon}_{AB} - \hat{\epsilon})/k_BT$ for three systems of the chains with the lenght $N = 50, 100$ and 200. The phase transition can qualitatively be estimated to lie in the region where $\langle\phi\rangle$ has values between zero and about 1. A clear tendency can be observed in the plot showing a shift of the transition point towards larger values of $1/N\delta$ when increasing the chain length N. A similar scaling of the critical temperature with N was also found in experiment [Geh92] and computer simulations [Bin81], [Bin83].

The GEM was also capable of catching shrinkage of particles belonging to the minority phase due to the tendency of the monomers belonging to the minority phase to reduce the number of unfavorable contacts.

Another interesting feature is the spinodal decomposition in the symmetric system ($\phi_A = 0.5$) that initially was at equilibrium at the mismatch parameter $\delta = 0$ which was then suddenly increased. The following spontaneous coarsening was studied using the structure factor $S(\vec{k}, t)$ whose definition is given in the Appendix, Eq. (A.3). As the structure factor in the disordered melt has rotational symmetry and depends only on $k = |\vec{k}|$, a spherical averaging was made; for details on the analytic expresion of $S(k, t)$ in the GEM, see [Eudiss].

The structure factor was shown to develop a peak at the characteristic demixing length, which remained at the same position at the initial times with the maximum of the peak growing up. At later times of the demixing, the peak position was gradually shifting towards smaller values of k with the peak maximum keeping increasing.

To study the demixing quantitatively, the first moment k_1 of the structure factor defined by $k_1(t) = \int dk\, kS(k,t) / \int dk S(k,t)$ was calculated from the simulation data, see Fig. 2.6.

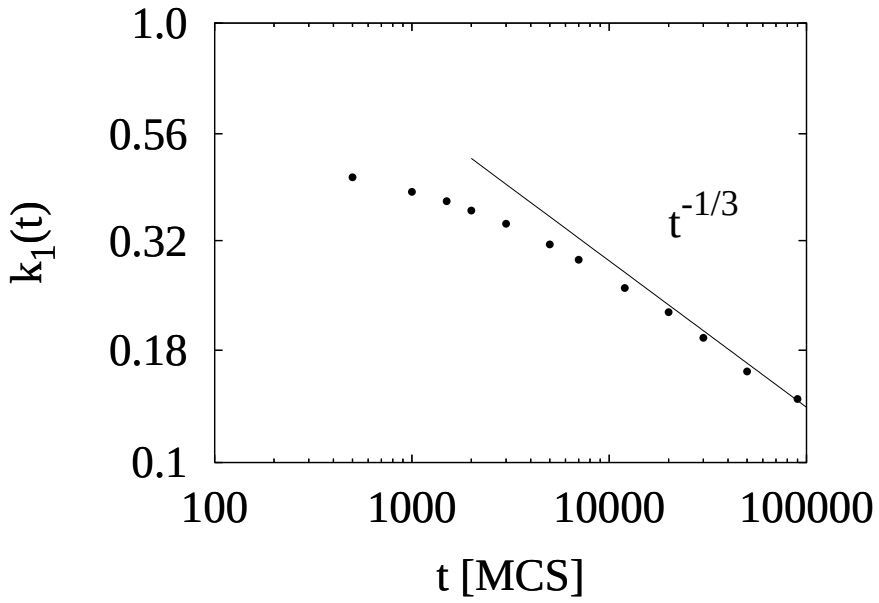

Figure 2.6: The first moment of the structure factor $k_1(t)$ versus time during the coarsening process in the symmetric system of soft-ellipsoid particles of types A and B (after [Eudiss], section 5). The quantity $k_1(t)$ serving as an estmation of the characteristic length of the demixing tends to the Lifshitz-Slyozov behavior $k_1(t) \sim t^{-1/3}$ at later stages of the process.

The Lifshitz-Slyozov behavior $k_1(t) \sim t^{-1/3}$ [Bra94] was observed at the later times of the coarsening, see the plot.

The GEM was also checked against the behavior of the polymer systems confined between two neutral walls modeled by exponential potentials. Elipsoid particle near the wall were found to be aligned parallel to the wall. Additional effects of strong oblating of the particle in the vicinity of the wall were observed when considering the eigenvalues of the gyration tensor as a function of the distance from the wall.

The phase separation in the mixture of two components A and B was investigated in the slab geometry. Here the dependence of the critical temperature $T_c(L_z)$ below which the demixing happens on the film thickness L_z is of interest. The Ginzburg–Landau mean-field theory [Tag93] predicts that $T_c(L_z) - T_c(\infty) \sim 1/L_z$ in the limit $L_z \ll Nb$. The critical temperature $T_c \sim 1/\delta$ was roughly estimated from an extrapolation of the coexistence curve to zero, see Fig. 2.7 where the order parameter $\langle\phi\rangle = \langle|f_A - f_B|\rangle$ is plotted against δ. As shown in the inset to the plot, $T_c(L_z)$ indeed follows the Ginzburg–Landau law.

2.5 Summary

In this section following [Eur01], [Eur02] we have reviewed the main concepts of coarse-graining as applied to the description of polymer systems. We explained the general definition of the soft–particle model and showed its main realizations based on the Gaussian chain as the input model, e.g. the soft-sphere model (the simplest realization), the disphere model for diblock

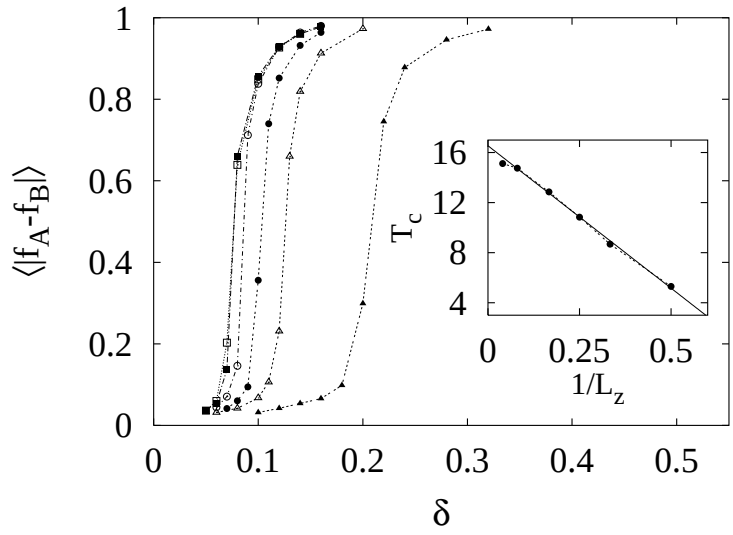

Figure 2.7: Coexistence curves for A and B components confined between two neutral walls for different film thicknesses $L_z = 25(\square)$, $12.5(\blacksquare)$, $6(\circ)$, $4(\bullet)$, $3(\triangle)$, and $2(\blacktriangle)$ (after [Eudiss], section 6). The critical temperature as a function of $1/L_z$ is plotted in the inset.

copolymers, and the Gaussian ellipsoid model. Main results obtained with the GEM were presented, where a good agreement with the theory and experiment was found regarding the static and dynamic properties of polymers and polymer mixtures in the bulk and slab geometries.

3 Diplock Copolymers: Structure Factor in the Bulk

In this and the following section we test the GDM against bulk properties of chain-like copolymer molecules, a subject well known from extensive model studies [Bin81], [Fre87], [Mur98a]. We will show that despite its simplicity the GDM accounts for a remarkable set of both structural and diffusion properties connected with microphase separation.

In a first step, we discuss the static properties of the systems of interest both in the disordered melt and in ordered phases. We will calculate the static structure factor to monitor the transition from the disordered regime towards the ordered phase and find a shift of the order-disorder transition (ODT) point under changing the chain legth. The functional form of the structure factor corresponding to the density fluctuations in the disordered melt will be compared with the predictions of Leibler [Lei80], and Fredrickson and Helfand [Fre87]. We will also prove that the lamellar spacing of the symmetric molecules λ normalized by the factor $N^{0.5}$ scales well with the product χN and compare the calculated scaling exponents with theoretical predictions.

All simulation results in this section are for systems with $M = 4000$ molecules, the system is a cube with the size $L = (MN/\rho_{tot})^{1/3}$. The considered chain lengths are in the range $N = 60, ..., 300$, the total average monomer density is kept constant $\rho_{tot} = 0.85$. The calculated quantities are time averages taken after equilibration of the system; in addition we make an averaging over three independent runs in the ordered phase.

3.1 Equilibrium Structure Factor and the Order–Disorder Transition

The most important quantity to characterize the short- and long-range ordering in the system is the static structure factor which we define through the density correlation function of A-monomers:

$$S(\vec{k}) = \frac{V}{MN_A} \int d^3r \, \langle \rho_A(\vec{r}) \rho_A(0) \rangle e^{i\vec{k}\cdot\vec{r}} \,, \tag{3.1}$$

where $V = L^3$ is the volume of the system. The structure factor is useful because it is both experimentally measurable and predicted by the weak segregation theories to have a specific form discussed below. The density $\rho_A(\vec{r})$ in (3.1) is expressed in the GDM as a sum over individual molecules, see (A.5). For details on the calculation of the structure factor for the GDM, see Eq. (A.10) in Appendix A. The simulations are performed in the systems with periodic boundary conditions, which allows the following set of the components of the vector $\vec{k}$: $\vec{k}_{n_x,n_y,n_z} \equiv (k_x, k_y, k_z) = (2\pi n_x/L, 2\pi n_y/L, 2\pi n_z/L)$ with $n_x, n_y, n_z = 1, 2, ..., 20$, where due

to reflection symmetry we consider only positive values of n_x, n_y, n_z, and restrict the largest values to 20 .

The diblock copolymer melt is a fluid, therefore the disordered phase is fully isotropic and shows no preferred direction in $\vec{k}$ space. The instability of the system upon approaching the order-disorder transition point $\chi = \chi_c$ should show up in a divergence of $S(\vec{k}_c^*)$ according to the Leibler theory. As long as the system remains disordered, (3.1) depends only on $|\vec{k}|$, so it is sufficient to study the spherical average of the structure factor. We define the spherically averaged structure factor as a sum of (3.1) over all vectors $\vec{k}$ which lie in a shell of thickness $\triangle k$ at the distance k from $\vec{k} = (0, 0, 0)$:

$$S(k) = \frac{1}{N_{k,\triangle k}} \sum_{k \le \sqrt{k_x^2+k_y^2+k_z^2} < k+\triangle k} S(\vec{k}) \,,$$

where $N_{k,\triangle k}$ is the number of points in the shell. The thickness of the shell $\triangle k$ can be made even smaller than $2\pi/L$ to have a better resolution in k. The spherical averaging of the structure factor in the disordered melt is discussed in Appendix C.

In the disordered phase, the structure factor $S(k)$ displays a peak at $k = k^*$ that directly determines the characteristic length of the A-monomer density fluctuations, the magnitude of the maximum $S(k^*)$ reflects the degree to which A and B monomers are separated into A- and B-rich regions.

As mentioned above, $S(k)$ is calculated at a discrete set of k only; to approximate the values of k^* and $S(k^*)$, we use the following fitting function suggested by previous work [Bin81]:

$$NS^{-1}(k) = \frac{1}{\alpha}[F(k\tilde{R}_G) - \delta] \,, \tag{3.2}$$

where

$$F(x) = \frac{x^4}{2}\left(\frac{x^2}{4} + e^{-x^2/2} - \frac{e^{-x^2}}{4} - \frac{3}{4}\right)^{-1} \,. \tag{3.3}$$

Equation (3.2) generalizes the form of the structure factor from Leibler's random phase approximation, which in our notation amounts to setting $\alpha = 1/2$, $\tilde{R}_G = R_G$ and $\delta = 2\chi N$. In the Leibler theory, the copolymers are assumed to behave as Gaussian chains in the disordered melt up to the ODT so that the radius of gyration R_G as well as the position of the peak of the structure factor are not affected by increase of χ. The lamellar ordering sets in at the critical value $(\chi N)_c^{\mathrm{L}} = 10.5$, connected with a divergence of $S(k)$ at $k = k_c^\star$ with $k_c^\star R_G = 1.95$. We regard $\alpha, \tilde{R}_G$ and δ as fitting parameters, which are to be determined from the behavior of $S(k)$ around its main peak at $k_\star$.

In Fig. 3.1, data points of the spherically averaged structure factor S(k) and the corresponding fitting curves are displayed for symmetric chains of lenght $N = 120$ in the disordered phase. The values of the fitting parameters $\alpha, \tilde{R}_G$, and δ used in the plot are given in Table 3.1.

As seen from the Fig. 3.1, in the vicinity of the peak and towards small k a good fit is achieved, whereas at larger k the data points fall below the continuous curve where according to (3.2) $S(k) \sim 1/k$. This is to be expected because the intramolecular connectivity is not taken into account by assuming Gaussian monomer densities within each block. This behavior is obviously an artefact of the model which neglects the monomer density fluctuations on the

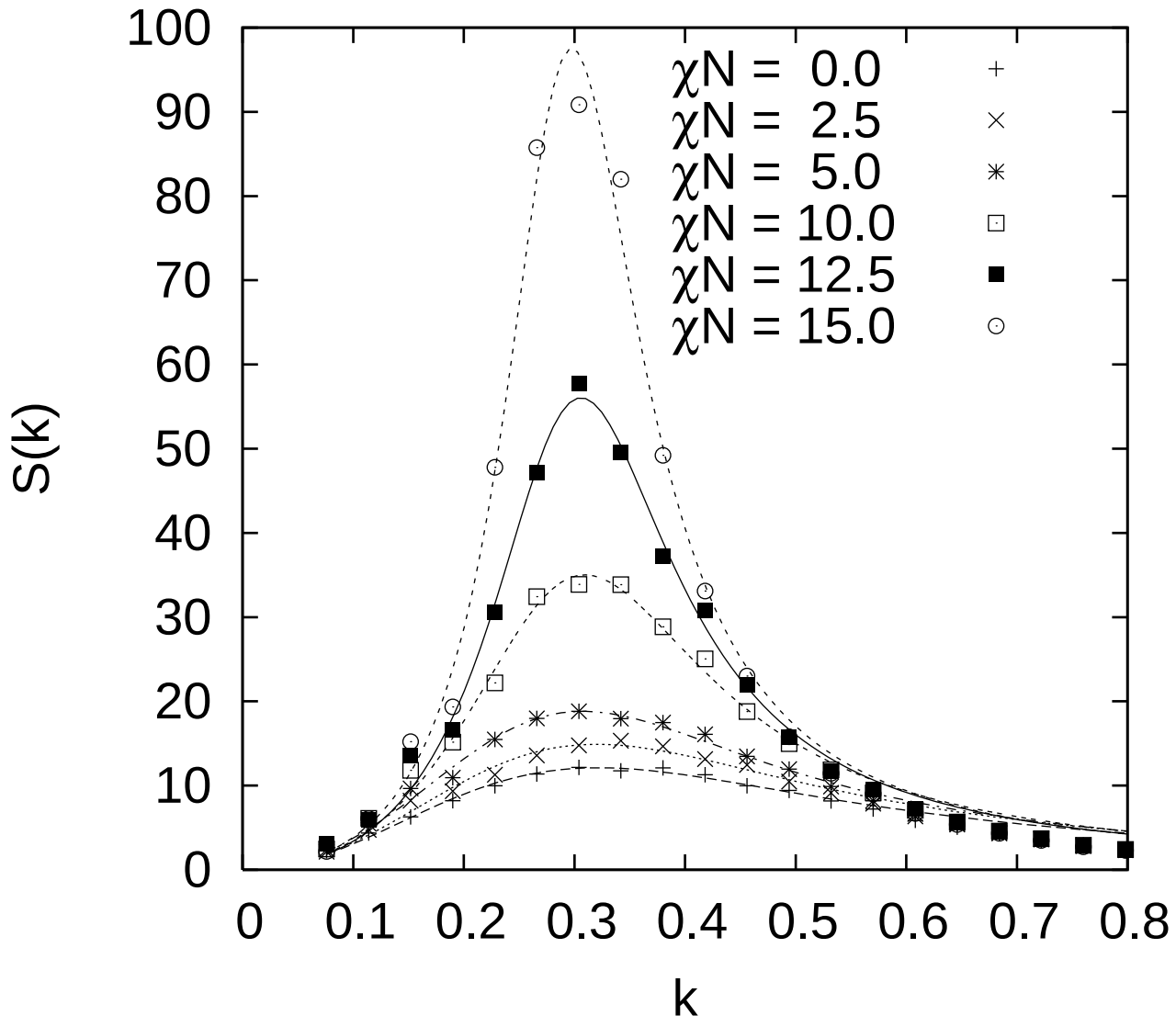

Figure 3.1: Simulated structure factor $S(k)$ in the disordered melt of symmetric chains of length $N = 120$ at different χN below the ODT. Continuous curves are fits to Eq. (3.2). The position of the peak shows a slight shift towards smaller k when going into the instability region.

χN	0.0	2.5	5.0	10.0	12.5	15.0
α	1.9	1.8	1.9	1.6	1.4	1.5
δ	2.1	6.4	8.9	15.5	17.9	19.2
$\tilde{R}_G$	6.1	6.1	6.3	6.3	6.4	6.5

Table 3.1: Parmeters for fitting the generalized Leibler function (Eq. 3.2) to structure factor data in Fig. 3.1.

scales less than the average radius of gyration of one block. An analytical consideration, see Eq. (A.10) in Appendix A, predicts an exponential drop in the structure factor at larger values of k

$$S(k) \sim \exp\left(-\frac{1}{3}k^2[R^A]^2\right) \tag{3.4}$$

with R^A being the mean radius of gyration of the A-block.

Note that the data points in Fig. 3.1 lie a little above the fitting curves at k close to 0. We suspect this feature to be an evidence of breaking down the incompressibility assumption of the Leibler theory [Lei80] clearly seen by very small fluctuations of the total monomer density discussed below, see Fig. 3.6. Analysis of the collective structure factor in the zero wave vector limit, where according to Eq. (A.10) $S(k=0) \neq 0$, shows that the large scale compressibility of our actual model is significally reduced relative to the case of noninteracting chains, but still comparable to that of an ideal gas consisting of individual monomers.

The radii of gyration of individual A-blocks entering the Eq. (A.10) determine the behavior of the structure factor and the position of its peak. The shift of the peak position experimentally observed and also seen in Fig. 3.1 in the disordered phase when increasing χ can partly be explained by deformation of the block sizes. Note that the structure factor in Fig. 3.1 exhibits a peak at $k_* \neq 0$ even in the limit of $\chi = 0$, or equivalently at an infinite temperature. This feature is opposite to a two-component melt of A and B polymers and follows from the connection between A and B blocks of the chain, inducing local correlations in A (or B) monomer density even at $\chi = 0$.

The physical meaning of the parameters α, $\tilde{R}_G$, and δ entering the fit function (3.2) is to allow for a shift in the peak position $k^\star = 2\pi/\tilde{R}_G$ relative to the Leibler value and a deviation of the maximum value $S(k^\star)/N$ from scaling with χN. Indeed, our results in Fig. 3.1 reflect a downward shift in $k^\star$ with increasing χ, starting with $k^* R_G \simeq 1.8$ for $\chi = 0$. Qualitatively, this downward shift agrees with previous calculations [Gre96], [Hof97a], but the effect is smaller than in these works. Moreover, when plotting $NS^{-1}(k^*)$ from simulations with different N against χN, see Fig. 3.2, linear extrapolation to zero yields an instability of the disordered phase at a critical value $(\chi N)_c$ that increases with decreasing the chain length N. This trend is qualitatively consistent with the Fredrickson and Helfand theory predicting $(\chi N)_c^{\mathrm{FH}} - (\chi N)_c^{\mathrm{L}} \propto N^{-1/3}$ [Fre87]. In our model the critical value for the longest chains ($N = 300$) as estimated by a linear extrapolation of $NS^{-1}(k_*)$ to zero is $(\chi N)_c \simeq 12$ to 14. For the chains with $N = 120$ used further in this work, the position of the ODT $(\chi N)_c$ is estimated to lie between 15.0 and 16.5, see Fig. 3.2. It also appears from Fig. 3.2 that the normalized inverse height of the peak $NS^{-1}(k^*)$ shows a good scaling with the product χN sufficiently below the ODT according to previous simulations [Bin81].

In Fig. 3.3, we show the position of the maximum k^* multiplied by the radius of gyration of the whole chain R_G which is expressed in the GDM through the radii of gyration of individual blocks R^A and R^B and the distance between the centers of mass $\vec{r}$ as $R_G^2 = 0.5[R^A]^2 + 0.5[R^B]^2 + 0.25\vec{r}^{\,2}$. We find that the data scale well with χN, in agreement with pevious work [Bin81], [Mur98a]. However, in the limit $\chi = 0$, the values of $k^* R_G$ lie below the Leibler value 1.95 predicted by mean field theory and found in other simulations, [Bin81], [Mur98a]. For the chain lenghts $N = 62, 120$, $k^* R_G$ is close to 1.8, while for the larger chains $N = 300$, $k^* R_G$ is about 1.76. We attribute this feature to the fact that the modeling of the diblock copolymer as two spheres lowers the elongation of the molecule in the direction of its symmetry axis $\vec{r}$ at $\chi = 0$, so that

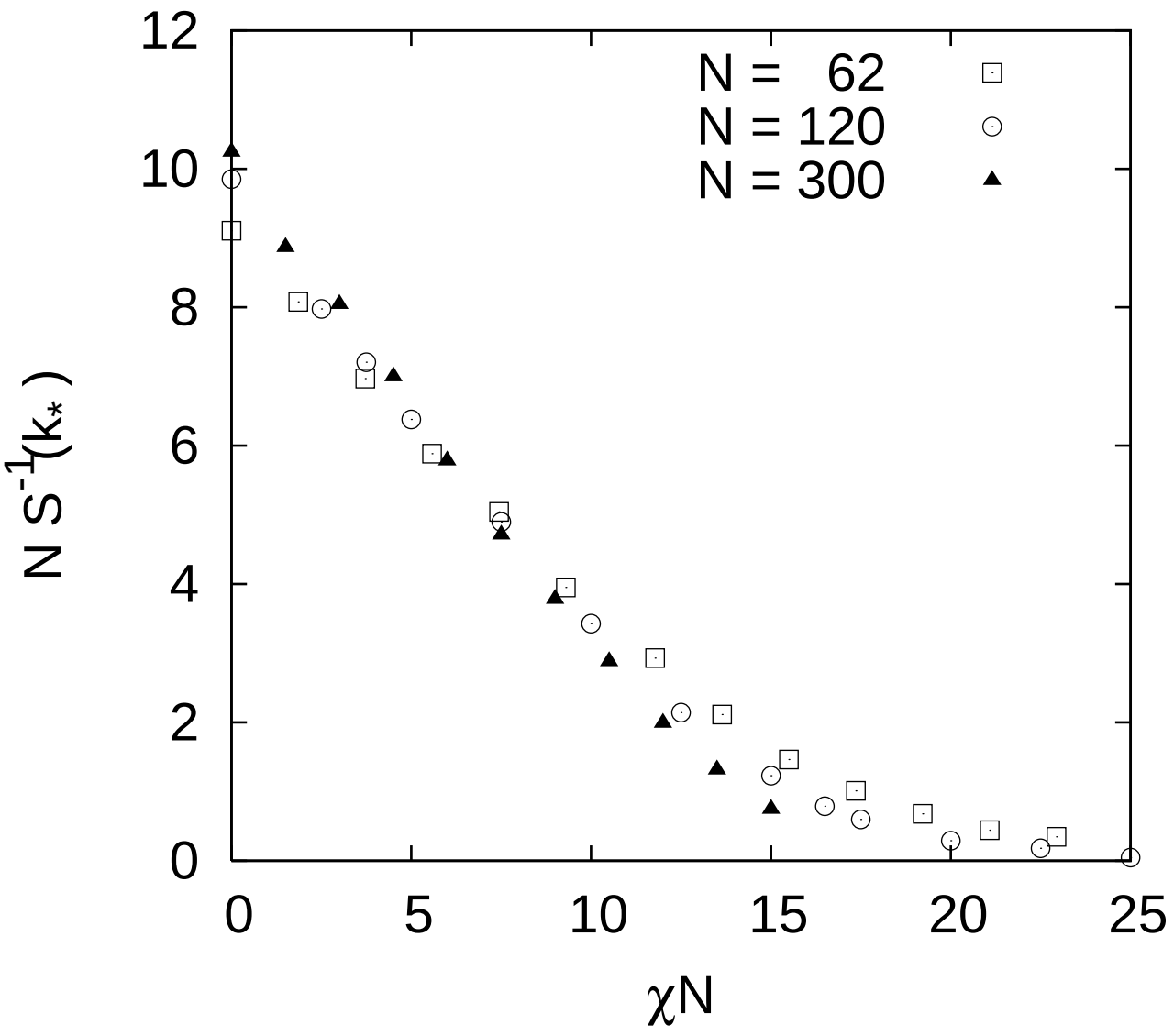

Figure 3.2: Normalized inverse maximum of the structure factor versus χN for three different chain lengths $N = 60, 120, 300$. Note that the scaling of $N\,S^{-1}(k)$ with χN expected from the Leibler theory, breaks down in the instability region mirrored in the shift of $(\chi N)_c$ towards higher values when decreasing the chain length N.

the radius of gyration has smaller values than those in more realistic models [Bin81], [Mur98a]. When approaching the ODT, $k^* R_G$ continuously becomes smaller and is little below 1.7 at the ODT, which is close to the result of Murat and Kremer. The fitting parameter δ plotted in Fig. 3.4 for various chain lengths also shows a good scaling with χN .

Ordered structures spontaneously forming under a quench from the disordered state to a value χN above but still close to $(\chi N)_c$, display a multidomain pattern with various lamellar periods and weak segregation, i.e. a smooth variation of the respective monomer densities when passing from A-rich to B-rich domains. Figure 3.5 exemplifies the spherically averaged

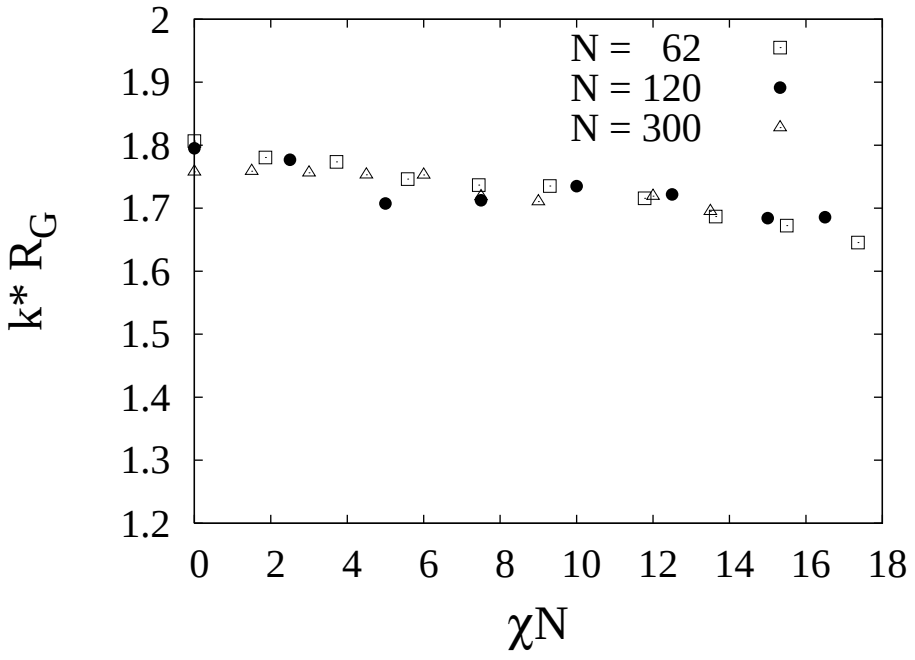

Figure 3.3: $k^* R_G$ versus χN for three different chain lengths $N = 60, 120, 300$. All the data are below the Leibler value 1.95 and show futher decrease when increasing χN.

structure factor for $\chi N = 25$ (the chain length $N = 120$). The position of the sharp peak at $k_\star = 2\pi/\lambda$ reflects the averaged lamellar periodicity λ.

In Fig. 3.6 we plot the A- and B-monomer number densities averaged in xy plane, $\varrho_X(z) = \int dxdy\varrho_X(x, y, z)$ where X stands for A and B, in the system of the geometry $L_x = L_y = 71.27$ and $L_z = 4\lambda$ (number of molecules $M = 4000$). The lamellar period was estimated from the peak position $S(k)$, $\lambda = 2\pi/k_\star$. As there are always several domains of different oriented lamellae in the weak segregation regime, the initial state here was an artificial lamellar structure oriented perpendicular to the z direction. The initial configurations were prepared in the way that the radii $\vec{r}_j$ of the particles lie along the z-axis with their centers of mass being randomly located at the isosurfaces of the lamellar structure. The radii of gyration R_j^A, R_j^B of individual blocks as well as $\vec{r}_j$ were taken out from the equilibrated systems with the same χ. In the next section we will discuss these artificially created ordered configurations in more details.

The system was then left to equilibrate for 7000 MCS after which the density profiles were calculated. Note that the density $\varrho_A(z)$ does not vanish so that there are always A-monomers present in B-rich regions (minima of $\varrho_A(z)$). The peaks of $\varrho_A(z)$ are also lower than the mean value 0.85, which is caused by the presence of some B-monomers in A-rich regions. The total monomer number density $\varrho_{tot}(z) = \varrho_A(z) + \varrho_B(z)$ presented as a dotted line in Fig. 3.6 does not remain constant but fluctuates showing minima at the boundaries of the A- and B-rich regions. We will discuss in the following whether this fact breaks the incompressibility assumption common in the mean field theories. One can distinguish also the double–peak structure of the maximum of the $\varrho_{tot}(z)$ mirroring the layering of the A and B-blocks in the xy plane along the z axis.

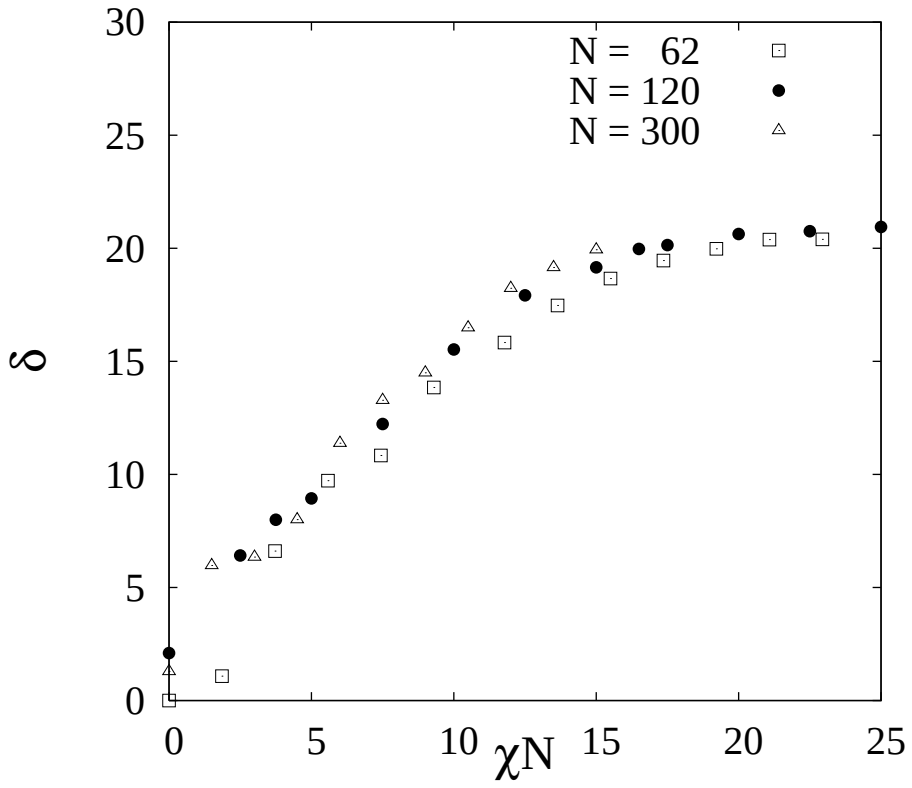

Figure 3.4: Scaling of the fitting parameter δ, Eq. (3.2) with χN plotted for three different chain lengths $N = 60, 120, 300$.

Going to the strong segregation, larger scale oriented lamellae with sharp interfaces develop. This leads to higher-order peaks in $S(k)$ and further increase in the peak hight both seen in Fig. 3.7, where we plotted the structure factor for $\chi N = 54$ in the system with the chain length $N = 120$. The position of the main peak is shifted towards smaller k relative to that of the system $\chi N = 25$, Fig. 3.5. Note the absence of the second order peak due to the arrangement of blocks inside the domains. To show the lamellar structure in the real space, we extracted $\varrho_A(\vec{r})$, $\varrho_B(\vec{r})$ from the system configurations and defined an isosurface as a surface at which the A-monomer number density equals the B-monomer number density $\varrho_A(\vec{r}) = \varrho_B(\vec{r})$. The isosurfaces for the lamellae in the system with $N_A = N_B = 60$ at $\chi N = 54$ are shown in Fig. 3.8. They appear to be well-developed almost flat surfaces with some defects visible as connections between neighbouring planes. These defects are actually lamellae with a different orientation which are still present in the system and do not dissapear when we let the simulation run further.

In Fig. 3.9 we present the A- and B-monomer density profiles along the z direction calculated in the way similar to $\chi = 25.0$ (system geometry $L_x = L_y = 77.92$ and $L_z = 3\lambda$, $M = 4000$). Now the peaks of the density profiles are very close to the mean value 0.85 and the minima show no presence of A-monomers in B-rich regions. Note also that the maxima have a well pronounced two-peak structure reflecting the arrangement of the blocks mentioned before. The total monomer number density (dotted line in Fig. 3.9) has more pronounced minima than in

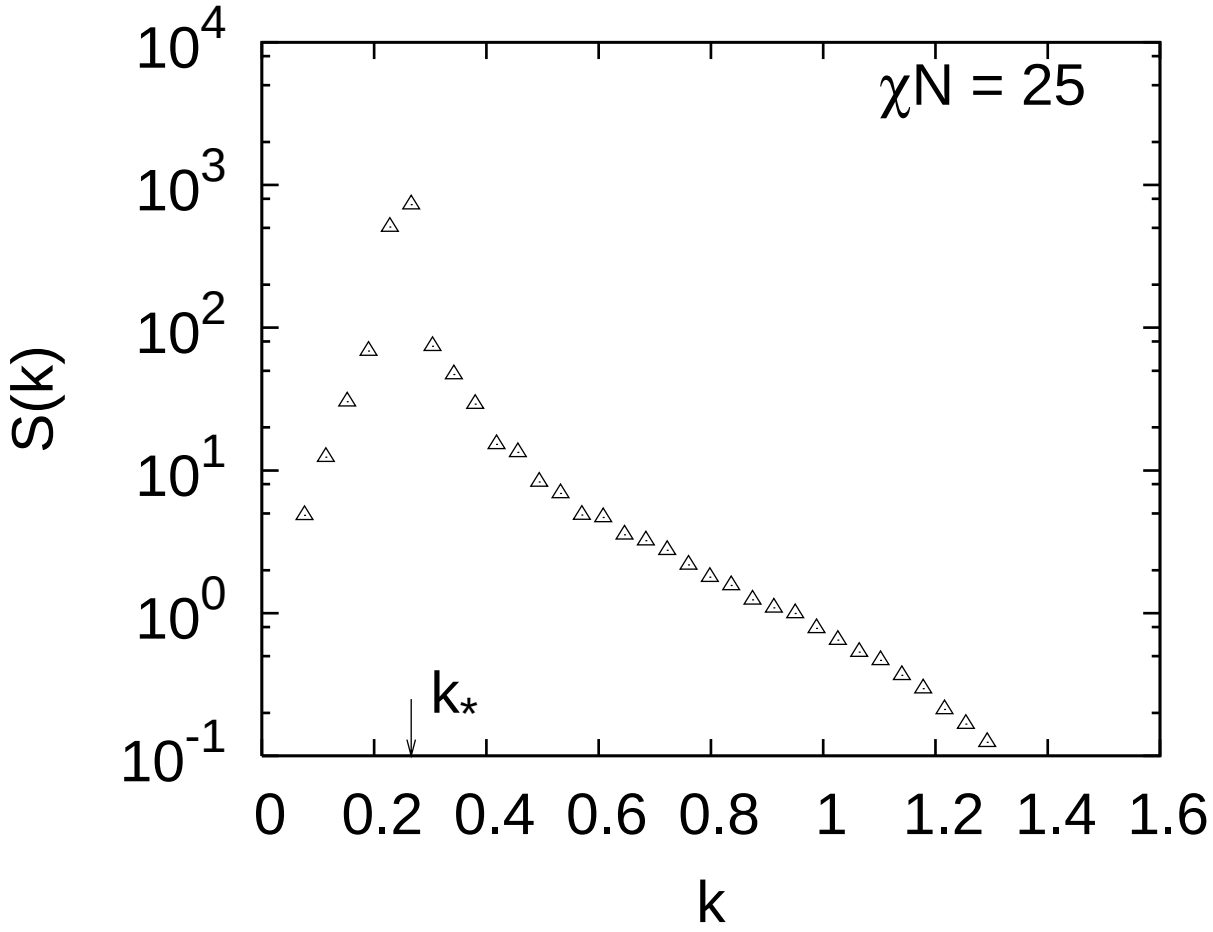

Figure 3.5: Spherically averaged structure factor in ordered phases. Lamellar phase with $\chi N = 25$ (weak segregation).

the weak segragation regime mirroring the well developed isosurfaces between A and B-rich regions which reduce the energetically unfavorable contacts between monomers of different types.

Obviously, the peak position of the structure factor $k_\star$ is significantly smaller than in the disordered state of molecules with the same chain length, due to their stretching under alignment in the ordered lamellae. In the GDM, chain stretching is described by the parameter $r = \langle \vec{r}^{\,2} \rangle^{1/2}$. Its dependence on χN (with N fixed) is plotted in Fig. 3.10, showing a pronounced increase in the vicinity of the ordering transition and a subsequent weaker increase, as χN rises further. For $\chi = 0$, one recovers $r^2 = 2(\langle [R^A]^2 \rangle + \langle [R^B]^2 \rangle)$, see Eq. (2.20). The averaged radii of gyration $\langle [R^X]^2 \rangle^{1/2}$ of individual blocks become decreased a little in the disorderd melt due to some shrinking of individual blocks also observed in work of [Hof97a].

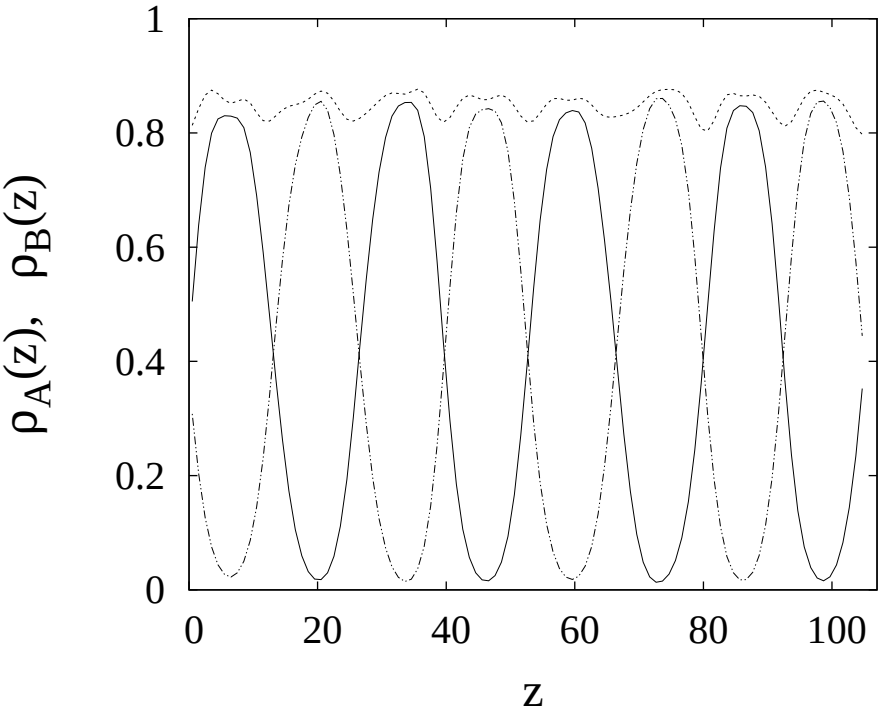

Figure 3.6: A- (solid line) and B-monomer (dashed line) number density profiles $\varrho_A(z)$ and $\varrho_B(z)$ along z in the lamellar phase with $\chi N = 25$ (weak segregation), chain length $N = 120$, the system geometry: $L_x = L_y = 71.27$ and $L_z = 4\lambda$. The dotted line presents the total monomer number density $\varrho_{tot}(z) = \varrho_A(z) + \varrho_A(z)$.

3.2 Finite Size Effects

It is worth to note that the finite size of the simulation box and the periodic boundary conditions reduce significantly the set of possible values of λ that the system can develope during the microphase separation. It is convenient to define the lamellar structure developed in the system through the numbers n_x, n_y , and n_z of intersections of isosurfaces with the x, y, z axes, respectively. Note that n_x, n_y , and n_z must have even values to keep the periodic boundary conditions: $n_x, n_y, n_z = 0, 2, 4, \ldots$. Given n_x, n_y , and n_z , the lamellar spacing can be calculated in the following way. Let us suppose that the first isosurface intersects the x, y, and z axes at points $(L/n_x, 0, 0)$, $(0, L/n_y, 0)$, $(0, 0, L/n_z)$ (it is assumed that the isosurfaces are ideal planes). The equation of the isosurface n_x, n_y, n_z is

$$n_x x + n_y y + n_z z = L \, .$$

Then, because of the periodic boundary conditions, the lamellar spacing is twice the distance between consecutive isosurfaces:

$$\lambda = \frac{2L}{\sqrt{n_x^2 + n_y^2 + n_z^2}} \, .$$

We visualized the isosurfaces in the simulations with the chain length $N = 120$ at various values of χ, each with 3 independent runs. Results are summarizied in Table 3.2. As seen,

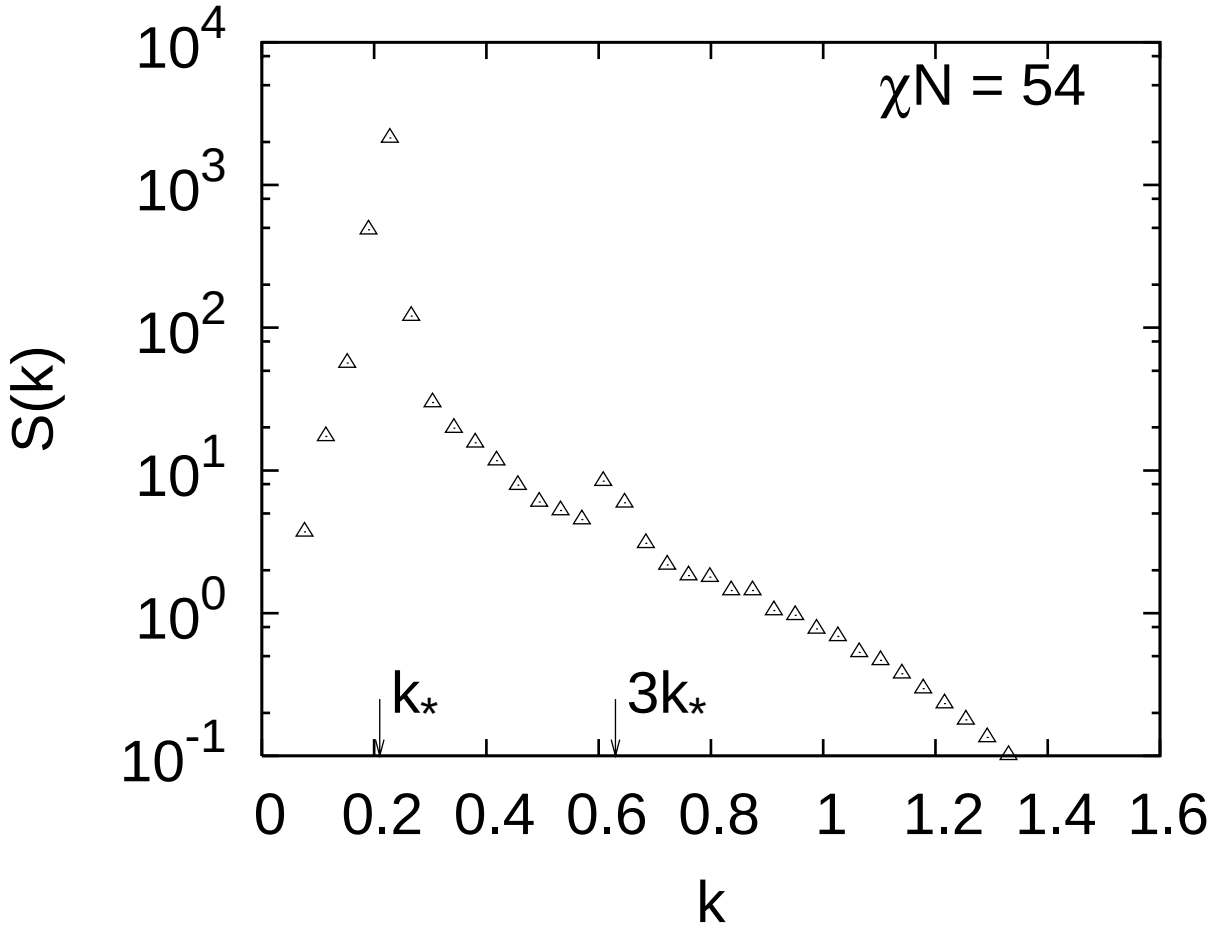

Figure 3.7: Spherically averaged structure factor in ordered phases. Lamellar phase with $\chi N = 54$, chain length $N = 120$ (strong segregation). The third order peak is present reflecting almost full segregation of A and B-components into well defined lamellae. Even order peaks are absent due to the arrangement of blocks inside the lamellar domains.

there are at least two domains with different orientations of the lamellae observed even deep in the strong segregation regime ($\chi = 1.25$). Note that n_x and n_y have odd values for the main domain in the third run of $\chi = 1.25$, which is due to the two-domain structure well developed in the system. Multidomain structures result in the fact that the position of the peak in the spherically averaged structure factor is not fixed by the set (n_x, n_y, n_z). In Fig. 3.11, we plot the lamellar spacing averaged over 3 independent runs (circles) versus χN obtained in simulations of the chains $N = 120$. The horizontal lines represent possible values of λ in a single domain structure as determined by the set (n_x, n_y, n_z). Generally, we do not find coincidence of the lamellar spacing from the simulation with the lines; some of the circles lie well between the corresponding lines (for example, the value of λ at $\chi N = 54.0$ is between $(4, 4, 0)$ and $(4, 2, 2)$), other are very close to lines but do not coincide with them, e.g. $\chi N = 90.0$ and the line $(4, 2, 0)$.

These observations suggest that the finite size effects of the simulation box have a little effect

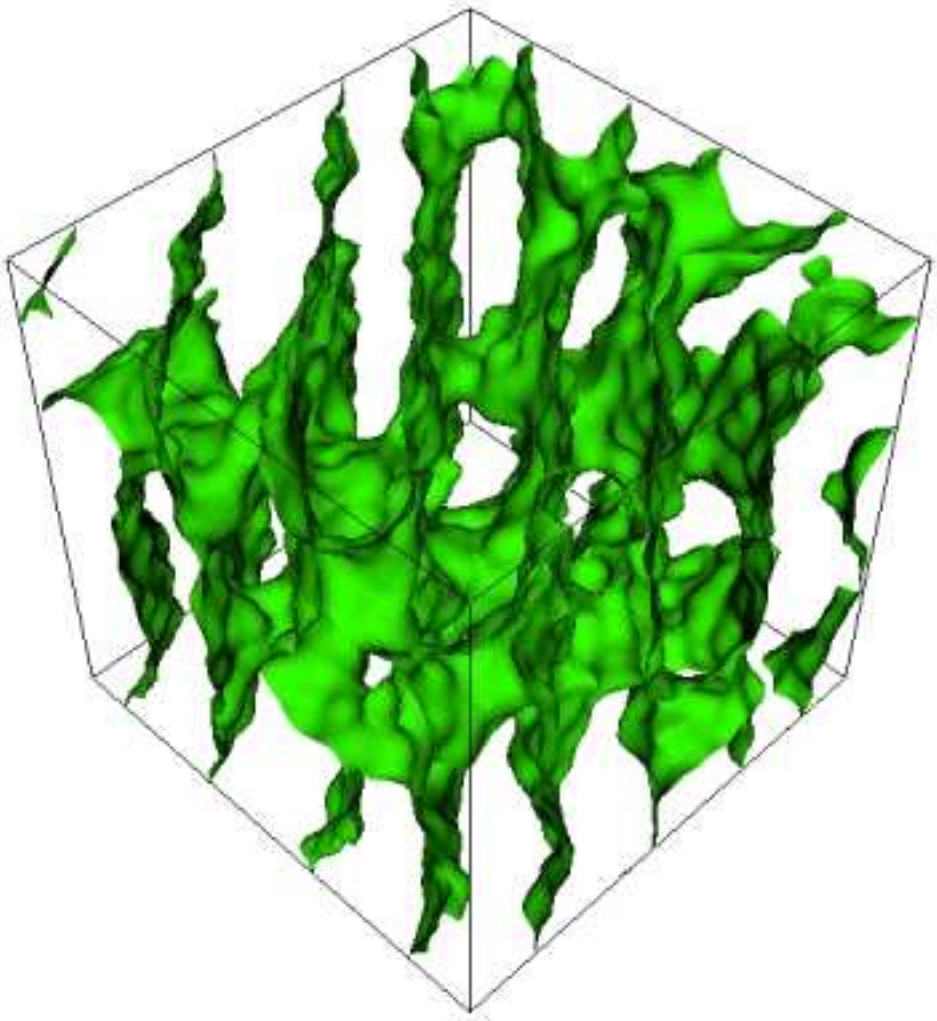

Figure 3.8: Isosurfaces of the lamellar structure for the same system as in Fig. 3.7 ($\chi N = 54$, strong segregation). Surfaces seen as connections between different planes are actually domains of lamellae with different orientations.

on the determination of λ and consequently on the scaling exponent n in $\lambda/N^{1/2} \sim (\chi N)^n$. Moreover, the multidomain structure observed in the system produces some averaging when calculating the structure factor, making the result more reliable.

A more general method to tackle the problem of the finite size and so to improve the value of n is to run simulations in simulation boxes of different geometries where the lamellae are oriented along the z axis. There are two possibilities for the box geometry: *i*) cubic one, where $L_x = L_y = L_z = L$ and the number of molecules varies with L to keep ρ_{tot} constant, and *ii*) rectangular one, where $L_z \neq L_x = L_y = L$ are varied whereas M, ρ_{tot} are kept constant. The free energy is then determined as a function of L (or L_z in the rectangular geometry) and the true lamellar spacing λ_F would correspond to the minimum of the free energy as a function of L (or L_z).

To run simulations from disordered initial conditions would be time consuming. In addition,

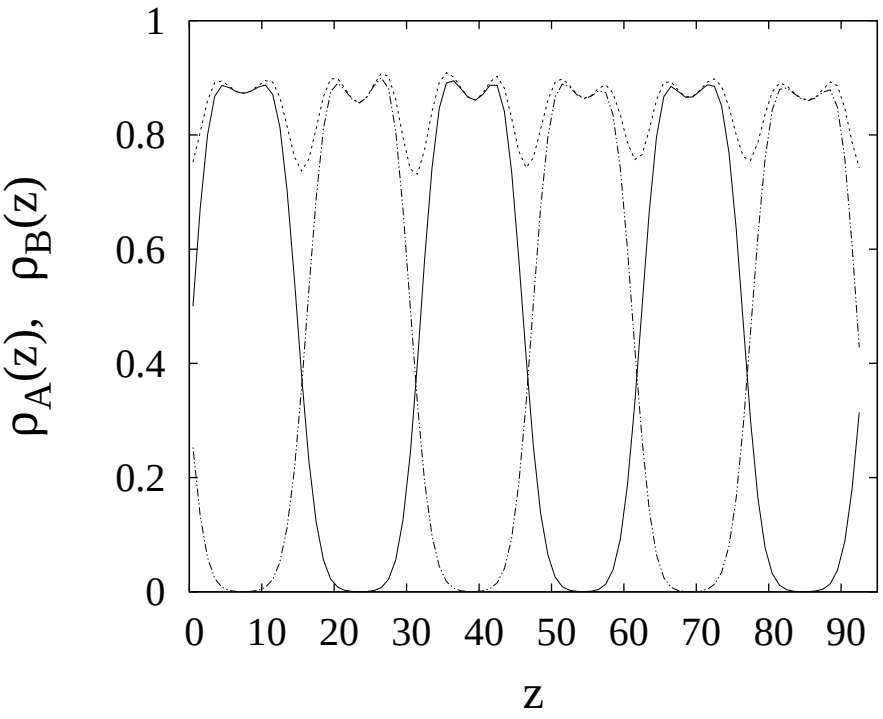

Figure 3.9: A- (solid line) and B-monomer (dashed line) number density profiles $\varrho_A(z)$ and $\varrho_B(z)$ in the lamellar phase with $\chi N = 54$ (strong segregation), chain length $N = 120$, the system geometry: $L_x = L_y = 77.92$ and $L_z = 3\lambda$. The dotted line presents the total monomer number density $\varrho_{tot}(z) = \varrho_A(z) + \varrho_A(z)$. Deep minima of $\varrho_{tot}(z)$ reflect the well pronounced isosurfaces between A and B-rich regions.

in the course of the simulations, the system may be trapped in a state where there exist two lamellar domains with the same lamellar spacing but different orientation of lamellae, which prevents us to extract the correct λ. To prevent this, we run simulations starting from an artificial configuration, where the molecules are already poritioned and oriented in the lamellar structure. To create such configurations, the system volume is divided into A- and B- rich regions with equidistant isosurfaces oriented perpedicular to the z axis. The initial values for R^A, R^B and r of each molecule are set equal to those of a molecule taken at random from the equilibrated final configuration of the previous simulations (with the same N and χ). For values N and χ not studied before, the values for R^A, R^B and r were calculated using the corresponding probability distributions, see Eqs. (2.20), (2.21). The molecules are distributed in the system in such a way that their centers of mass are located in some vicinity of an isosurface so that the x and y components of their center of mass are randomly drawn in the interval $(0, L)$ and the z components obeys $Z_i - 0.1r < z < Z_i + 0.1r$ where Z_i is the position of the i-th isosurface along the z axis. The molecules are always oriented in the z direction; the A-block of each molecule is placed in the A-rich region on one side of the isosurface and the B-block of the molecule is in the B-rich region on the other side of the isosurface.

Simulations have shown that the systems with the artificial initial configurations rapidly evolve towards equilibrium so that the free energy per molecule computed with the help of (2.2)

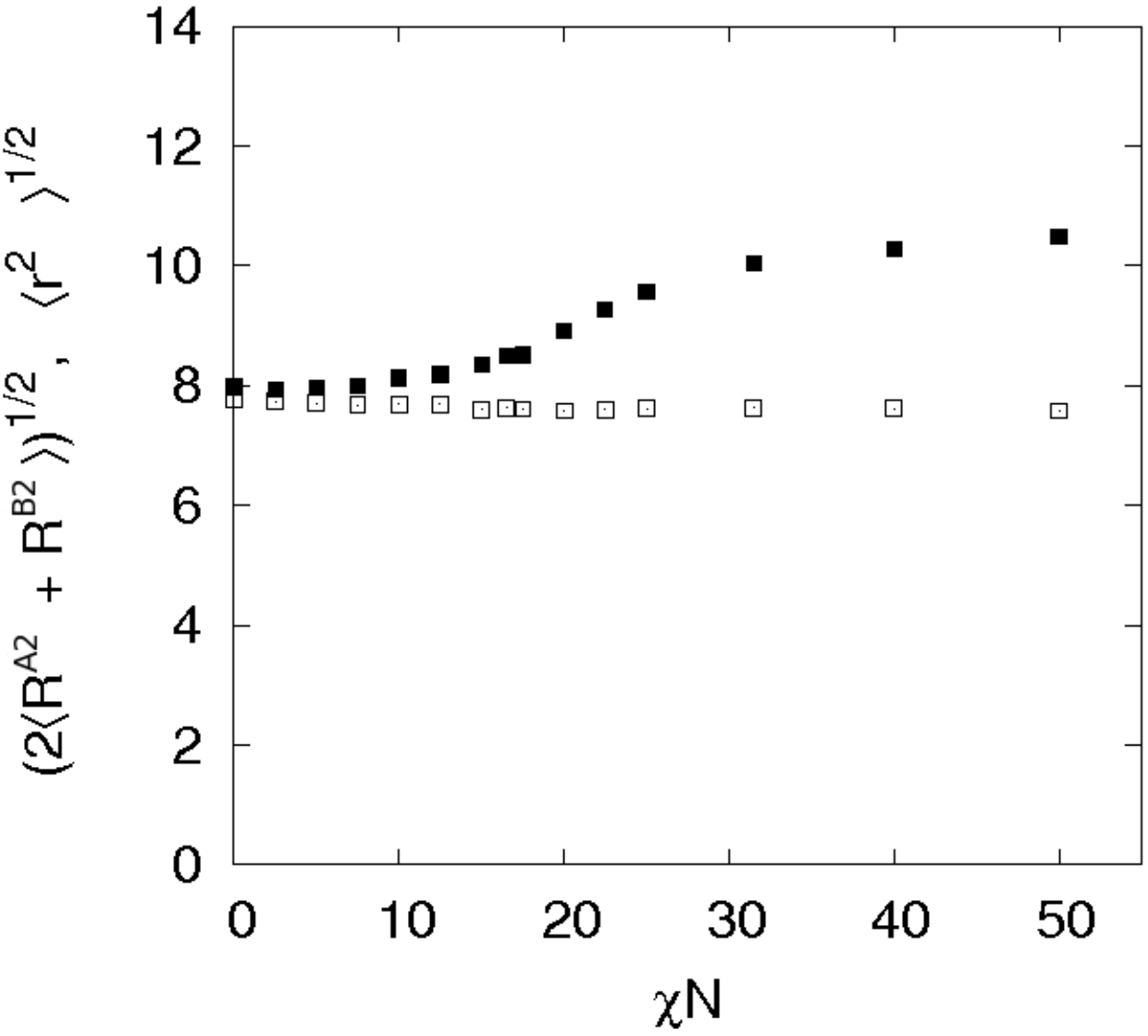

Figure 3.10: Average stretching parameter r (full symbols) compared to the average radii of gyration $\langle (R^A)^2 \rangle^{1/2} = \langle (R^B)^2 \rangle^{1/2}$ (light symbols), cf. Eq. (2.21) versus χN, in the system with the chain length $N = 120$.

with (2.15), (2.16) reaches a plateau after about $200 - 300$ MCS and fluctuates about its mean value. The profiles of the total monomer number density and A-, B- monomer number densities do not show any significant changes after about 200 MCS. We let the systems equilibrate typically during the first 1000 MCS and then calculated the mean free energy during the following 4000 MCS. We have found no difference in the mean free energy in simulations with the cubic and rectangular geometries. In the following we will use the rectangular geometry of the simulation box with 4000 or 6000 molecules, because reducing the particle number in the cubic geometry leads to larger fluctuations of the free energy.

We also compared simulations with the artificial initial configurations discribed above with

χN	**run**	(n_x, n_y, n_z)	**remarks**
0.45	1	$(4, 4, 0)$	dominant domain, connections between lamellae
	2	$(4, 4, 0)$	dominant domain, small additional domain
	3	?	several domains
0.75	1	$(4, 4, 2)$	dominant domain, small additional domains
	2	?	several domains
	3	$(4, 4, 2)$	dominant domain, small additional domains
0.95	1	$(4, 2, 0)$	dominant domain, small additional domains
	2	$(4, 2, 0)$	dominant domain, small additional domains
	3	?	several domains
1.25	1	$(4, 2, 0)$	two domains
	2	$(4, 2, 0)$ and $(4, 0, 0)$	two domains
	3	$(3, 3, 0)$	two domains

Table 3.2: Structures observed in simulations with the chain lenth $N = 120$ at different values of χ; n_x, n_y, n_z are always ordered in the way that $n_x \geq n_y \geq n_z$. We give values of n_x, n_y, n_z only for the most pronounced domain developed in the system. The question mark is placed in cases where it was hard to decide what orientation the domains had .

simulations where the initial configurations correspond to a disordered melt but a potential was applied forcing the molecules to have the orientation parallel to the z axis, similar to anisotropic spin models in ferromagnetism. After about 10000 MCS, lamellae oriented perpendicular to the z axis were well developed in the system and the mean free energy was calculated during the next 4000 MCS. There was again no difference in the free energy in simulations with both types of the initial configurations so that we decided to use the simulations with the artificial initial configurations because they take less time for equilibration.

We show in Fig. 3.12 the typical behavior of the free energy when changing the dimension of the system along z. The systems contains 6000 molecules with $N_A = N_B = 60$ at $\chi = 0.45$ and the system dimension along z is $L_z = 3\gamma\lambda$. The parameter γ reflects the deviation of the lamellar spacing in the system from λ calculated previously with the structure factor. For convenience we represent the free energy as a function of γ . The free energy has a minimum at $\gamma \simeq 0.9$. To obtain a more exact value of γ, the free energy as a function of γ was approximated by a third order polynomial in the vicinity of its minimum. It should be noted that the values of the lamellar spacing $\lambda_F = \gamma\lambda$ which minimize the free energy are always lower by about 10% from the values estimated through the peak position of the structure factor for all chain lengths and the interaction χ.

3.3 Scaling of the Lamellar Spacing

Based on the minimization of the free energy described above, we study now the variation of the periodic spacing λ with the chain length and the interaction strength for the lamellar morphology in melts of symmetric chains. It is predicted by the strong segregation theories [Oht86] that λ scales with N and χ as $\lambda/N^{1/2} \sim (\chi N)^n$ with $n = 1/6$, see Eq. (1.46). This relation can be obtained by minimizing the sum of the elastic energy due to molecular stretching

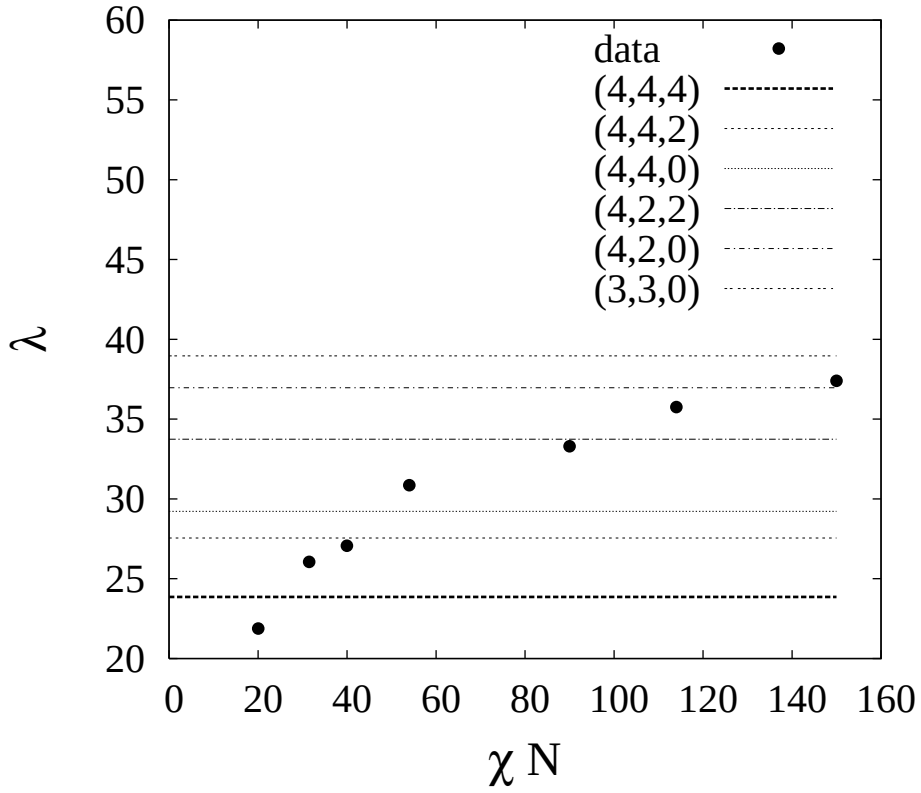

Figure 3.11: Lamellar spacing from the simulations averaged over 3 independent runs (circles) and its possible values as determined by the set (n_x, n_y, n_z) (lines) in the system with the chain length $N = 120$.

within the period λ and the interfacial energy, see page **11**. To test this scaling law, we run simulations with minimization of the free energy in the systems with $N = 62, 120, 210, 300$ and at $\chi = 0.45, 0.95$. The scaling law is obviously confirmed in Fig. 3.13, where we plot $\lambda/N^{1/2}$ versus χN. We find a good collapse of the data yielding the scaling exponent to have a value $n = 0.22$ which is somewhat higher than the theoretical prediction 1/6. When the interaction strength becomes smaller, near the ODT and in the disordered melt, the Gaussian behavior of the chains gets recovered, reflected by scaling of the characteristic length of the A-monomer density fluctuations with $N^{0.5}$, see data points for the chain length $N = 120$ below $\chi N \approx 12$ in Fig. 3.13.

3.4 Coarsening

Contrary to spinodal decomposition in the blend of two polymers A and B where the demixing length diverges with time in the limit $t \to \infty$, the chemical linkage between two block of the diblock copolymer causes microphase separation in the melt of symmetric diblock copolymers below the ODT with the demixing length approaching the lamellar period λ. We study this type of coarsening, bounded at long times, in a melt of diblock copolymers with $N_A = N_B =$

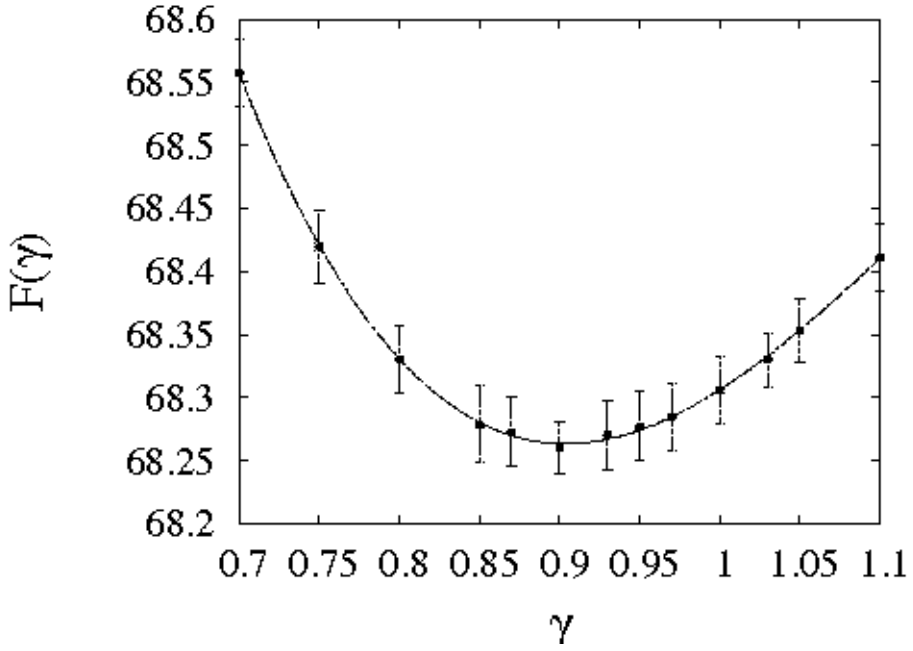

Figure 3.12: Approximation of the free energy in the vicinity of its minimum by a third order polynomial. The system has a rectangular geometry with $L_z = 3\gamma\lambda$ and contains 6000 molecules with $N_A = N_B = 60$ at $\chi = 0.45$. The bars represent the relative error of the calculated free energy.

60, starting from an initial state corresponding to the infinite temperature where the radii of gyration of the blocks for each molecule and the distance between them are distributed according to the probabilities for R^X, $\vec{r}$, see (2.20), (2.21). Then the mismatch parameter χ is set to $\chi = 0.45$ at the initial time $t = 0$ and the system is let to equilibrate. Three independent runs are made, differing in random initial distributions of the molecular positions within the simulation box.

The results for the spherically averaged structure factor of the A-component are presented in Fig. 3.14. A broad peak in the structure factor already developes at early times, which is associated with the characteristic length of A-monomer density fluctuations present even if there is no mismatch between A and B monomers. This length is of the order of the mean gyration radius of A blocks. As the time proceeds, A-rich domains begin to grow and the peak shifts to smaller k. At the same time the height of the peak becomes larger reflecting an increase in the amplitude of the density fluctuations.

To quantify the coarsening process further, we consider the position of the peak as estimated through the Lorenz fit $f(k) = B/(1 + (k^* - k)^2/a)$, where a, B, and k^* are fitting parameter. k^* starts with the value about 0.4 at $t = 40$ MCS, see Fig. 3.15 and equals the inverse of the lamellar spacing $k^* = 2\pi/\lambda$ at the end of the simulation. For early times up to 4000 MCS, k^* decreases with time as $k^* \sim t^{-0.15}$. An exponent of the similar order of magnitude was found in the work of Oono and Bahiana [Oon90], based on numerical solving a Cahn-Hilliard type equation for diblock copolymer melts. Oono predicted a faster growth of the characteristic length with the exponent 1/4 which is probably due to the hydrodynamic effects included in

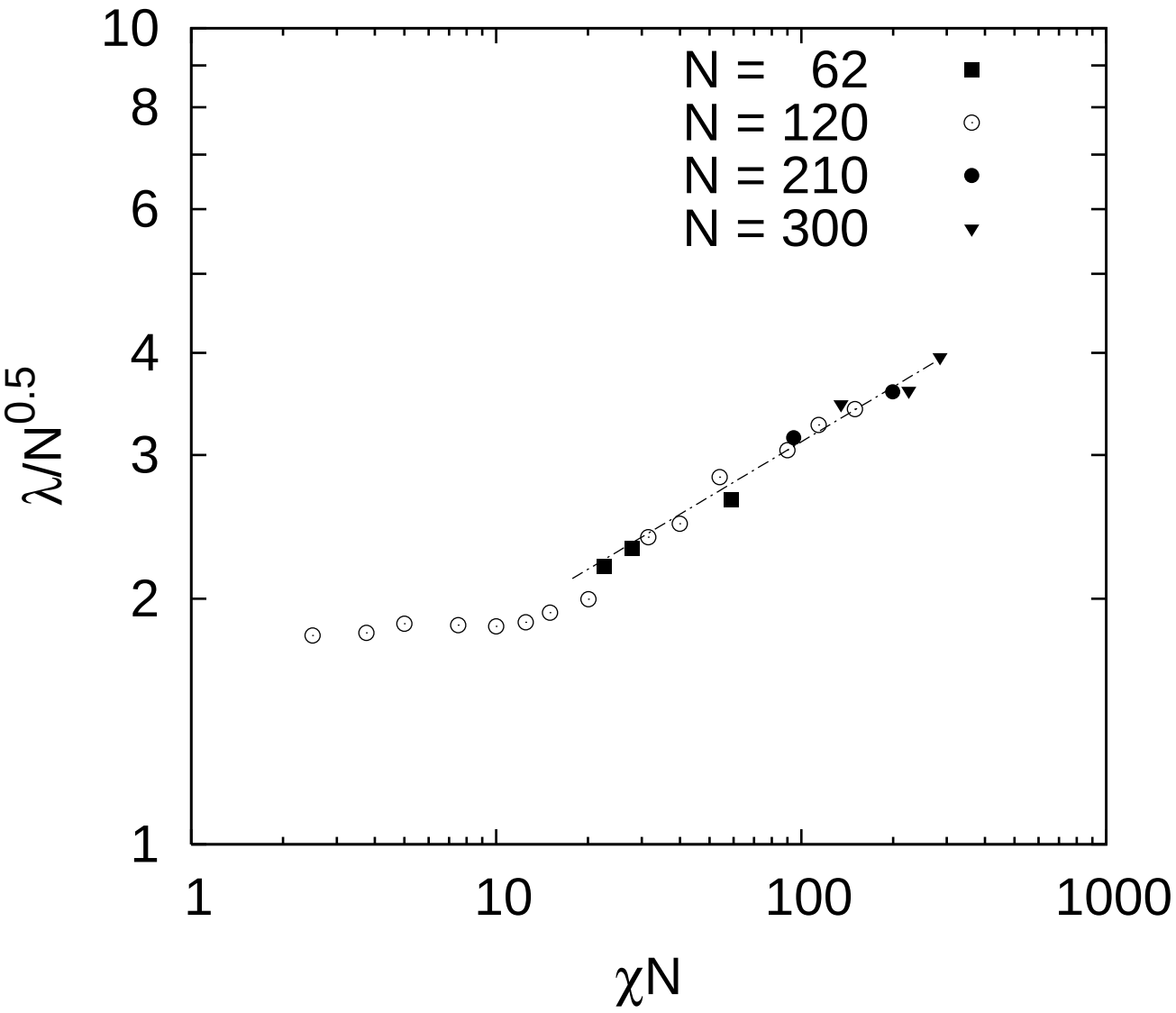

Figure 3.13: Scaling plot of lamellar distance λ depending on χ and N for four chain lengths $62, 120, 210, 300$ in the strong segregation-regime. The dashed straight line has a slope $n \simeq 0.22$. Data points for $N = 120$ are continued to lower χN-values to regain the weak–segragation behavior $\lambda \sim N^{0.5}$. All data were obtained in simulations with minimization of the free energy (2.2) with (2.15), (2.16).

their model.

3.5 Asymmetric Chains

We also carried out bulk simulations for asymmetric chains with the length $N = 100$ and the A-monomer fraction $f_A = 0.3$. The existence of a cylindrical phase is exemplified by

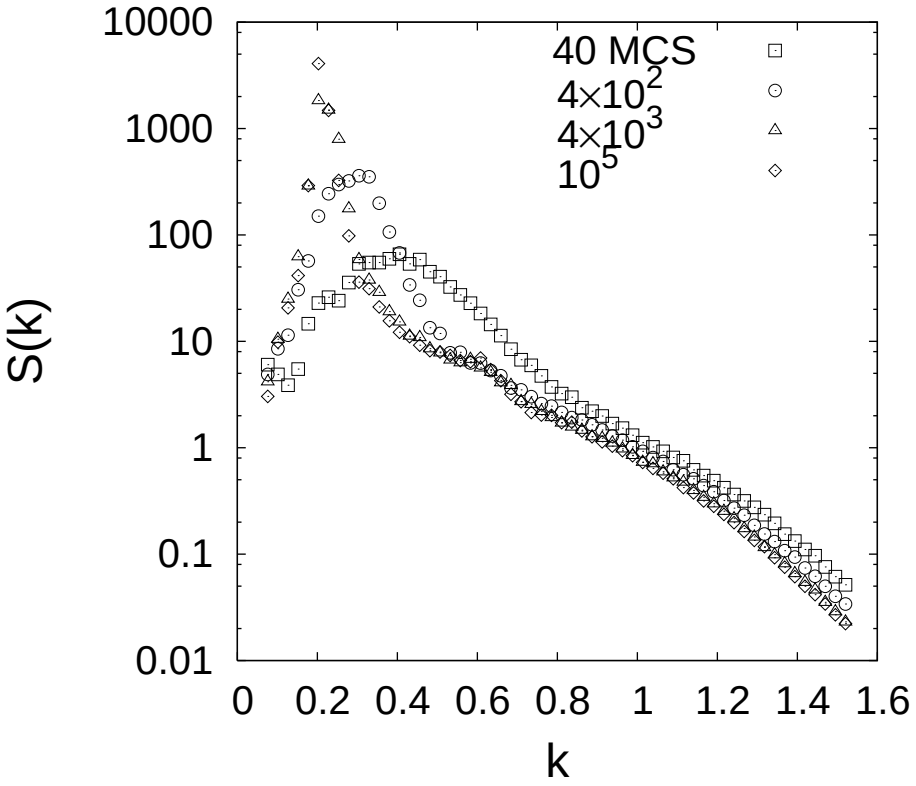

Figure 3.14: The structure factor developing in time in the melt of symmetric chains with the length $N = 120$. The initial configuration was a disordered melt at the infinite temperature $\chi = 0$. At $t = 0$ the mismatch parameter χ was set to 0.45. Note that the structure factor has a peak even at $t = 0$ corresponding to the mean radius of gyration of A blocks.

Fig. 3.16 where superstructure peaks of the spherically averaged structure factor of the minority component characteristic for this structure are clearly seen. To obtain Fig. 3.16, we used $\chi N = 65.0$. In Fig. 3.17 we plot the isosurfaces for this structure. One can clearly observe the columnar tubes of the minority component A ordered on a hexagonal $2 - d$ lattice. Some connections between neighboring tubes seen in the figure are actually additional domains of cylindrical structure with their orientations different from that of the main domain. The whole multidomain structure remains stable when the simulation going further on which may be attributed to the absence of hydrodynamic flows in the Monte Carlo algorithm.

In Fig. 3.18 we present isosurfaces obtained in simulations on asymmetric chains $f_A = 0.17$ (chain length $N = 150$) at $\chi N = 45.0$. The minority component is contained in spheres or bulbs ordered in a body–centered cubic (bcc) lattice. There are still some A-blocks in the B-rich region which do not disappear as the simulation goes on.

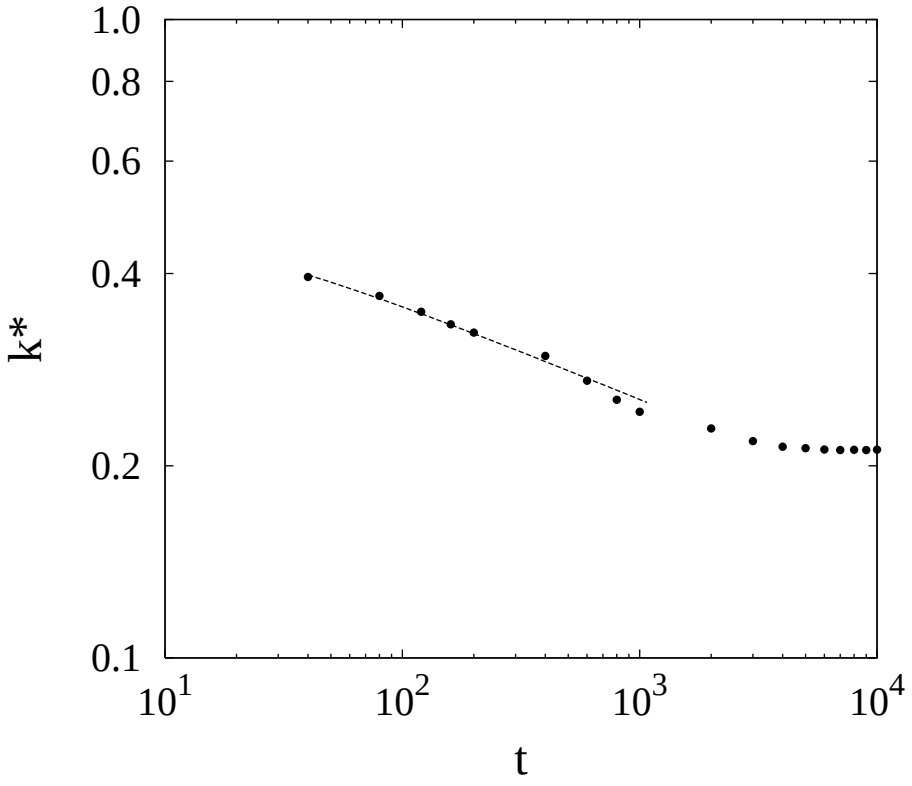

Figure 3.15: The position of the peak of the structure factor as estimated with the Lorenz fit versus time in the melt of symmetric chains $N = 120$ after suddenly increasing χ from zero to 0.45. The line represents a power law fit with the exponent 0.15 to the data at the initial times.

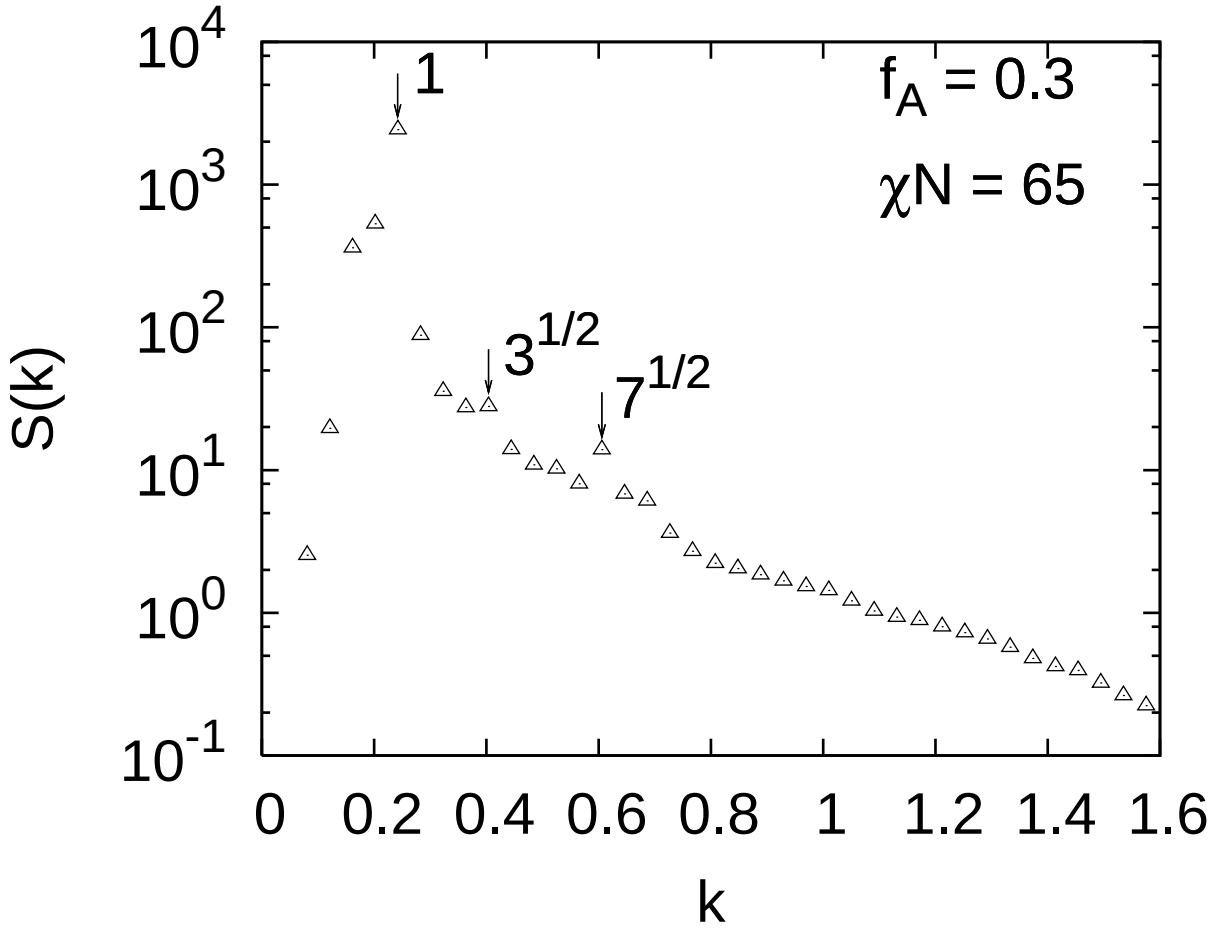

Figure 3.16: Spherically averaged structure factor for the cylindrical phase in the system $f_A = 0.3$, $\chi N = 65$ and the chain length $N = 100$. The positions of the main peak k_1 and two higher order peaks k_2 and k_3 are marked with 1, $3^{1/2}$ and $7^{1/2}$ respectively with their relative positions $k_2/k_1 = 3^{1/2}$ and $k_3/k_1 = 7^{1/2}$.

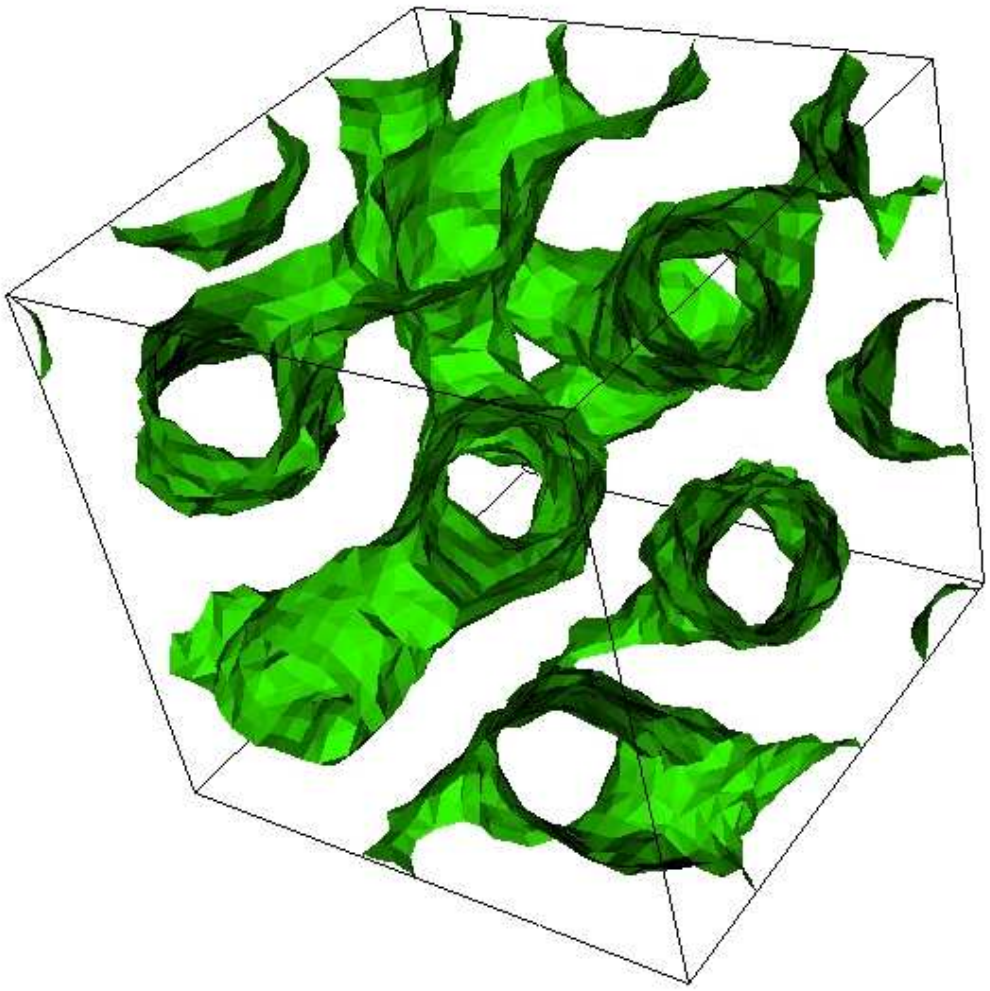

Figure 3.17: Isosurfaces of the cylindrical phase in the system as in Fig. 3.16. The columnar tubes of the minority component are ordered on a two-dimensional hexagonal lattice. Connections between tubes are in fact additional domains of cylindrical structrure with different orientations.

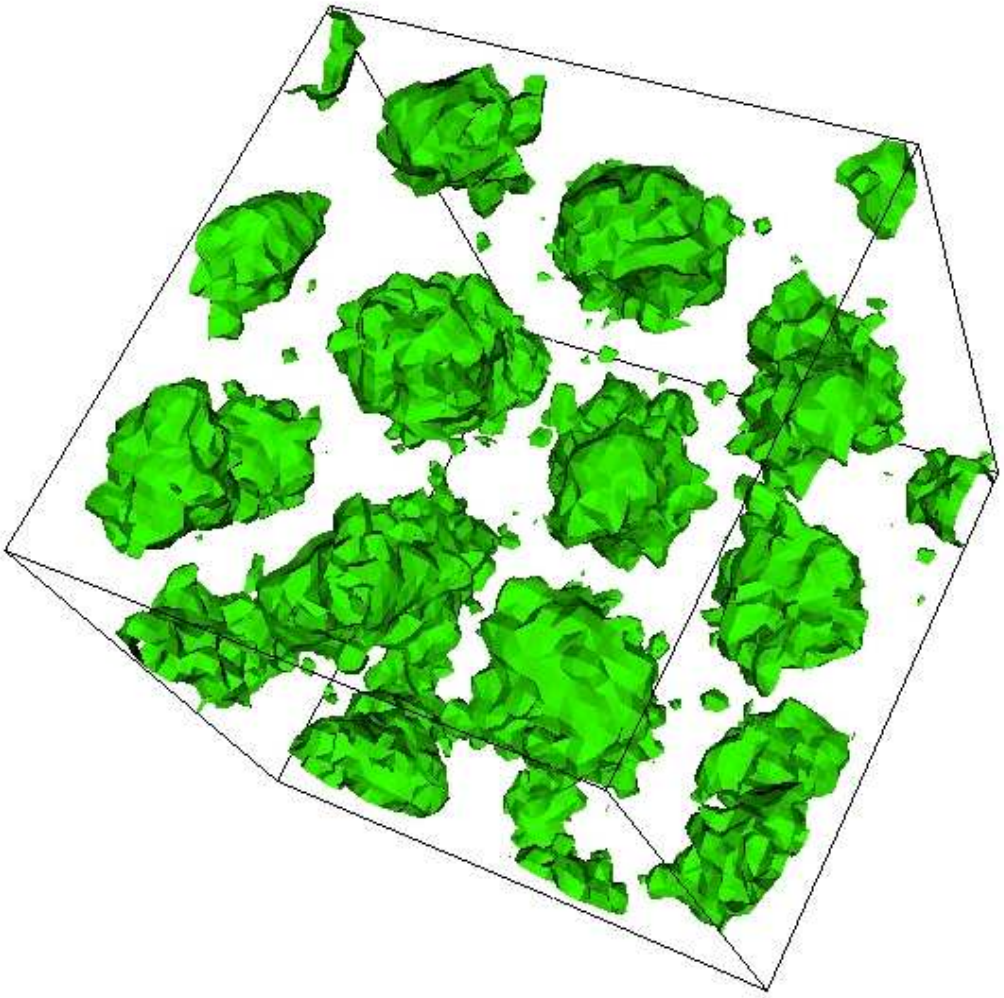

Figure 3.18: Isosurfaces of the bcc phase in the system of asymmetric chains $f_A = 0.17$ at $\chi N = 45.0$ (chain length $N = 150$). The minority component is contained in spheres ordered in a bcc lattice.

4 Dynamic Properties in the Bulk

Now we discuss how the self-diffusion of diblock copolymers is influenced by concentration fluctuations when approaching the ODT from the disordered phase. Another issue is the effect of the ordered structures on the diffusion. As the GDM does not catch molecular features on the length scale less than the gyration radius of the block, we do not intend to study the diblock copolymer dynamics on the length scales less than the gyration radius of the molecule R_G and the time scale less than the disentanglement time τ_D , see section 1.

For all systems the time dependent directionally averaged diffusion coefficient is defined from the mean square displacement of the center of mass of the molecule

$$D(t) = \frac{1}{3}\frac{\left\langle [\vec{r}_{cm}(t) - \vec{r}_{cm}(0)]^2 \right\rangle}{6t}\,, \tag{4.1}$$

where $\langle ... \rangle$ means average over all molecules and different initial conditions of the system.

4.1 Diffusion in the Lamellar Phase

We will be mostly interested in systems with $N_A = N_B = 60$ for which the ODT is expected to occur at $\chi \sim 15.0 - 16.5$, section 3.1 of section 3 The mean square displacement $\left\langle [\vec{r}_{cm}(t) - \vec{r}_{cm}(0)]^2 \right\rangle$ shows usual diffusive behavior for times $t > \tau_D$ for various values of χ , see Fig. 4.1. The entanglement time τ_D can roughly be estimated as an average time which the molecule needs to diffuse over the radius of gyration of one block R^X , which is close to 3.8 for the given chain length.

Close examination of Fig. 4.1 reveals that τ_D is of the order 50 MCS and is almost unaffected by the interaction χ , e.g. by the ordering. The short time diffusion coefficient defined as $D_0 = \lim_{t\to 0} D(t)$ remains constant for all χ , and so is fully determined by $D_0(\chi = 0)$. We also find by inspection that for all χ the diffusivity $D(t)$ reaches a constant values which are denoted in the following as D .

To study the effect of the lamellar ordering on the diffusion in more details, lamellae oriented perpendicular to the z axis were prepared through placing molecules parallel to the z and with their centers of mass located at the isosurfaces, for details see section 3.2. The system dimension L_z was set to an integer number of the lamellar spacing calculated from the structure factor, see section 3.1 and the lateral dimensions L_x and L_y were taken from $L_x = L_y = \sqrt{NM/(L_z\rho_{tot})}$, where the number of molecules in the system is $M = 4000$. The systems were then let to equilibrate after which the diffusion coefficients $D_{||}(t)$, $D_z(t)$ were calculated that correspond to the motion in the lateral direction along the lamellae

$$D_{\|}(t) = \frac{1}{2}\frac{\left\langle \left[\vec{r}_{cm,||}(t) - \vec{r}_{cm,||}(0)\right]^2 \right\rangle}{6t}\,,$$

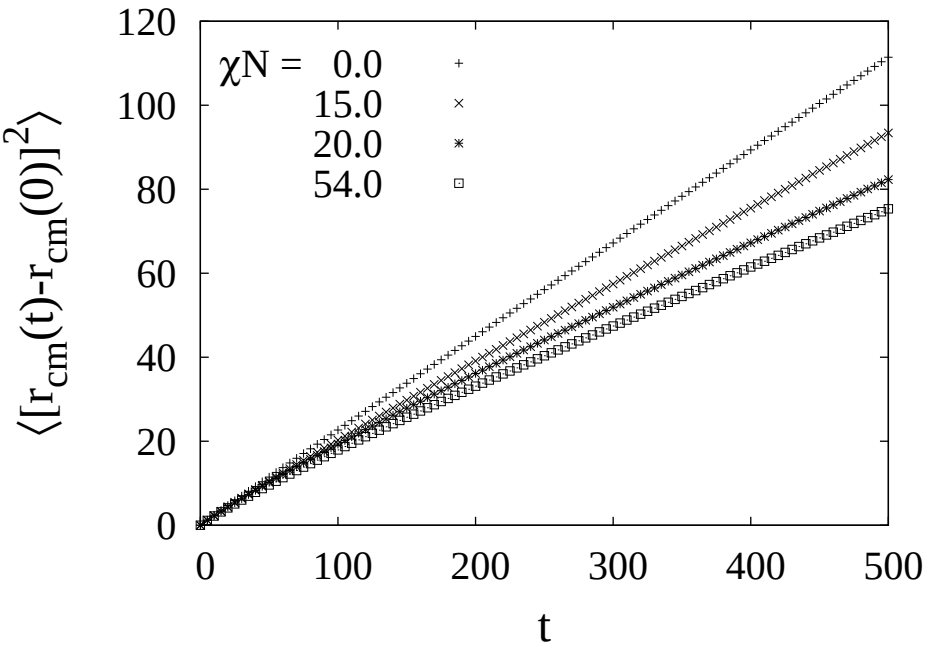

Figure 4.1: Mean square displacement of the center of mass of the molecule in disordered and ordered lamellar phases of symmetric chain with $N_A = N_B = 60$ at various χ.

and to the motion across the lamellae

$$D_{\perp}(t) = \frac{\left\langle [z(t) - z(0)]^2 \right\rangle}{6t},$$

where $\vec{r}_{cm,||} = (x, y)$. The quantity $\left\langle \left[\vec{r}_{cm,||}(t) - \vec{r}_{cm,||}(0)\right]^2 \right\rangle$ is plotted in Fig. 4.2; it shows no suppression of the lateral diffusion, instead a slight increase in the lateral motion of the molecules is observed with increasing χ, which may be attributed to the reduction of the structural fluctuations and so to an decrease of the $A - B$ interface thickness leading to more free motion of the molecules along the isosurfaces. The overall weak dependence of the mean-square displacement on χ agrees with the prediction of Barrat and Fredrickson [Bar91] that in a system of Rouse chains the diffusion of the molecules along lamellae is not affected by the parameter χ.

Contrary to the lateral behavior, the diffusion of the center of mass of the molecules in the direction perpendicular to the lamellar layers is suppresed when increasing the interaction χ, see Fig. 4.3. For $\chi \geq 30.0$, the quantity $\left\langle [z(t) - z(0)]^2 \right\rangle$ practically saturates at a constant value, meaning that the centers of mass of the molecules are almost attached to the isosurfaces with single jumps from one isosurface to a neighbouring one.

All the measured diffusion constants normalized by $D(\chi = 0)$ are summarized in Fig. 4.4. We find a continuous drop in the isotropic diffusion coefficient D starting already in the disordered melt. That means that the A and $B-$blocks of the molecule prefer to stay in A and B-rich regions already forming in the disordered phase. Near the ODT, the quantity D is about 80% of its value at $\chi = 0$ which is higher than the theoretical prediction of about 60% by Barrat and

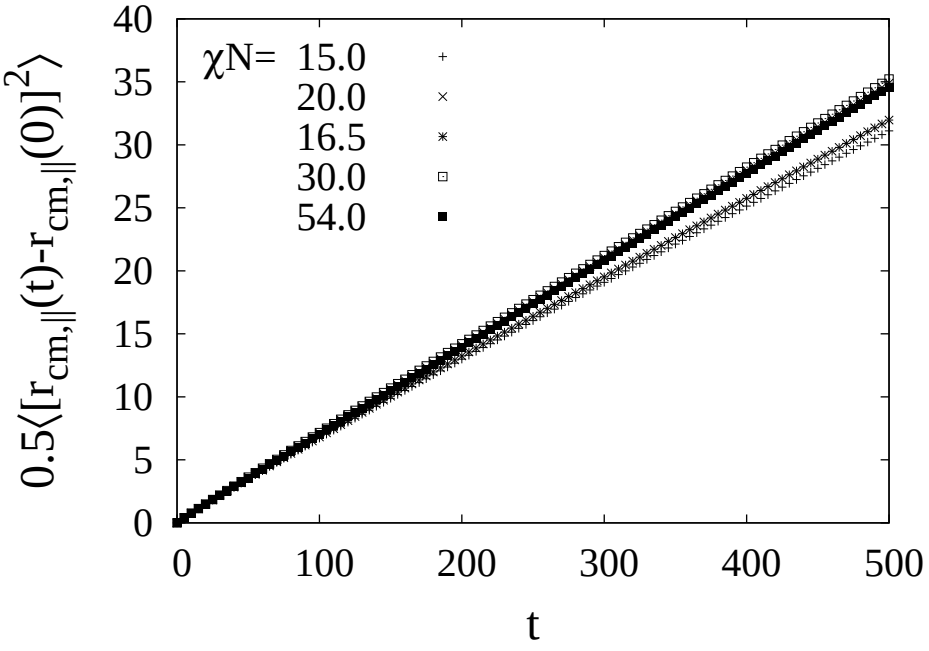

Figure 4.2: Lateral mean square displacement of the center of mass of the molecules in the ordered phase of symmetric chain with $N_A = N_B = 60$ at various χ.

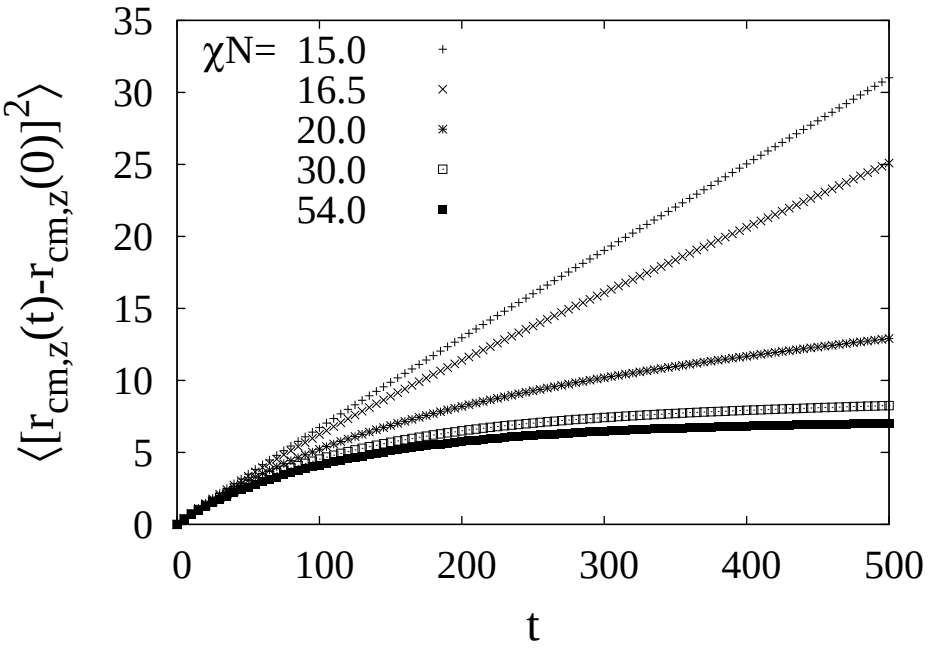

Figure 4.3: Perpendicular mean squared displacement of the center of mass of the molecules in the ordered phase of symmetric chain with $N_A = N_B = 60$ at various χ.

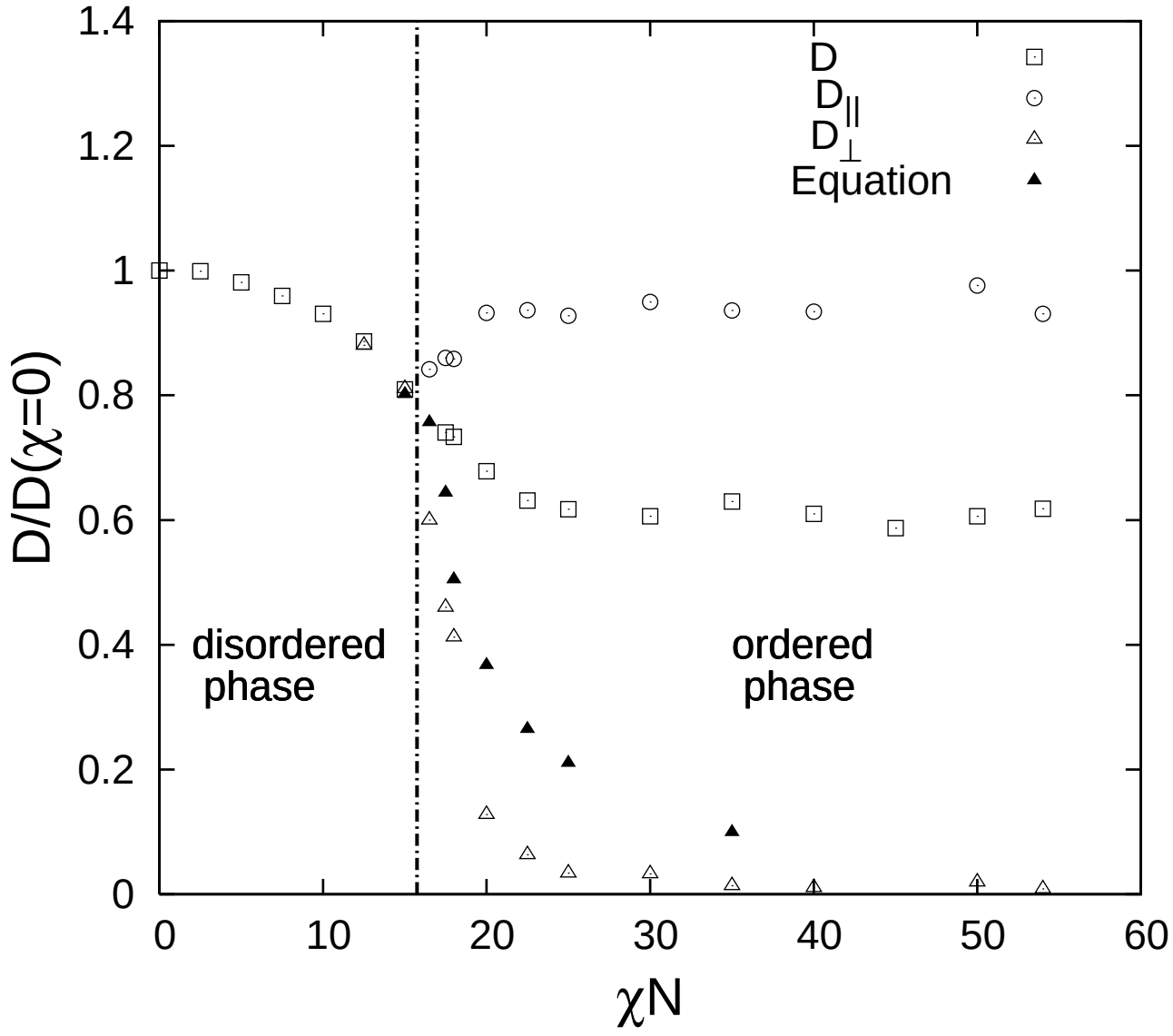

Figure 4.4: Normalized diffusion coefficient D as well as anisotropic diffusion coefficients $D_{\|}, D_{\perp}$ in the lamellar phase versus χN in the system of symmetric chains with $N = 120$. The vertical dashed dotted line separates isotropic from anisotropic diffusion. Black triangles correspond to diffusion coefficient calculated within the mean field approach, see Eq. (4.2).

Fredrickson [Bar91] supported by simulation results of Blumen [Hof97a] and Kremer [Mur99] who observed a drop of about 40% in the isotropic diffusion near the ODT. D is consistent with the average $D \approx (2D_{\|} + D_{\perp})/3 \approx (2/3)D_{\|}$ in the lamellar phase. It continues to decrease further and at $\chi \simeq 25.0$ saturates reaching about 60% of its value at $\chi = 0$ characteristic of two-dimensional diffusion, see Fig. 4.4.

4.2 Mean Field Approach

An intuitive approach to understand the diffusion across the domain boundaries in the lamellar phase is to adopt the picture of one-dimensional Brownian motion in a periodic potential $V(z)$. We start from the exact expression, see [Die77] and Appendix D, $D = D_0/\left[\overline{e^{-\beta V(z)}}\,\overline{e^{\beta V(z)}}\right]$, where D_0 is the diffusion coefficient in the corresponding homogeneous state, and the bars denote averages over one period of $V(z)$.

Obviously, the rates determining diffusion steps are those near the maximum of $V(z)$ or the minimum of the equilibrium density $\varrho_{eq}(z) \propto \exp(-\beta V(z))$. Within mean field theories [Die86] this aspect can be generalized to interacting systems by regarding $V(z)$ as potential of mean force, defined in terms of the actual equilibrium density via the Boltzmann factor, Appendix D. Guided by these ideas, we write for our system

$$D_\perp \simeq \frac{D_0}{\left[\overline{\varrho_A(z)}\,\overline{\varrho_A^{-1}(z)}\right]} \tag{4.2}$$

with simulated A-monomer densities $\varrho_A(z)$ and diffusion constant D_0 at the ordering transition point. Close to the ordering transition $\varrho_A(z)$ can be represented as $\varrho_A(z) \simeq \overline{\varrho_A}(1+\Delta\varrho_A \sin k_\star z)$, see section 3.1 of the section 3, which yields $D_\perp = D_0(1-\Delta\rho_A^2)^{1/2}$. This simple approach already describes the sharp drop in $D_\perp$ for $\chi N > (\chi N)_c$, shown in Fig. 4.4. It still overestimates the simulated data for $D_\perp$ especially at larger χN. One reason may lie in the fact that shape deformations of molecules during barrier crossing are not included in these arguments.

We run additional simulations with longer chains ($N_A = N_B = 150$). It should be noted here that the Rouse dynamics which is valid for unentangled chains cannot be verified because the maximal translational change $\triangle\vec{r}_{max}$ of one block is $K_r = 0.75$, i.e. a fixed fraction of the gyration radius of the block $R^X \sim N^{1/2}$ so that the time units in the Monte Carlo procedure would be different for different chain lengths. In Fig. 4.5 the diffusion coefficients $D(\chi, N)$ for the chains of lengths $N = 120$ and $N = 300$ normalized with respect to $D(\chi = 0, N)$ are plotted as functions of the product χN . The curves belonging to different N scales remarkably well with χN in the disordered melt. However, wenn approaching the ODT, the values of the diffusion constant for the shorter chain are higher than those for the longer chains because $(\chi N)_c$ increases with decreasing the chain length. Diffusion of the diblock copolymers of different lengths was also studied in simulation work of Hoffmann [Hof97a], where the best scaling was achieved for the scaling variable $(\chi N)^{0.7}$.

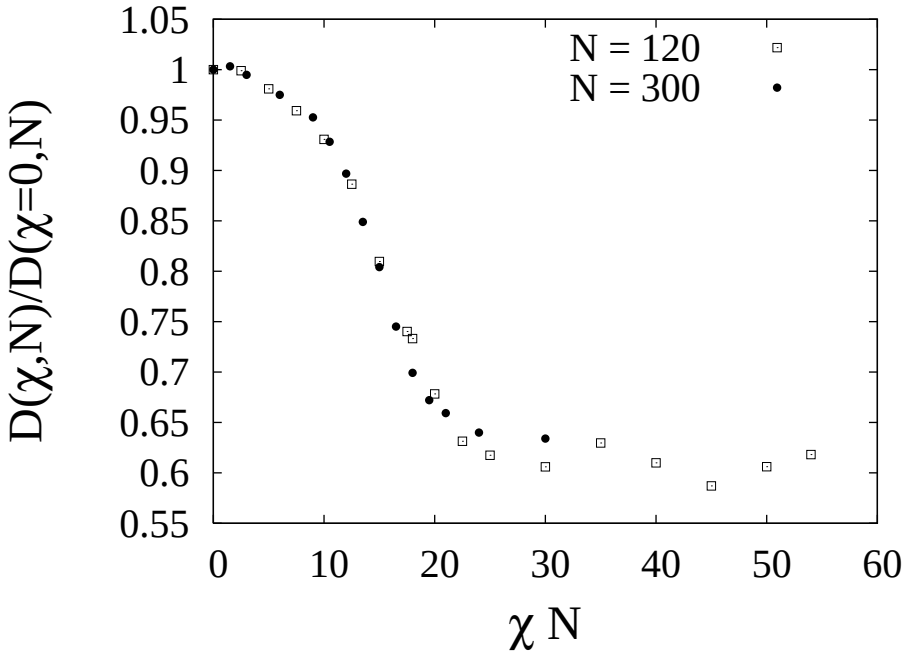

Figure 4.5: Normalized diffusion coefficient D for chains of length $N = 120$ and $N = 300$ in the disordered melt and lamellar phase versus χN. Fair scaling is observed up to the ODT where it breaks down due to the dependence of $(\chi N)_c$ on N, see section 3.1.

5 Confined Geometries

In this section, we present results of Monte-Carlo simulations of the symmetric diblock copolymer melt confined between two parallel flat walls. Confinement of diblock copolymers adds several new aspects to microphase separation studied in the section 3. A common repulsion of A and B-blocks by neutral walls will favor parallel orientation of molecules to the wall surface and therefore can induce perpendicular lamellar ordering. However, if walls act differently on A and B-monomers, one type of blocks will be preferred to the wall, favoring parallel lamellar ordering.

It has been shown experimentally [Kel96] that perpendicular lamellae turn out to imply only short range order in the case of neutral walls. Long-range order can be achieved by casting symmetric diblock copolymers on heterogeneous substrates patterned with stripes of the width $\lambda/2$ that alternately prefer A and B-blocks of the molecule, [Roc99] and [Sto03]. We show that the GDM can provide new insight into the process of the pattern translation. Calculations of the time-dependent structure factor enable us to discuss the propagation of the stripe patterns from the wall into the film and their competition with spontaneous ordering fluctuations occuring away from the pre-patterned substrate.

5.1 Neutral Walls

In this subsection we study equilibrium properties of symmetric diblock copolymer thin films confined between two flat parallel homogeneous surfaces at $z = 0$ and $z = L_z$ which have no preferential interaction for A- or B-monomers. Confinement in thin films with neutral walls is modeled by a soft repulsive potential of the form

$$V_w(z) = \hat{\epsilon}_w \left[\exp\left(-\frac{z}{2\, l_w} \right) + \exp\left(-\frac{L_z - z}{2\, l_w} \right) \right] , \tag{5.1}$$

which acts in the same way on A- and B-monomers located at z. Here $\hat{\epsilon}_w$ characterizes the strength of the wall-monomer interaction and the parameter l_w controls the hardness of the wall; the film thickness is defined by L_z. The molecules are free to move in the x and y directions where periodic boundary conditions are imposed. In the following we set $\hat{\epsilon}_w = 1$ and $l_w = 0.5$ so that $2l_w$ is equal to the average bond length of the Gaussian chain.

The presence of the walls leads to an additional term F_{wall} in the free energy functional (2.2)

$$F = F_{\text{intra}} + F_{\text{inter}} + F_{\text{wall}} , \tag{5.2}$$

where

$$F_{\text{wall}} = \sum_{i=1}^{M} F_{\text{wall}}^{(i)} = \sum_{i=1}^{M} \sum_{X=A,B} \int d^3y \; \tilde{\varrho}_i^X(\vec{y}) \; V_w(z) . \tag{5.3}$$

The exponential form Eq. 5.1 of the wall potential has the advantage that the terms determining the interaction of the molecules with the walls in (5.3) can easily be calculated analytically.

Throughout this section the simulations were carried out for symmetric diblock copolymers consisting of $N_A = 60$ monomers of type A and $N_B = 60$ monomers of type B whose bulk properties were studied in previuos sections 3 and 4. The mismatch interaction χ_{AB} was chosen to be 0.45, which corresponds to the strong segregation regime of the bulk microphase separation, see Section 3.1. The corresponding lamellar periodicity in the bulk with monomer concentration $\rho_{tot} = 0.85$ as estimated from the Lorentz fit to the first order peak of the structure factor averaged over 3 independent runs has the value $\lambda = 30.9$ and the average gyration radius of one block is $R^X = 3.8$.

We always choose equal system dimensions in the lateral directions $L_x = L_y = L$; for a given film thickness L_z and given L the number of molecules M in the simulation box is given by $M = \varrho_{tot} L_z L^2/(N_A + N_B)$.

In the following we consider two systems: a "thin" film with the film thickness $L_z = \lambda$ and a "thick" film with $L_z = 1.5\lambda$. The systems have the same dimensions in the lateral directions $L_x = L_y = 4\lambda$, the number of molecules in the thin film is $M = 3331$ and in the thick one $M = 4996$. As usual, we start the simulations with initial states where the molecules are uniformly distributed and randomly oriented inside the film. The initial values of parameters $\vec{r}_i$, R_i^A, and R_i^B are distributed according to their probabilities (2.20) and (2.21). To get good statistics, 10 independent runs with different initial configurations were carried out for each film thickness, the systems were left to equilibrate during the first 10^4 MCS after which at the final time ($2 \cdot 10^4$ MCS for the thin film and $4 \cdot 10^4$ MCS for the thick film) the quantities of interest were calculated and averaged over the last 10^4 runs.

5.1.1 Orientation

The constraints imposed on the molecules by the neutral walls makes the molecules to acquire a preferential parallel orientation. To show the reorientation of the molecules during the simulation, we calculate the quantity $\langle|\cos\Theta(z)|\rangle$, where $\Theta(z)$ denotes the angle between the vector $\vec{r}$ of a molecule with the center of mass located at z and the z-axis. $\langle ...\rangle$ means averaging over all the molecules in the system with the center of mass located in the grid unit $\triangle z = 1$ around the fixed z and all the independent runs. In the case of random orientations of molecules $\langle|\cos\Theta(z)|\rangle = \frac{1}{2\pi}\int d\Omega|\cos\Theta(z)| = \int_0^{2\pi} d\phi \int_0^{\pi} d\Theta(z)\sin\Theta|\cos\Theta(z)| = 0.5$, where Ω is the space angle. Values of $\langle|\cos\Theta(z)|\rangle$ below 0.5 would reflect the parallel orientation of the molecules at z. The results for various times and film thicknesses are shown in Fig. 5.1.

As clearly seen from the figure, at the short time $t = 200$ MCS molecules near the walls ($z = 0$ and $z = L_z$) prefer to assume a parallel orientation in both films, in the middle of the thin film there is a tendency to parallel orientation whereas in the thick film the molecule resume their random bulk orientation with $\langle|\cos\Theta(z)|\rangle$ close to 0.5. At the time $t = 2000$ MCS we observe a decrease in $\langle|\cos\Theta(z)|\rangle$ for the middle molecules indicating their preference for the parallel orientation, this effect being more pronounced in the thin film than in the thick one where the wall induced orientation encounters bulk microphase separation in the center of the film. An equilibrated state with a parallel orientation ($\langle|\cos\Theta(z)|\rangle \approx 0.35$) is reached at the time $t = 20000$ MCS in the thin film, in the thick film similar values of $\langle|\cos\Theta(z)|\rangle$ are reached at longer times (about $t = 40000$ MCS).

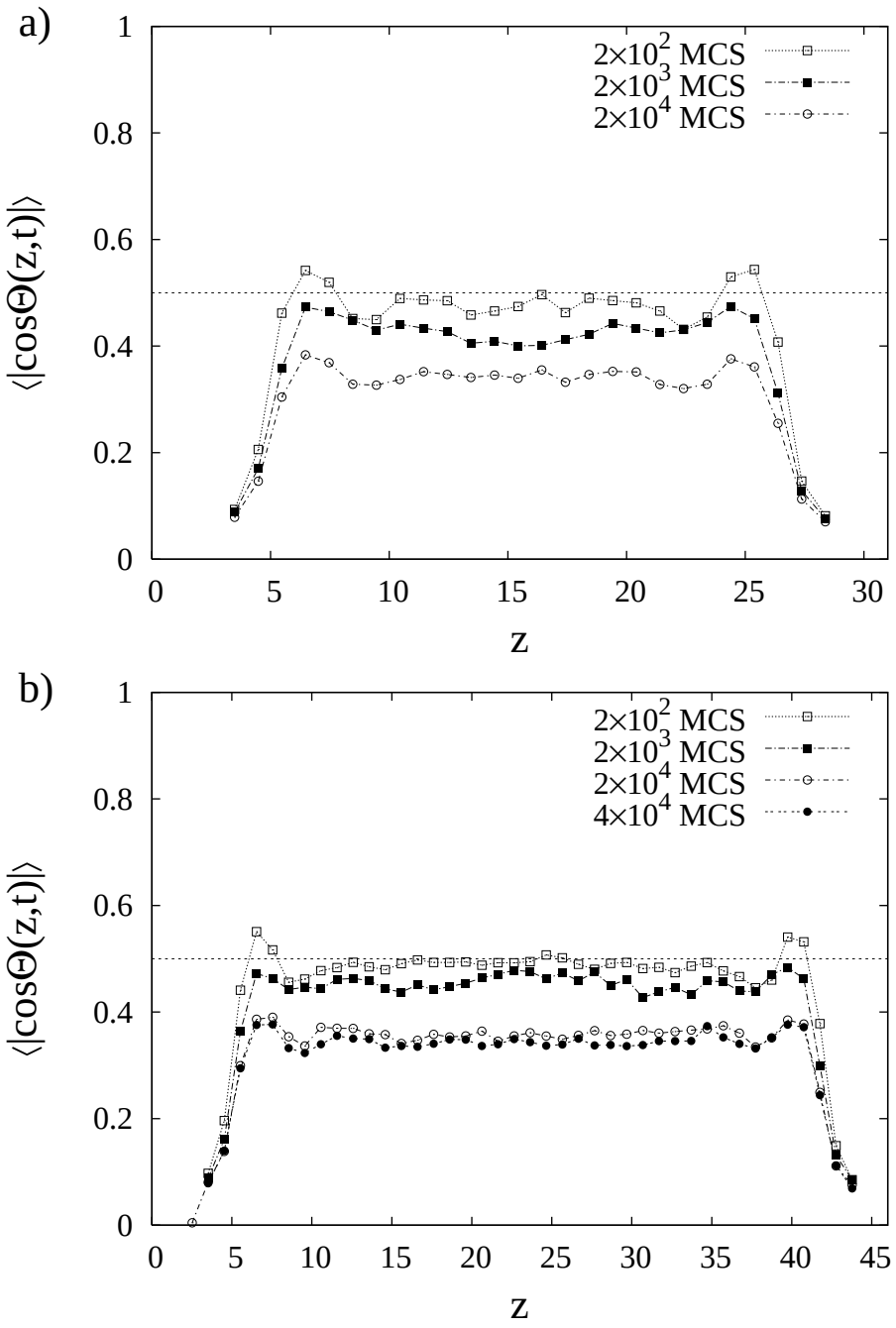

Figure 5.1: Wall-induced molecular orientation across the slab (neutral walls) at various times shown for film thicknesses (a) $L_z = \lambda$ and (b) $L_z = 1.5\lambda$.

Similar results on the equilibrated films with homogeneous walls were obtained in simulations of lattice polymers performed by Wang et al. in [Wan00a].

5.1.2 Deformation

Interaction with the wall alters the shape of the diblock copolymer molecule. It is known from computer simulations that the molecule near the wall gets compressed in the direction perpendicular to the wall and elongated in the lateral directions [Bas00b]. In the GDM the compression of the molecule would lead to a decrease in the gyration radii of individual blocks. However, values of the gyration radii smaller than the average R^A and R^B entering the conditional probability distribution of the center of mass distance r (see Eq. (2.21)) make large values of r quite improbable.

So we expect that our model while capable of catching the molecule compression in z direction

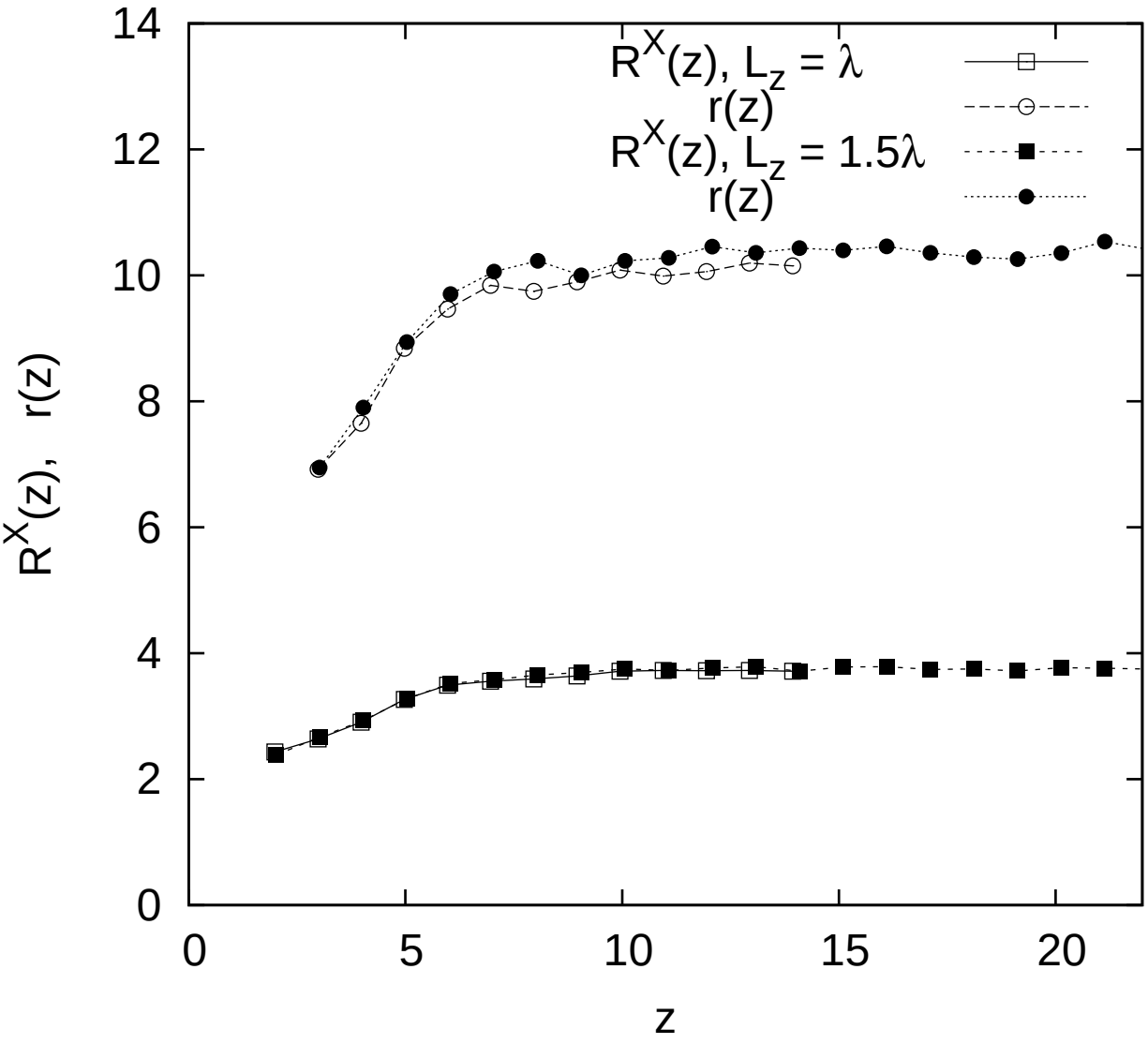

Figure 5.2: Center of mass distance $r(z)$ and the gyration radius of one block $R^X(z)$ as functions of separation z from the wall for films of thickness $L_z = \lambda$ and $L_z = 1.5\lambda$.

would fail to model the elongation along the wall. In Fig. 5.2 we present the center of mass distance $r(z)$ of molecules with the centers of mass located at z and the gyration radius $R^X(z)$ of blocks with their centers at z in equilibrated films of both thicknesses. As seen, the molecules near the walls become compressed in all the directions, while inside the film they retain bulk values of the gyration radii and the distance r.

To further test our model against properties in the slab we simulated a melt of $M = 8000$ homopolymers consisting of 60 monomers each confined in a very thin film of thickness L_z equal to the gyration radius of the block in the bulk, $R^X = 3.8$. The lateral dimensions of the system were chosen in the way that the average monomer density equals its bulk value. The

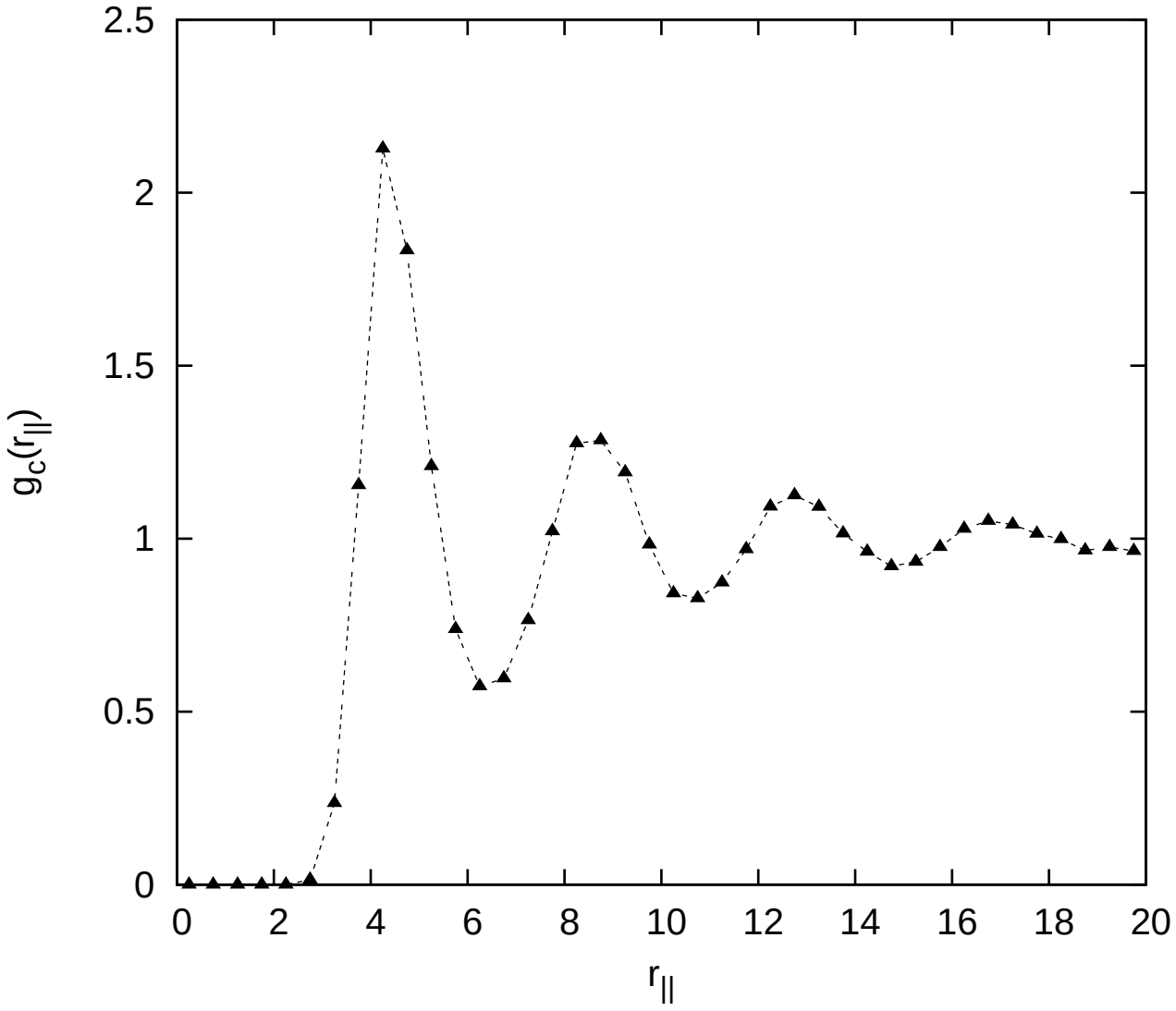

Figure 5.3: Lateral center-of-mass pair correlation function for homopolymers with the chain length $N = 60$ modelled as soft spheres in the slab of thickness $L_z = R^X = 3.8$ showing periodic fluctuations characteristic for a liquid-like order of the molecules.

walls are modelled with the same potential as in (5.3) and the homopolymers are represented as soft spheres whose radii of gyration obey the probability distribution of the block gyration radius in the GSM, Eq. (2.21). The strength of interaction between the monomers is the same as that of the monomers of the same type in the GSM.

The homopolymer molecules in the thin films behave like soft particles which can freely penetrate each other so that the center-of-mass pair correlation function should monotonically increase with distance to unity. We started the simulation from a disordered state, let the system thermalize and then calculated the lateral pair correlation function $g_c(r_\parallel)$ defined as

$$g_c(r_\parallel) = \frac{1}{\rho} \left\langle \sum_{j,k=1}^{M} \delta\left(\vec{r}_\parallel - \vec{r}_{k\parallel} + \vec{r}_{j\parallel}\right) \right\rangle , \tag{5.4}$$

where ρ is the mean monomer number concentration which was set to 0.85, $\vec{r}_\parallel = (x, y)$, $r_\parallel = |\vec{r}_\parallel| = \sqrt{x^2 + y^2}$ and $\vec{r}_{k\parallel}$ is the lateral position of the k-th particle. Fig. 5.3 shows $g_c(r_\parallel)$ obtained in the simulation. As seen from the figure, the pair correlation function has zero values up to about 2.2 (whereas the avaregad gyration radius of the spheres was estimated as 2.1) and then starts to oscillate about unity which is typical for the short range order in liguids with strong repulsion.

It follows from this observation that the GSM cannot be applied to study coarsening phenomena in very thin films of thicknesses becoming comparable with the gyration radius. We cannot expect the model to give a right description in the close vicinity to the walls where the radius of gyration becomes of the order of 2 and where we could not find a lateral elongation of the molecules.

5.1.3 Surface Directed Microphase Separation

To further quantify the order in the film and its evolution following a quench from a random initial state, we introduce the time-dependent lateral structure factor

$$S(\vec{k}_\parallel, z, t) = \frac{L_z}{MN_A} \langle |\varrho_A(\vec{k}_\parallel, z, t)|^2 \rangle \tag{5.5}$$

defined in terms of lateral density fluctuations

$$\varrho_A(\vec{k}_\parallel, z, t) = \int d^2 r_\parallel \varrho_A(\vec{r}, t) e^{i\vec{k}_\parallel \cdot \vec{r}_\parallel} \tag{5.6}$$

with $\vec{r}_\parallel = (x, y)$ and $\vec{k}_\parallel = (k_x, k_y)$, Appendix B. The prefactor L_z in (5.5) is introduced in order to achieve L_z-independence of (5.5) in the bulk limit $L_z \to \infty$ for given total monomer concentration, for details see Appendix B.

In Fig. 5.4 we show the lateral structure factor $S(k_\parallel, z, t)$ averaged over $\vec{k}_\parallel$ with $k_\parallel = (k_x^2 + k_y^2)^{1/2}$ fixed at various times for the system geometry $L_z = \lambda$. Simular results are obtained for the thicker film $L_z = 1.5\lambda$. As one can see from these figures, $S(k_\parallel, z, t)$ exibits a maximum throughout the whole film reflecting lateral ordering induced by the alignment effects described above. With increasing time the peak grows and at the final time $t = 20000$ we have a lamellar structure perpendicular to the walls well developed through the film.

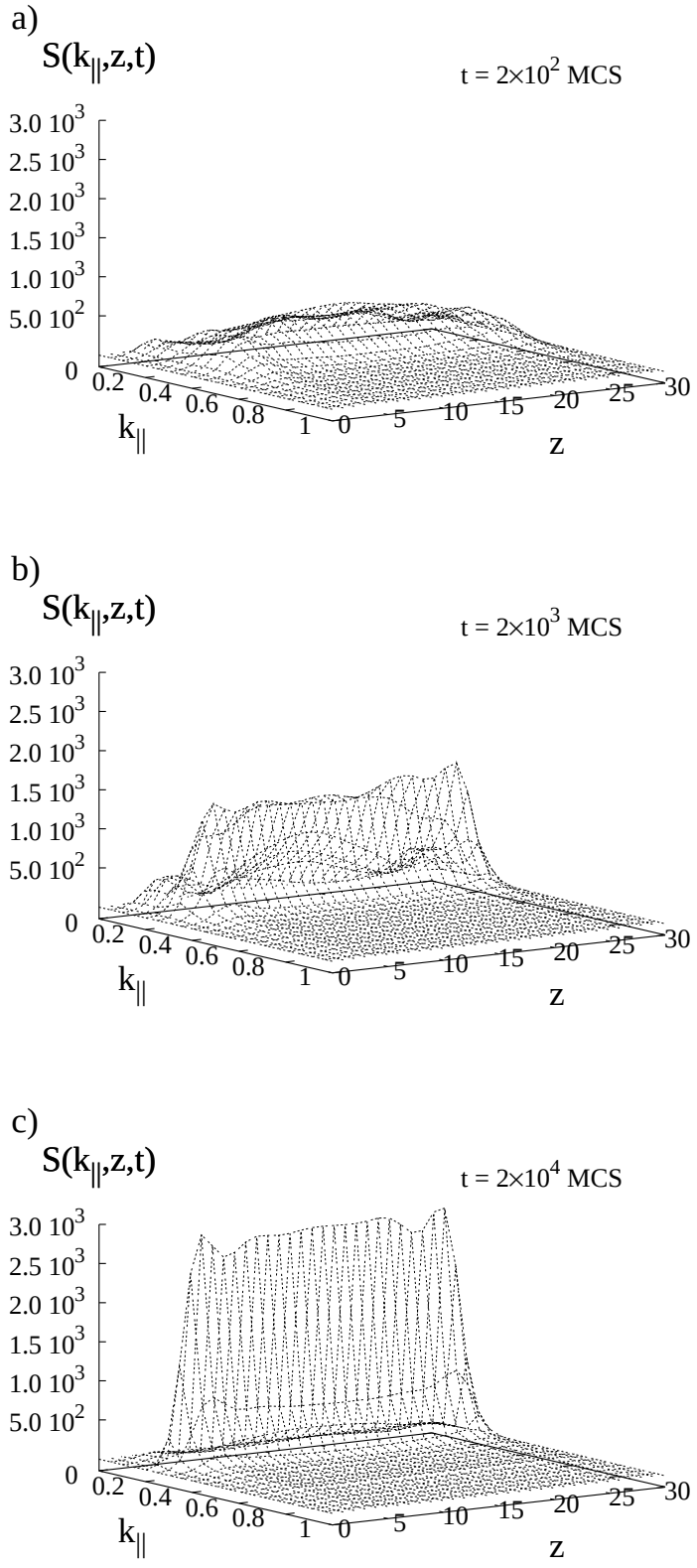

Figure 5.4: Circularly averaged structure factor $S(k_{\|}, z, t)$ for a film with neutral walls of thickness $L_z = \lambda$ at different times (a) $t = 200$ MCS, (b) $t = 2000$ MCS, and (c) $t = 20000$ MCS.

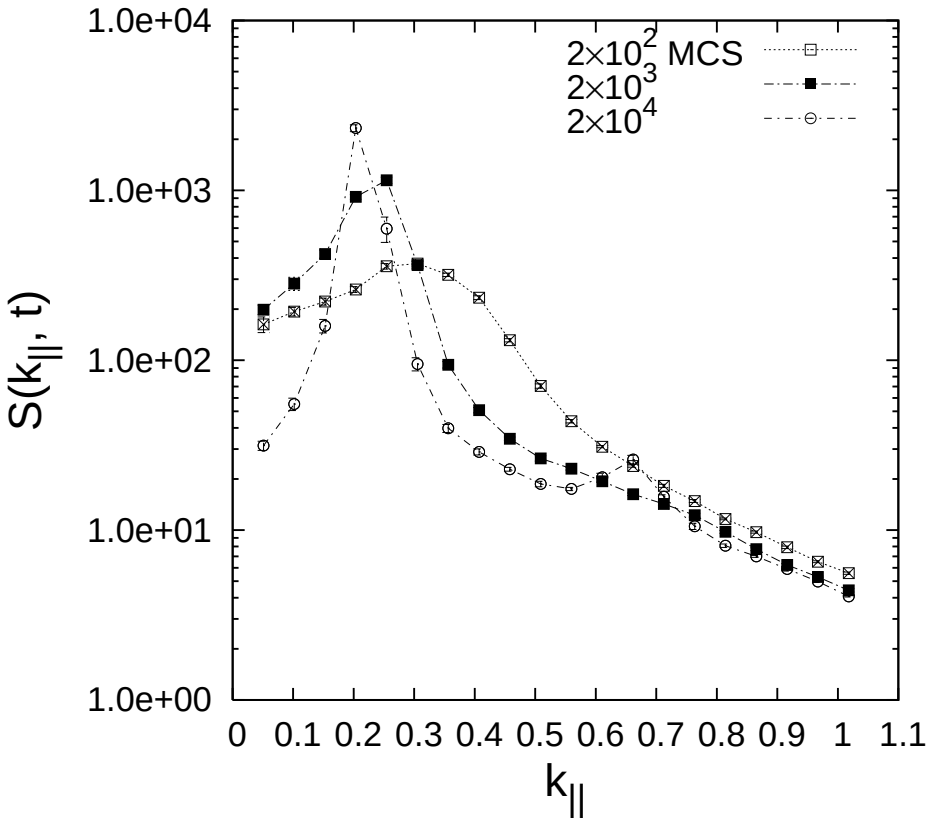

Figure 5.5: Time evolution of circularly averaged structure factor after averaging over z in the thin film with neutral walls, $L_z = \lambda$. Note the appearance of the 3rd-order peak in the final equilibrated state.

To quantify the dynamics of coarsening we average the circularly averaged structure factor $S(k_\parallel, z, t)$ over z which yields the function $S(k_\parallel, t)$ plotted in Fig. 5.5. $S(k_\parallel, t)$ has a maximum with its position $k^*_\parallel(t)$ becomming smaller during the coarsening and approaching a non-zero value, corresponding to the lamellar distance in the equilibrium state. The final lamellar periodicity has the same value as that in the bulk. A third order peak visible in the figure at the final time reflects a well ordered lamellar structure.

Fig. 5.6 shows isosurfaces of the perpendicular lamellar phase in the film with the thickness $L_z = \lambda$. The isosurfaces are perpendicularly oriented to the walls; the lamellar structure is locally ordered on the scale of two lamellar periods.

5.2 Parallel Lamellae between Homogeneous A-preferential Walls

5.2.1 Commensurate Thickness: $L_z/\lambda = 1$ and 2

Now we turn to the situation where the walls remain homogeneous but one or both of them prefer the A-component. To model an A-attractive wall we change the prefactor $\hat{\epsilon}_w$ in (5.1)

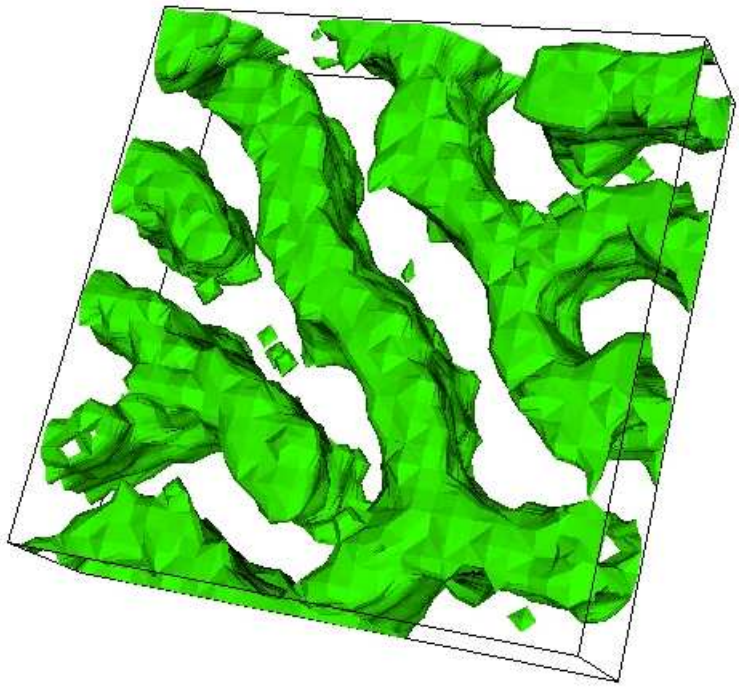

Figure 5.6: Isosurfaces of the perpendicular lamellar structure in the thin film with neutral walls at the time 20000 MCS, $L_z = \lambda$. The structure is equilibrated and has a local order which extends over two periods.

to $\hat{\epsilon}_w^A = \epsilon_w - \delta_w$ for A-monomers and $\hat{\epsilon}_w^B = \epsilon_w + \delta_w$ for B-monomers where the parameter δ_w is positive so that the A-preference of the wall means that the wall has a stronger repulsion for B than for A monomers. Choosing $\delta_w = 0.5$, the energetic preference of A-monomers is strong enough to overcome the essentially entropic alignment effect discussed before, that molecules near the wall have reduced orientational degrees of freedom. First we consider films of a commensurate geometry with thicknesses $L_z = \lambda$ (lateral dimensions $L_x = L_y = 4\lambda$ and the number of molecules $M = 3331$) and $L_z = 2\lambda$ ($L_x = L_y = 3\lambda$, $M = 3747$). We made 5 independent runs for symmetric films with A-attractive upper and lower walls and 10 runs for asymmetric films with A-attractive upper and neutral lower walls.

In Fig. 5.7a the corresponding A-monomer density $\rho_A(z,t)$ is plotted across the symmetric film of thickness $L_z = \lambda$. Layers of A-monomers adjacent to the walls rapidly form and get separated by a B-rich domain. Notice a peak of the A-density in the center of the film which emerges at initial times of the simulation. Its origin is due to the fact that the initial formation of the A-rich layers goes through a fast reorientation of the molecules located close to the walls

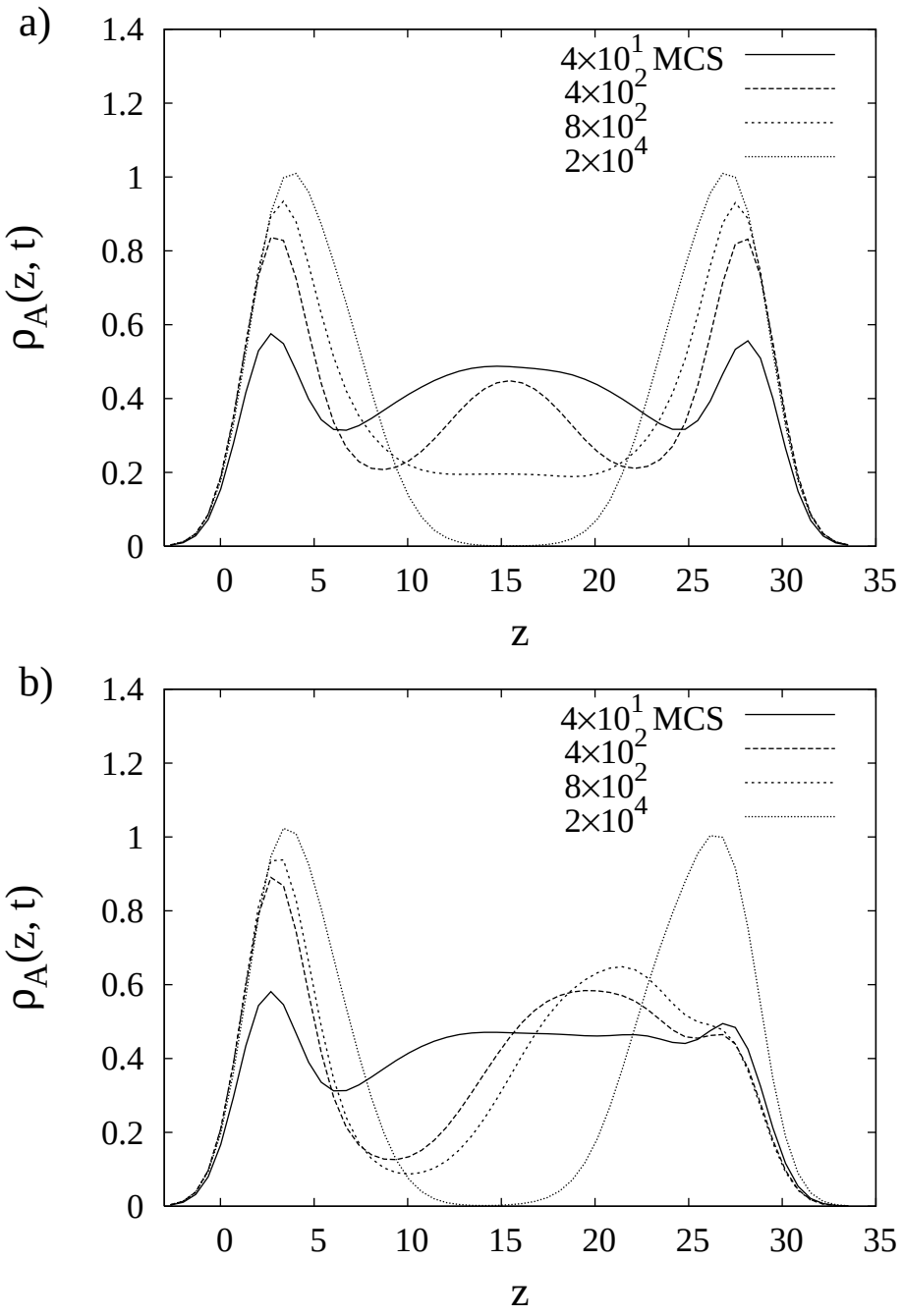

Figure 5.7: (a) Time evolution of the A-monomer density in a film of thickness $L_z = \lambda$ with A-attractive walls, for $\chi = 0.45$ (b) same, but with A-attractive left and neutral right wall. Systems with both types of walls develops $A - B - A$ lamellar structure across the film.

which leads to some depletion of A-monomers in the adjacent regions. Diffusion of A-blocks from the center of the film is not fast enough to compensate this depletion at initial times. The peak decreases in hight and disappears at 800 MCS. The final profile of the A-monomer density which becomes equilibrated at about $2 \cdot 10^4$ MCS has two well defined peaks at the

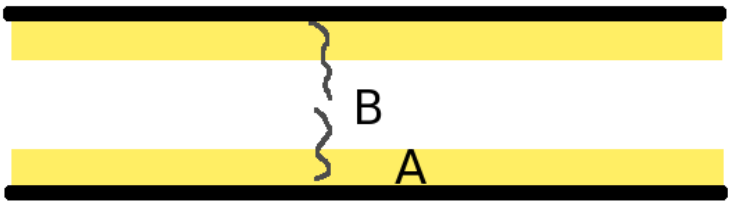

Figure 5.8: Schematic representation of the parallel lamellar structure observed between two homogeneous A-attractive walls, the film thickness $L_z = \lambda$.

walls and decreases towards the middle of the film where it has zero values. In the middle of the film we observe a peak in the B-monomer density (not presented here), a clear indication of lamellae parallel to the walls. A schematic representation of the structure is shown in Fig. 5.8.

When the wall at $z = L_z$ is replaced by a neutral one, the equilibrium density profile (40000 MCS) essentially remains symmetric, see Fig. 5.7b. At 400 MCS we observe a peak of the A-monomer density located near the middle of the film which then moves due to reorientation of the molecules towards the neutral wall. Thus the A-attractive wall induces layering almost as in Fig. 5.7a. Development of the A-rich layer near the neutral wall, however, takes much longer time than in Fig. 5.7a. The whole situation is reminiscent of wall-induced spinodal decomposition in films of binary polymer blends, at least in its early stages [Eudiss], [Pur97], [Fis98].

In Fig. 5.9 we plot the z dependent A-monomer density in symmetric and asymmetric films of thickness $L_z = 2\lambda$. In the symmetric film, Fig. 5.9a, we observe A-rich layers already formed at the walls at the time 40 MCS, then at the time 400 MCS two additional peaks appear, reflecting two A-rich layers in the middle of the film. The peaks move towards each other (800 MCS) and then coincide to form one layer in the film center at the final time $2 \cdot 10^4$ MCS. The ordering process is different in the asymmetric film, Fig. 5.9b, where we have an "ordering wave" resulting in appearance of the first layer at the A-attractive wall, a gradual increase of the second layer, its movement towards the center of the film followed by a development of the third layer at the opposite neutral wall. The final equilibrated structures in both films are quite similar and consist of lamellae parallel to the walls, see Fig. 5.10, the equilibration time in the asymmetric film is two times larger as that in the symmetric film.

5.2.2 Incommensurate Thickness: $L_z/\lambda = 1.5$

So far the thickness of the film with A-attractive walls (or A-attractive lower and neutral upper walls) was an integer multiple of the bulk lamellar periodicity so that the parallel lamellae observed were not compressed or stretched. Now we study the microphase separation in films of thickness incommensurate with the bulk periodicity. In Fig. 5.11a we plot the A-monomer density as a function of z in the symmetric film of thickness $L_z = 1.5\lambda$ with A-attractive upper and lower walls. The time evolution of the A-density profile runs quite similar to that of the parallel lamellar structure formation in Fig. 5.9 except that there is only one peak in the middle at all the times. The final structure is compressed parallel lamellae with the periodicity $\lambda_f = 3/4\lambda$.

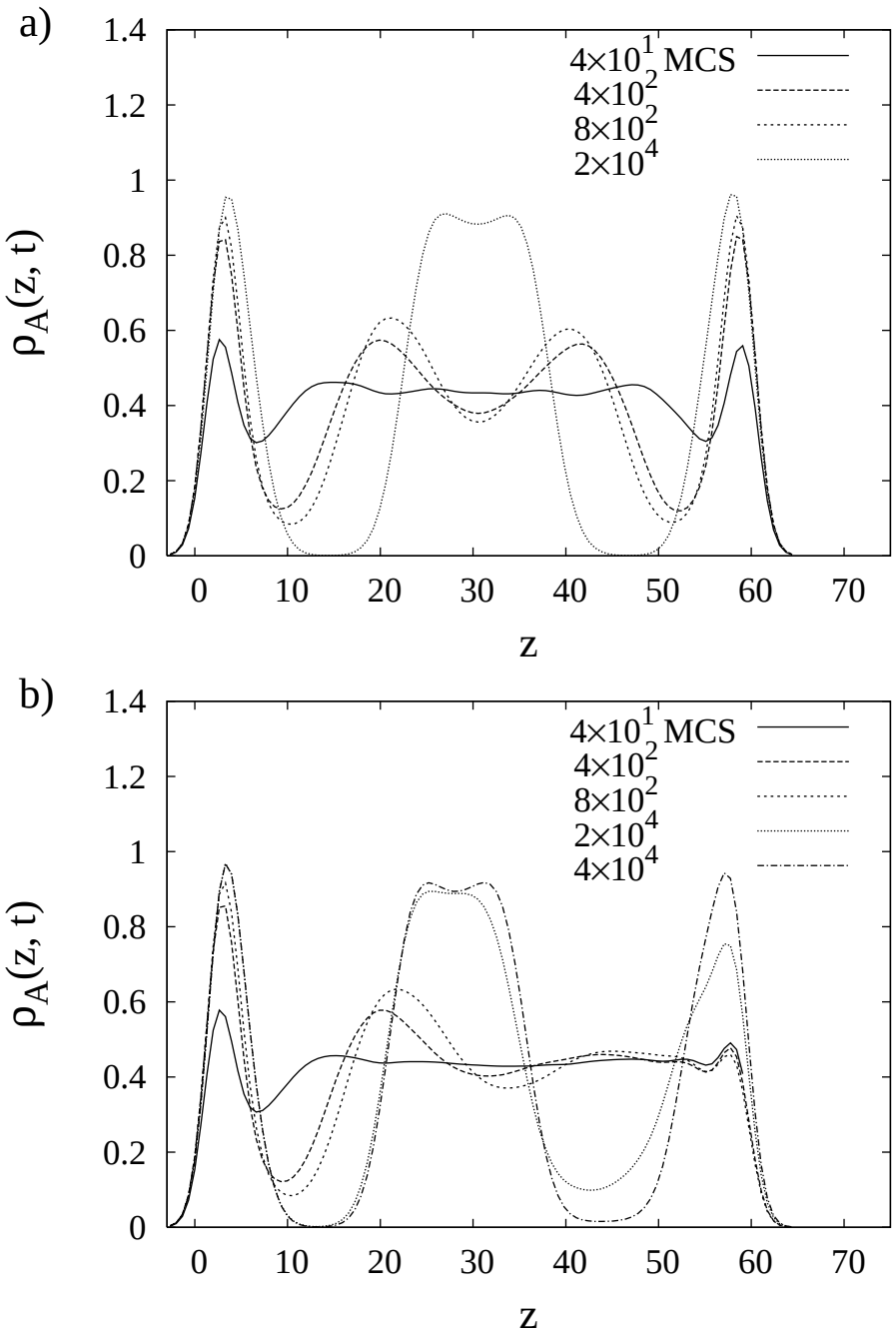

Figure 5.9: (a) Time evolution of the A-monomer density in a film of thickness $L_z = 2\lambda$ with A-attractive walls, for $\chi = 0.45$ (b) same, but with A-attractive left and neutral right wall. The systems develops $A - B - A - B - A$ lamellar structure across the film.

The time evolution of the A-density profile in an asymmetric film of the same thickness, Fig. 5.11b, shows the same features as in the asymmetric film of the Fig. 5.9b with an ordering wave of parallel lamellae moving from the A-attractive lower wall towards the neutral upper one. The A-density profile gets equilibrated at about $2 \cdot 10^4$ MCS having one peak at the lower

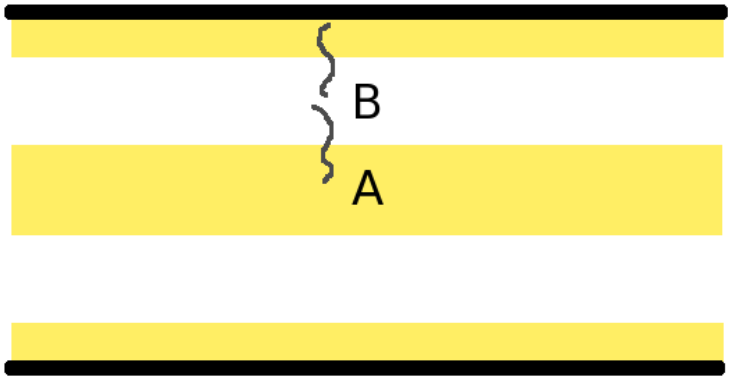

Figure 5.10: Schematic representation of the $A-B-A-B-A$ structure observed in films confined between two A-attractive walls, Fig. 5.9a, and A-attractive and neutral walls, Fig. 5.9b. The film thickness $L_z = 2\lambda$.

wall and the second peak near the middle of the film. It decreases gradually to zero values at the neutral upper wall where the B-monomer density (not presented here) shows a peak similar to the peak at the lower wall.

5.3 Periodically Patterned Walls

In this section we study the kinetics of pattern transfer into films of diblock copolymer melts deposited on chemically heterogeneous surfaces. The surface is patterned periodically with stripes parallel to the x axis consisting of alternating A- and B-attractive regions. The substrate is modeled by a periodic potential applied at the lower wall

$$V_w(y,z) = \epsilon_w \left[1 + \delta_w^X \cos(k_p y)\right] \exp\left(-\frac{z}{2\,l_w}\right) , \tag{5.7}$$

where $\epsilon_w = 2$, $\delta_w^B = -\delta_w^A = \delta_w = 0.5$, $k_p = 2\pi/L_p$, and L_p is the period of the AB stripe. As in the case of homogeneous walls studied in the previous section, the overlap integral in (5.3) can be calculated analytically. The opposite wall remains neutral with the potential as in (5.1) but without the first term.

To monitor the time evolution of the coarsening, we use the integrated structure factor

$$S(k_y,z,t) = \int dk_x S(\vec{k}_\parallel,z,t)\,, \tag{5.8}$$

which reflects A-monomer density modulations in the y direction, for the quantity $S(\vec{k}_\parallel,z,t)$ see Appendix B.

As long as $\chi N < (\chi N)_c$, the equilibrium state displays a periodic segregation of monomers in the y-direction confined near $z = 0$. From previous bulk simulations, the position $(\chi N)_c$ of the ODT in the melt of symmetric diblock copolymers of the chain length $N = 120$ was estimated to lie between 15.0 and 16.5, section 3.1. We studied a thin film of the diblock copolymer melt

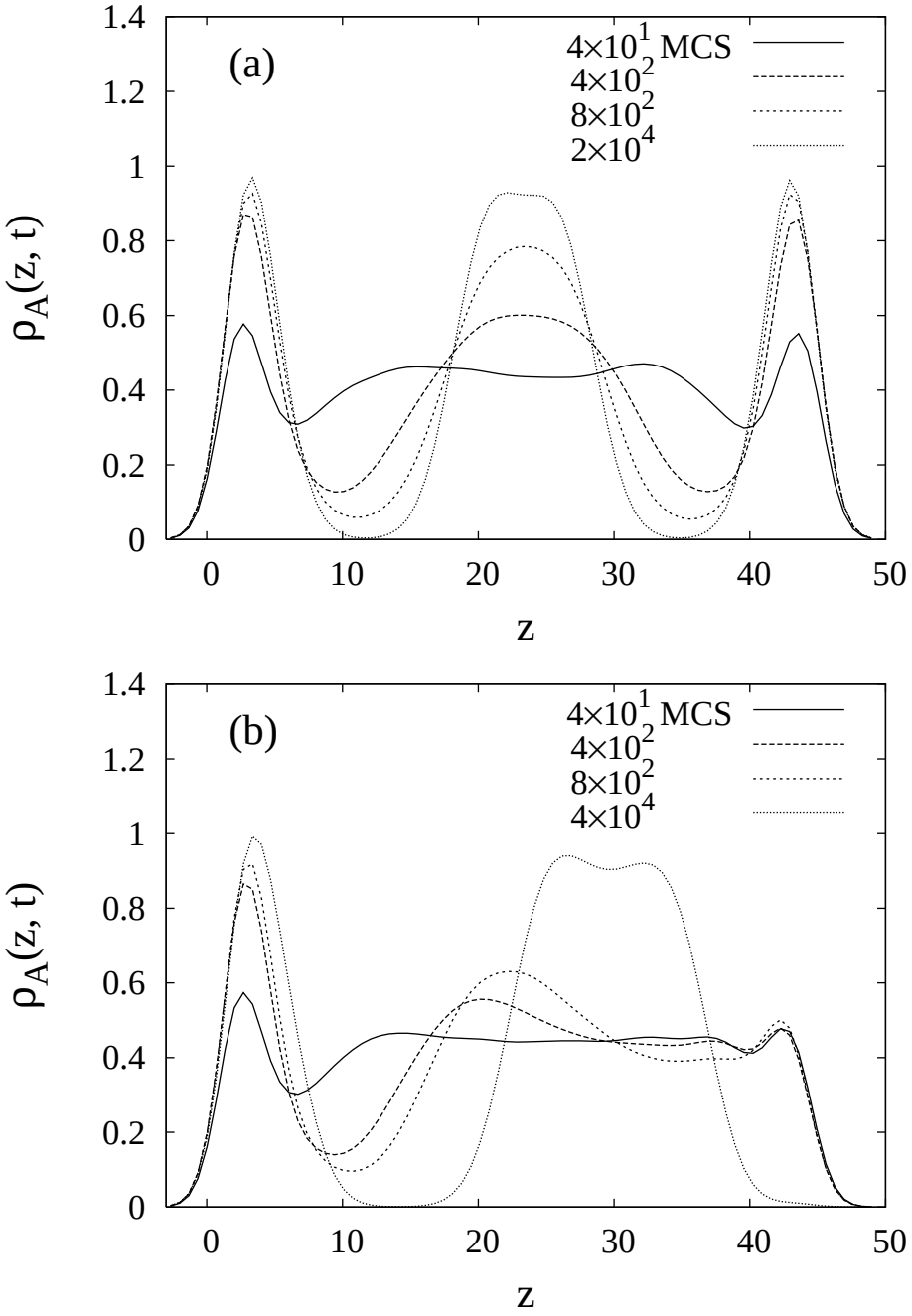

Figure 5.11: (a) Time evolution of the A-monomer density in a film of incommensurate thickness $L_z = 1.5\lambda$ with A-attractive walls, for $\chi = 0.45$ (b) same, but with A-attractive left and neutral right wall.

in the disordered phase near the ODT ($\chi N = 15.0$). The film has a thickness $L_z = 1.5\lambda_{dis}$ with the lateral dimensions $L_x = L_z = 4\lambda_{dis}$, where $\lambda_{dis} = 21.06$ is the position of the maximum of the structure factor in the disordered bulk at $\chi N = 15.0$. The pattern periodicity was set to $L_p = 2\pi/k_p = \lambda_{dis}$.

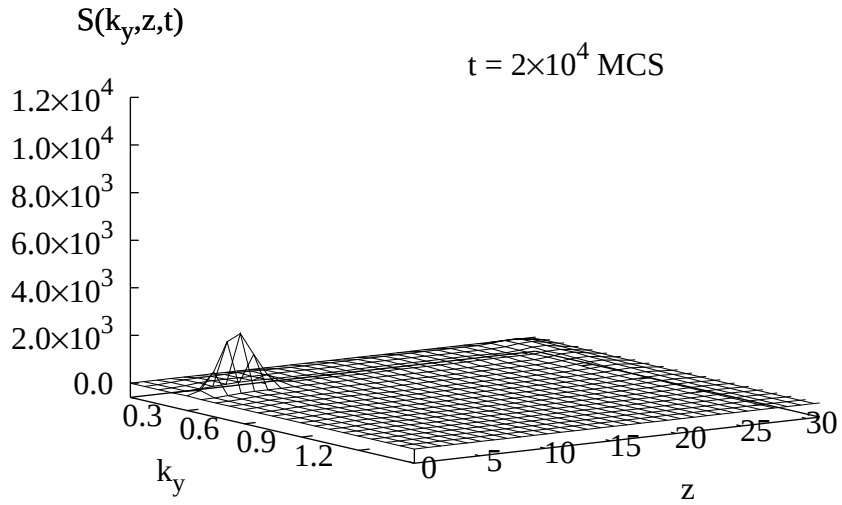

Figure 5.12: Structure factor $S(k_y, z, t)$ at the time $t = 2 \times 10^4$ MCS in the presence of a stripe-patterned wall near $z = 0$ at $\chi = 0.15$ (disordered phase). The upper wall is neutral. The pattern periodicity is $L_p = 2\pi/k_p = \lambda$ where k_p was estimated with the Leibler fit from bulk simulations and the film thickness $L_z = 1.5\lambda$. The lateral system size is $L_x = L_y = 4L_p$.

The structure factor $S(k_y, z, t)$ exibits a peak near the substrate at 2000 MCS with $k_y = k_p$ which remains located at the wall as the time proceeds. We plot $S(k_y, z, t)$ averaged over 5 runs at the time $2 \cdot 10^4$ MCS in Fig. 5.12, where one can see that the position of the maximum is at a distance R^X from the substrate. The peak in the structure factor is caused by modulations in the A-monomer density along the y-axis located within a distance $2R^X$ from the substrate which however cannot develop further. The decay of the segregation amplitude along the z-axis reflects the correlation length of the disordered phase. The substrate pattern does not penetrate further into the film as the time proceeds beyond $2 \cdot 10^4$ MCS.

On the other hand, in the ordered phase $\chi N > (\chi N)_c$ various scenarios of pattern-induced microphase separation emerge, depending on film thickness and on the commensurability between the two length scales L_p and λ. In the following we study the pattern transfer in the strong segregation regime with $\chi N = 54.0$; the results are always averaged over 10 independent runs.

5.3.1 Commensurate Systems: $L_p/\lambda = 1$

When the surface pattern period equals the bulk lamellar period $L_p = \lambda$, we observe perpendicular lamellae in register with the surface pattern throughout the entire film, see Fig. 5.13. Figs. 5.14 and 5.15 show the time evolution of the integrated structure factor $S(k_y, z, t)$ and the circularly averaged structure factor $S(k_\parallel, t)$, Eq. (5.5), after averaging over z in the film of thickness $L_z = \lambda$ (lateral dimensions $L_x = L_y = 4L_p$). At the time 200 MCS, see Fig. 5.14a,

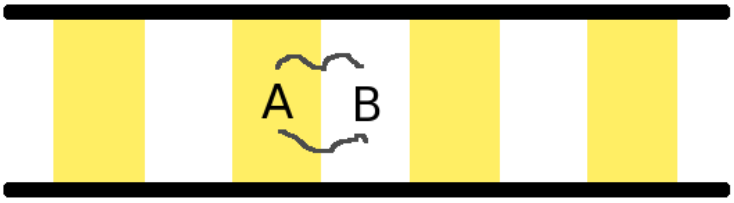

Figure 5.13: Schematic representation of perpendicular lamellae in register with the substrate pattern. The film thickness $L_z = \lambda$.

one can observe a rapid growth of a peak with $k_y \simeq k_p$ near the patterned substrate, which has a higher maximum than that in the disordered phase at $2 \cdot 10^4$ MCS in Fig. 5.12. Simultaneously, a broader structure develops across the slab indicating spontaneous microphase ordering similar to bulk behavior. This structure is visible also as an additional broad shoulder at 200 MCS in Fig. 5.15 which gets smaller at 2000 MCS. As the time proceeds, Fig. 5.14b (2000 MCS), we observe a further increase in the maximum of the peak and its propagation into the film, meaning suppression of the spontaneous ordering in the middle of the film.

At earlier times (about 200 MCS) a smaller additional peak in $S(k_p, z, t)$, Fig. 5.14a, and a well defined minimum near $z \approx 6.5$ can be observed in between these two main features. The z-dependence of $\langle |\cos\Theta(z)| \rangle_{\text{eq}}$, see Fig. 5.16a exibits a peak near $z \simeq 6.5$ with the maximum above the disordered value 0.5 which means that molecules whose centers of mass are located at this distance prefer perpendicular orientation. The minimum position in the structure factor locates the distance from the substrate where the centers of mass of the perpendicularly oriented molecules are distributed, suppressing lateral modulation of the monomer density. The whole structure in this region resembles one layer of the checkerboard morphology, see Fig. 5.23. This transient structure costs an additional penalty in the block-block interfacial energy and disappears at 2000 MCS.

At the final time $t = 2 \times 10^4$ MCS, Fig. 5.14c, the wall-induced sharp structure dominates everywhere and has penetrated the slab nearly uniformly. A weak 3rd-order peak reflecting strong segregation of A- and B-rich regions is clearly seen at $k_y \simeq 3k_p$ at the time 2×10^4 MCS, see Fig. 5.15. The result is an equilibrium state with nearly perfect perpendicular lamellar ordering reflected in Fig. 5.16b where we plot the y dependent A-monomer density averaged over the xz plane. The chain orientational profile at the final time shown in Fig. 5.16a confirms the preferential parallel orientation of molecules throughout the entire film. Note that the hight of the peak in Fig. 5.14c becomes a little larger near the substrate where the molecules are forced to parallel alignment, Fig. 5.16a, favouring a stronger segregation of A- and B-rich regions.

In Fig. 5.17 we show the equilibrated lamellar structure at the time 2×10^4 MCS represented by the isosurfaces. Opposite to Fig. 5.6 the structure is globally ordered and in register with the substrate pattern.

For a thicker film with $L_z = 1.8\lambda$, one can see a similar rapid increase of a peak at the substrate at early times (200 MCS, Fig. 5.18a.) However, "bulk-like" ordering processes throughout the slab evolve further and more strongly interfere with the ordering wave propagating from the patterned wall, so that the pattern propagation slows down (2000 MCS, Fig. 5.18b). For

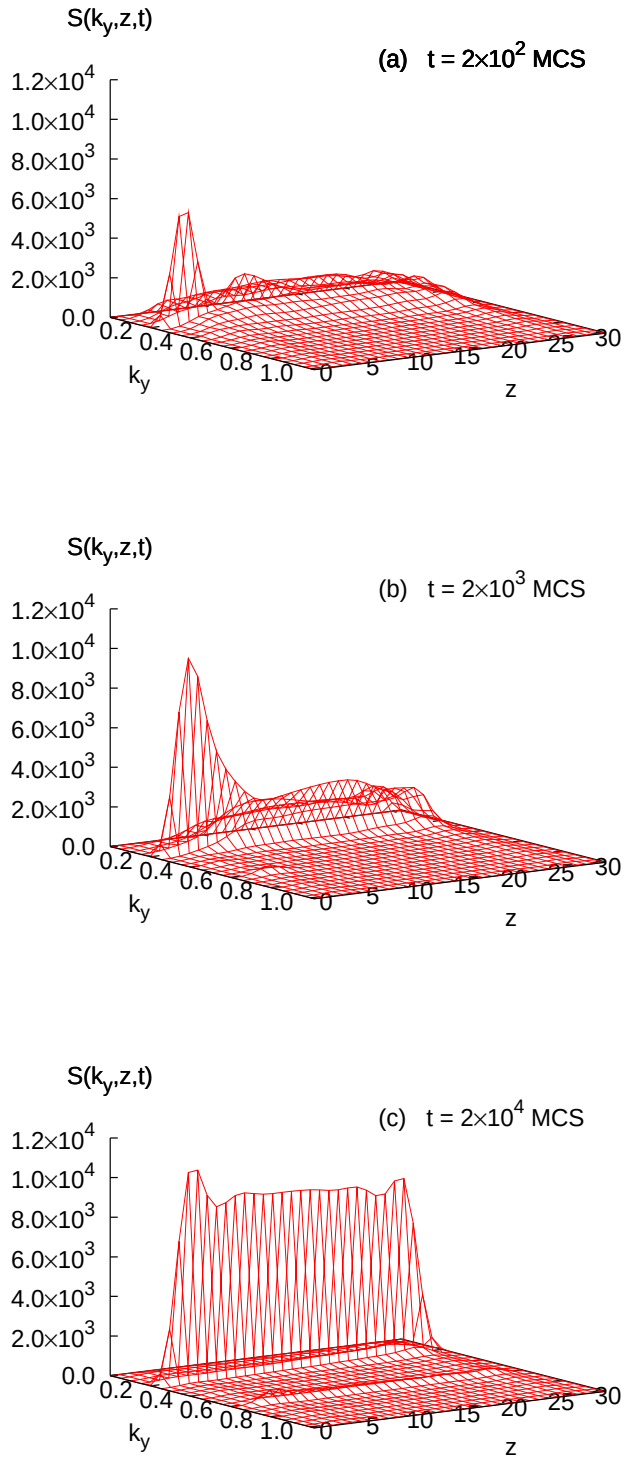

Figure 5.14: Time evolution of the structure factor $S(k_y, z, t)$ in the presence of a stripe-patterned wall near $z = 0$, for $\chi = 0.45$. The pattern periodicity is $L_p = 2\pi/k_p = \lambda$ and the film thickness $L_z = \lambda$. The lateral system size is $L_x = L_y = 4L_p$. (a) $t = 200$ MCS, (b) $t = 2 \times 10^3$ MCS, (c) $t = 2 \times 10^4$ MCS.

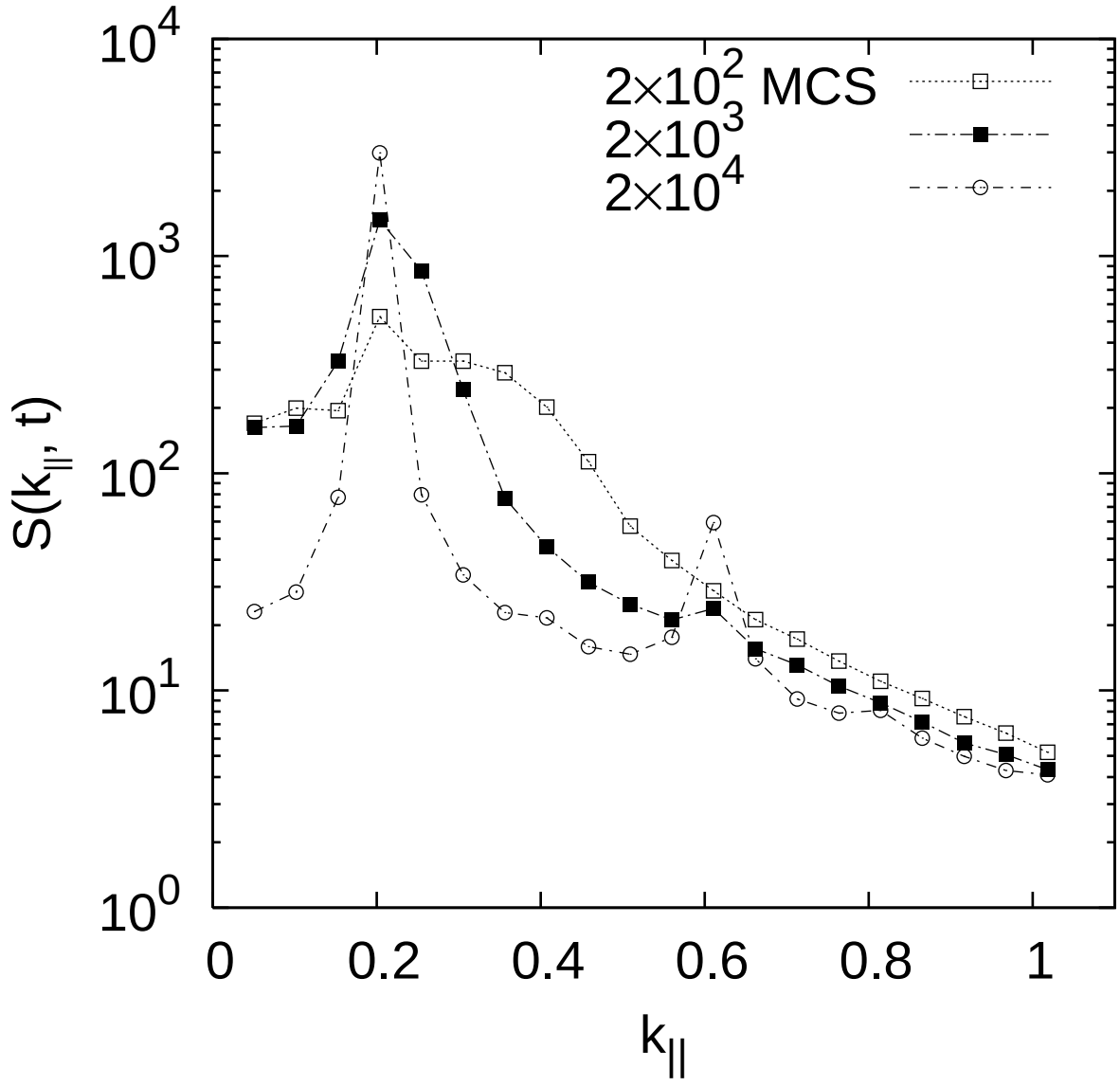

Figure 5.15: Time evolution of circularly averaged structure factor after averaging over z in the commensurate films of thickness $L_z = \lambda$, see Fig. 5.14

much longer times than those in the thin film, the ordering wave finally succeeds to overcome the bulk-like domain structures. Equilibrium is nearly but not fully reached at $t = 4 \times 10^4$ MCS, see Fig. 5.18c.

5.3.2 Incommensurate Systems: $L_p/\lambda = 1.1$ and 1.2

Now we turn to incommensurate situations when $L_p \neq \lambda$. A new feature is added to the competition between the pattern-induced ordering at the substrate and the bulk-like behavior in the rest of the film studied before. To adopt the pattern periodicity, molecules should be stretched which can slow down the pattern propagation into the film or even limit the depth

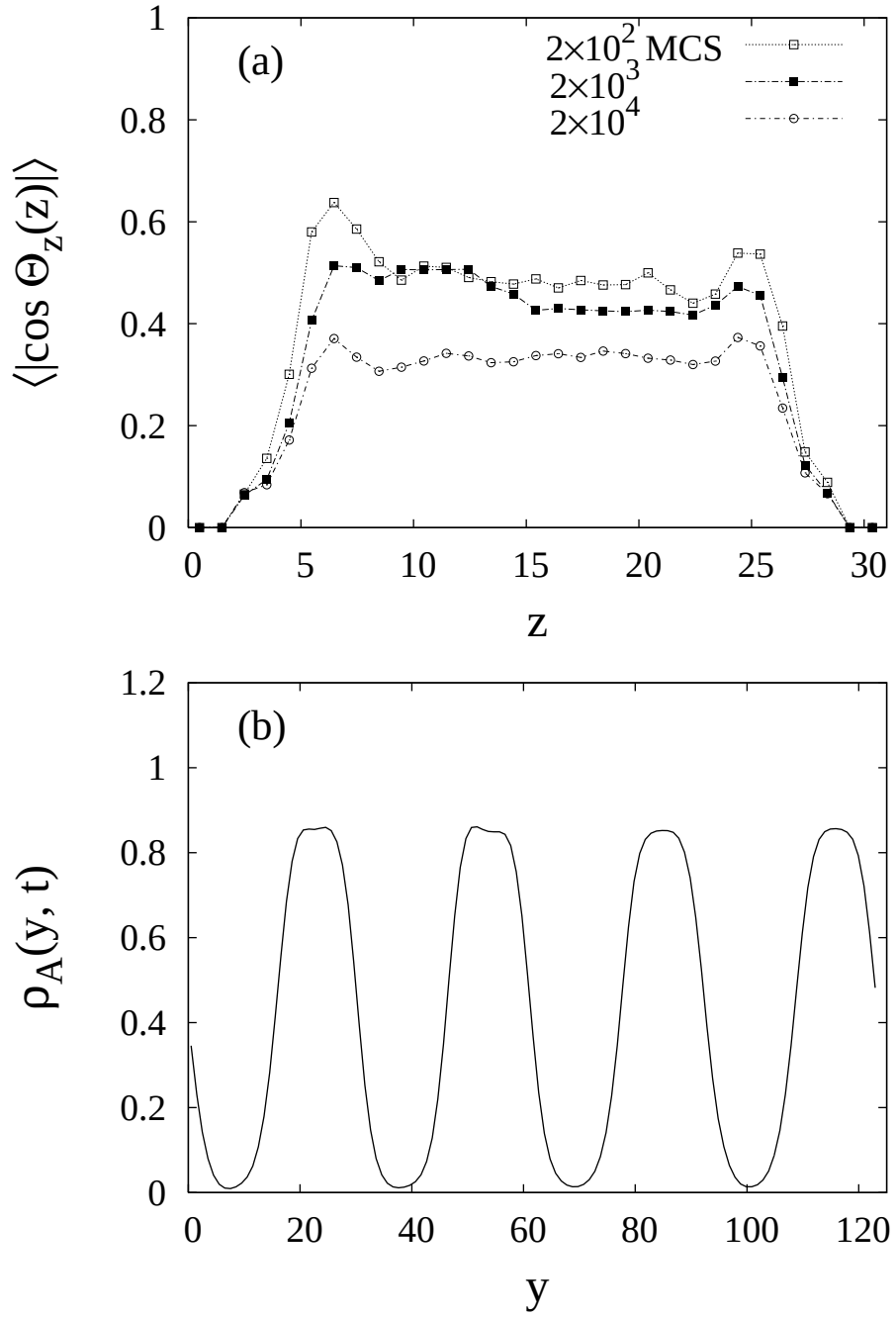

Figure 5.16: (a) Wall induced molecular orientation at different times and (b) A-monomer concentration in the y direction in commensurate patterned film of thickness $L_z = \lambda$ at the final time 20000 MCS.

of the penetration.

In the following, to keep the periodic boundary conditions, we set the lateral dimensions of the systems to $L_x = L_y = 4L_p$. The case $L_p/\lambda = 1.1$ and $L_z = \lambda$ will be described briefly because of its similarity at long times to the commensurate case $L_p/\lambda = 1.0$ shown in Fig. 5.14.

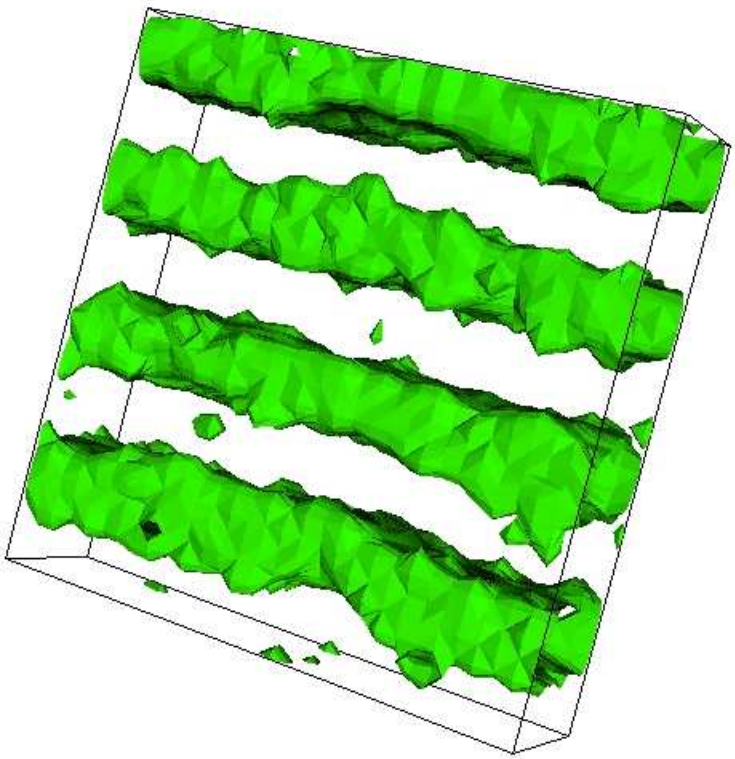

Figure 5.17: Isosurfaces of the perpendicular lamellar structure in the thin film with the patterned substrate at the time 20000 MCS, $L_z = \lambda$. The structure is equilibrated and has a global order, compare with Fig. 5.6.

The main difference at shorter times is most directly observed from the structure factor $S(k_\parallel, t)$ plotted in Fig. 5.19. Whereas in both cases the primary peak at $k_y = k_p$ has the same magnitude at the time 200 MCS, Figs. 5.15 and Fig. 5.19, bulk ordering in the commensurate case initially leads to a shoulder in $S(k_\parallel, t)$ next to the peak at k_p, which merges with it as time proceeds.

On the other hand, for $L_p/\lambda = 1.1$ and $t = 200$ MCS one can identify a separate "bulk" peak. It also merges with the peak at k_p for longer times $t > 2 \times 10^4$ MCS so that the final structure corresponds to complete penetration of the wall pattern (visible at $t = 4 \times 10^4$ MCS in the Fig. 5.19, where $S(k_\parallel, t)$ shows a weak 3rd-order peak), as in the commensurate case. It is interesting to note that transient coexistence of two peaks and final dominance of the peak at k_p have been observed recently in two-dimensional Fourier transforms of real space images of diblock copolymer thin films on chemically nanopatterned substrates [Edw05].

By contrast, for the larger ratio $L_p/\lambda = 1.2$ with $L_z = \lambda$ the two main features in Figs. 5.20a - c prevailing near the patterned wall and deeper in the film, respectively, remain separated

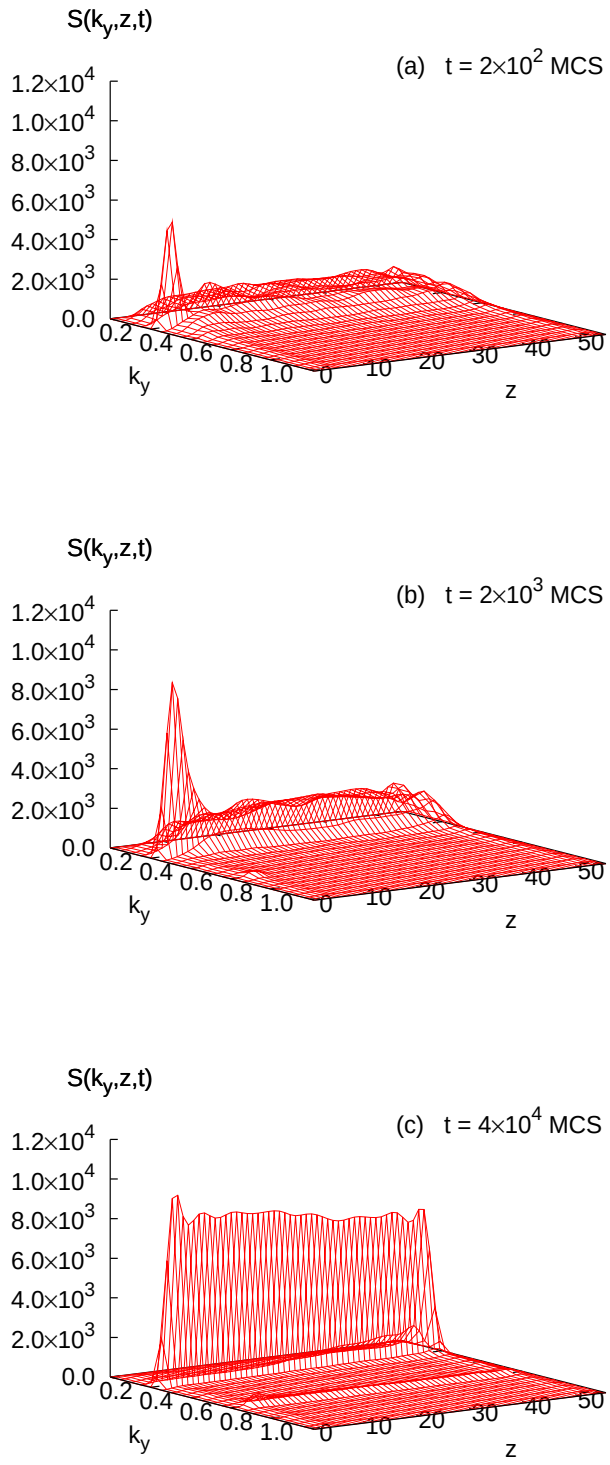

Figure 5.18: Same as Fig. 5.14, but $L_z = 1.8\lambda$. The equilibration takes more time than in the thin film of Fig. 5.14.

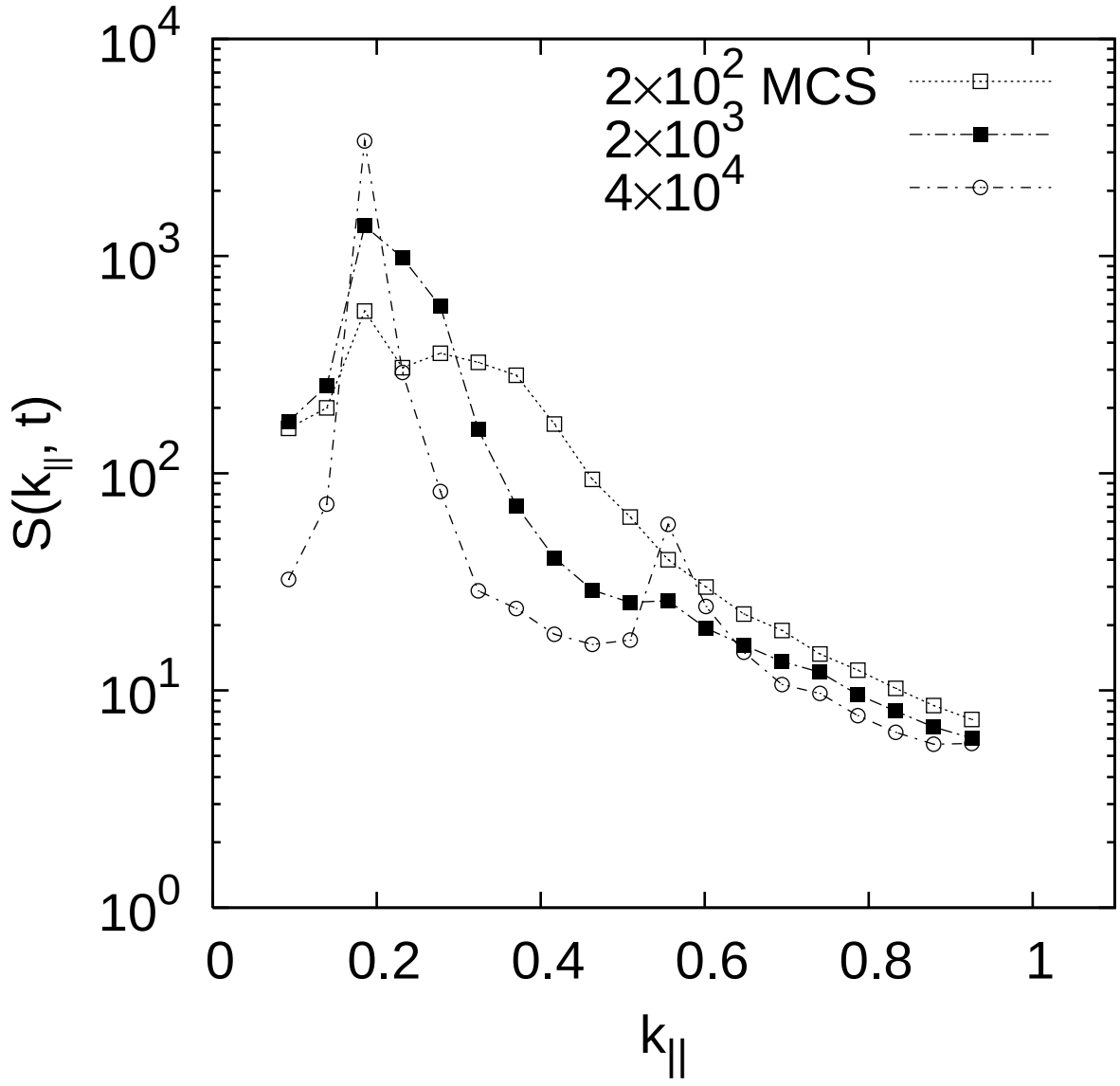

Figure 5.19: Time evolution of the structure factor $S(k_{\|}, t)$ in the incommensurate films with $L_p/\lambda = 1.1$ and the thickness $L_z = \lambda$.

with respect to k_y as time proceeds. Up to $t = 2 \times 10^3$ MCS the peak at k_p dominates, which is evident from $S(k_y, z, t)$ in Figs. 5.20a - b as well as from the averaged structure factor $S(k_{\|}, t)$ plotted in Fig. 5.21, whereas for $t > 2 \times 10^4$ the quantity $S(k_{\|}, t)$ takes an additional maximum at the bulk value $k_0 = 2\pi/\lambda$.

No further change of this pattern is observed in our longest runs up to $t = 6 \times 10^4$ MCS, nor does it change when we increase the strength in the modulation of the wall potential to $\delta_w = 0.75$ or when we replace the sinusoidal modulation by a well-like potential with the amplitude 0.5. Hence it appears that no well-ordered structure develops in this case, showing that transfer of the wall pattern into the film sensitively depends on the commensurability of the two length scales L_p and λ.

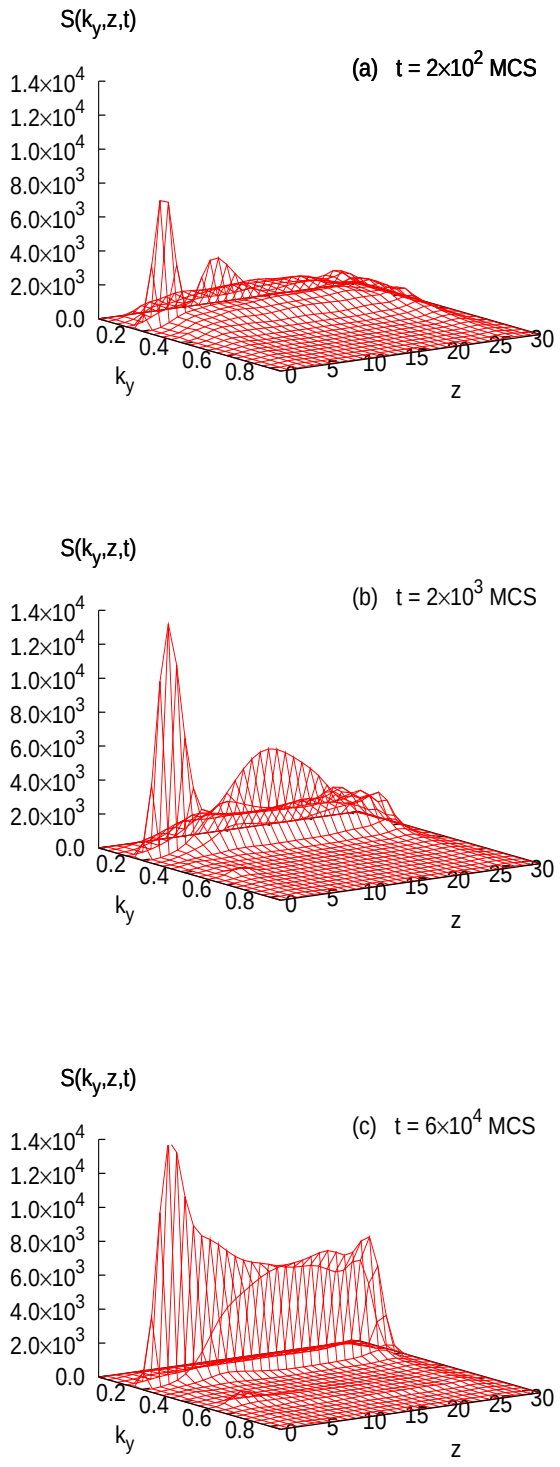

Figure 5.20: Same as Fig. 5.14, but $L_p/\lambda = 1.2$ (strong incommensurability), and $t = 6 \times 10^4$ MCS in (c).

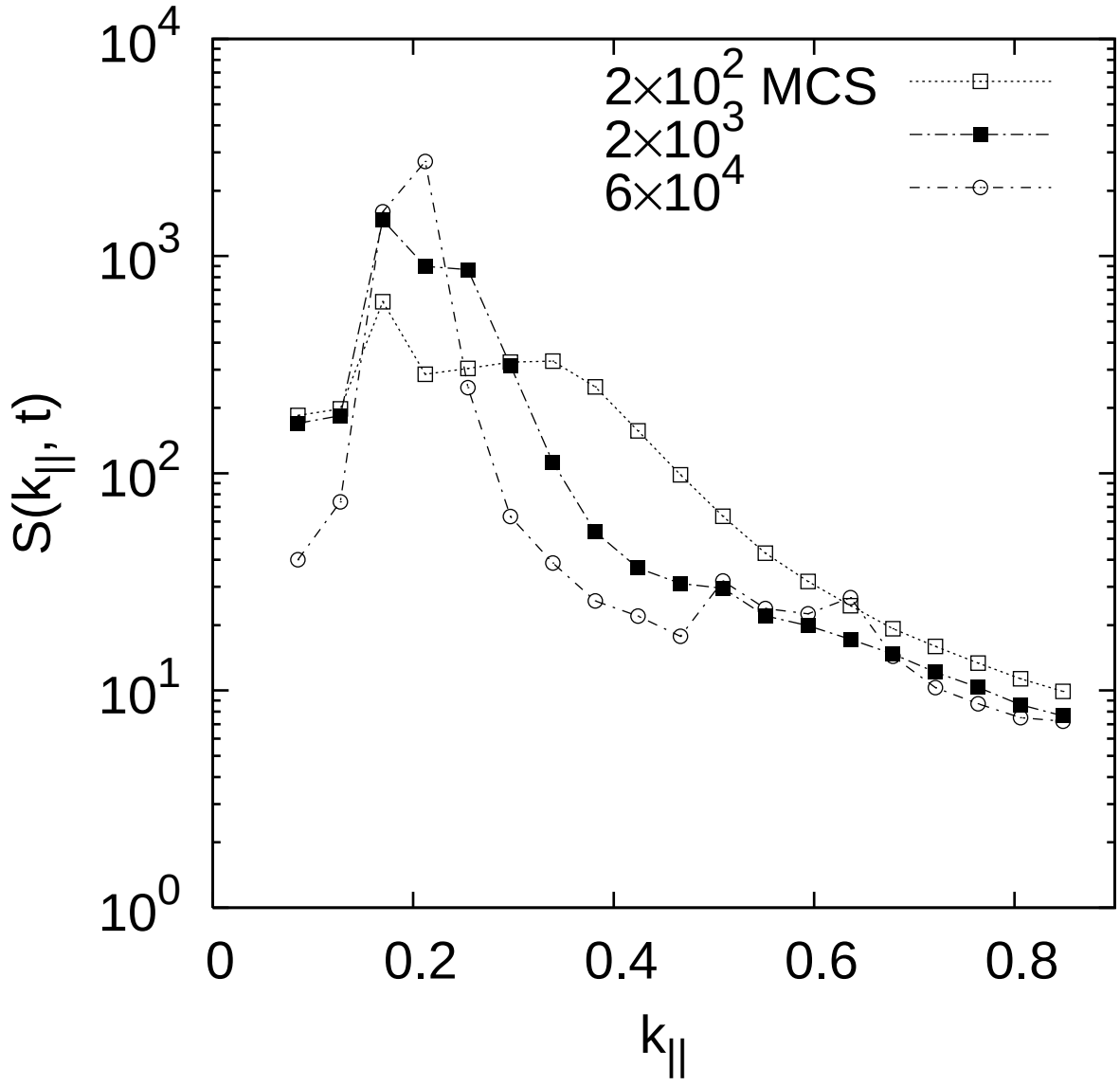

Figure 5.21: Circularly and z-averaged structure factor from the same simulation data as in Fig. 5.20.

One can roughly estimate the depth of the pattern penetration from Fig. 5.20c as a half thickness of the film. There are two separate 3rd-order peaks at $6 \cdot 10^4$ MCS in Fig. 5.21 which suggests strong segregation of A- and B-rich domains near the substrate and the neutral wall. Note that the transient checkerboard structure reflected by two peaks in $S(k_y, z, t)$ at k_p develops further and becomes well pronounced throughout the film at 2000 MCS, Fig. 5.20b.

5.3.3 Incommensurate Systems: $L_p/\lambda = 0.33$ and 0.8

If L_p/λ is too small, for example, in the case of $L_p/\lambda = 0.33$, forming the perpendicular lamellae with the pattern periodicity L_p throughout the entire film would cost too much elastic energy for chains which have to be excessively compressed. Instead, perpendicular lamellae with the

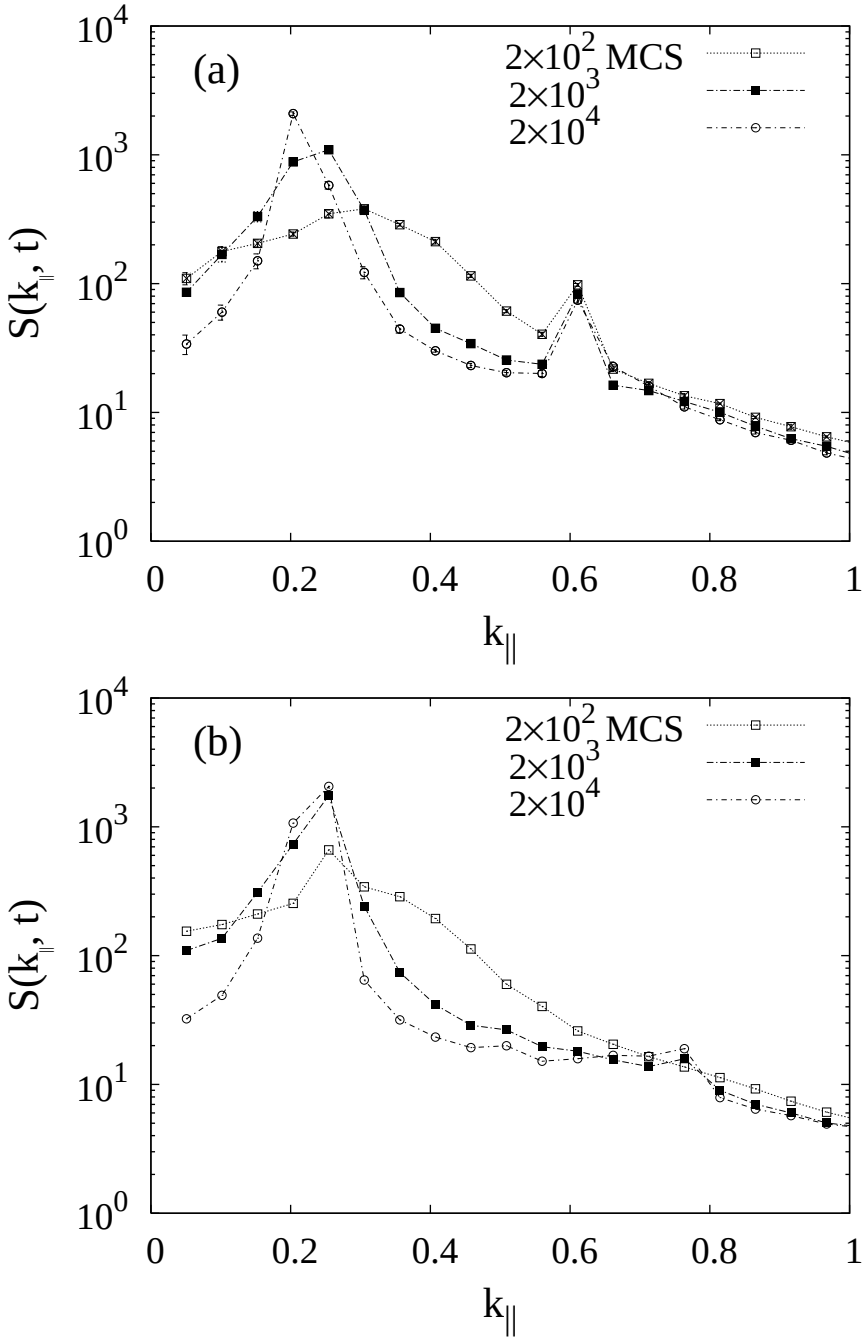

Figure 5.22: Circularly and z-averaged structure factor in incommensurate systems with (a) $L_p/\lambda = 0.33$ and (b) $L_p/\lambda = 0.8$. In both cases the film thickness is λ and lateral dimensions of the film $L_x = L_y = 4\lambda$.

the bulk periodicity λ develop with the lesser cost of the interfacial energy. In this case the patterned substrate acts more like a homogeneous wall repelling the whole molecule, and the diblock copolymers almost ignore the surface pattern.

We show the time evolution of the structure factor $S(k_\parallel, t)$ in the film with $L_p/\lambda = 0.33$ in

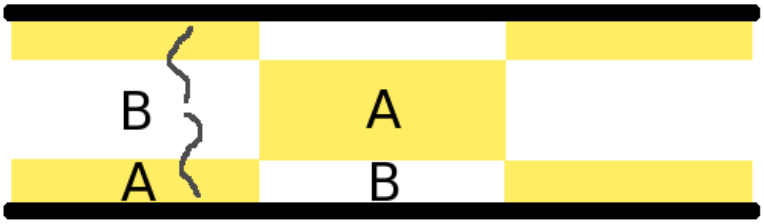

Figure 5.23: The checkerboard structure observed in films with high incommensurability of the substrate pattern. The film thickness $L_z = \lambda$.

Fig. 5.22a (the film thickness $L_z = \lambda$ and the lateral dimensions $L_x = L_y = 4\lambda$). The substrate pattern is seen as a second peak at $k_\parallel = 2\pi/L_p = 0.61$. Whereas the bulk-like ordering reflected by the first broad peak of $S(k_\parallel, t)$ at $t = 200$ MCS develops in time in a manner very similar to the case of neutral walls, see Fig. 5.4, the second peak does not change so that the substrate-induced pattern is hardly preserved in the immediate vicinity of the surface. The structure factor $S(k_y, z, t)$ (not presented here) confirms a well developed perpendicular lamellar structure with the bulk periodicity λ.

Fig. 5.22b presents $S(k_\parallel, t)$ at different times in the film with $L_p/\lambda = 0.8$ (with the same geometry as in the previous case $L_p/\lambda = 0.33$). Here we observe the pattern ordering at the time $t = 200$ MCS (a peak at $k_y = 2\pi/L_p = 0.25$) which develops simultaneously with the bulk-like ordering. At the final time a half of the film is occupied by perpendicular lamellae in register with the substrate pattern (peak at $k_y = 2\pi/L_p = 0.25$ in Fig. 5.22b) whereas the rest of the film consists of perpendicular lamellae with the bulk periodicity visible as a left shoulder of the peak.

5.3.4 Checkerboard Structure in Systems with $L_p/\lambda = 1.5$ and 2.0

We have seen that there exists some limit within which confined lamellae can be stretched or compressed; beyond this limit copolymer molecules change their orientation instead of being excessively stretched or shrunk. If L_p/λ is too large, as for example in the case of $L_p/\lambda = 2.0$, it would cost too much elastic energy for chains to be stretched while orienting parallel to the substrate. Instead, most molecules change their orientation from parallel to perpendicular to the walls, leading to the checkerboard structure near the patterned substrate, see Fig. 5.23. However, perpendicular lamellae can be still preferred at the opposite neutral wall.

Fig. 5.24 shows the time evolution of the structure factor $S(k_y, z, t)$ in the film of thickness $L_z = \lambda$ with $L_p/\lambda = 1.5$ (the lateral dimensions $L_x = L_y = 3L_p$). Two peaks at $k_y = k_p$ at the time $t = 200$ MCS, see Fig. 5.24a, located at $z \simeq R^X = 3.8$ and $z \simeq 11$ with a minimum at $z \simeq 7$ develop in a manner similar to the film with $L_p/\lambda = 1.2$ at the same time, Fig. 5.20a, indicating A-monomer density modulation along the y axis in register with the substrate pattern. The quantity $\langle|\cos\Theta(z,t)|\rangle$ at 200 MCS ploted in Fig. 5.25b has a peak with the magnitude above 0.6 at $z \simeq 7$ and values close to 0.5 in the rest of the film which also indicates one layer of molecules perpendicular to the wall.

As the time proceeds, Fig. 5.24b, the peaks increase in magnitude, the second peak develops

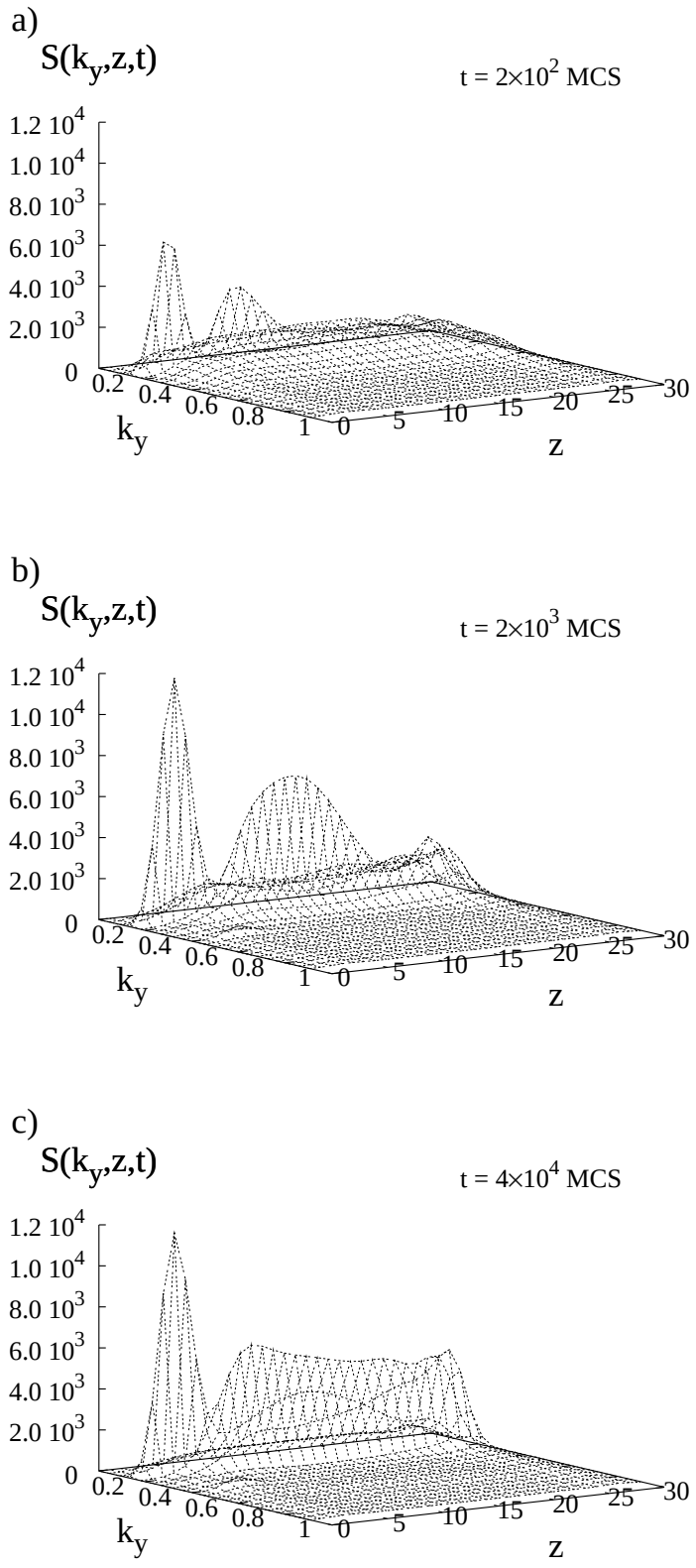

Figure 5.24: Same as Fig. 5.14, but $L_p/\lambda = 1.5$, and $t = 4 \times 10^4$ MCS in (c).

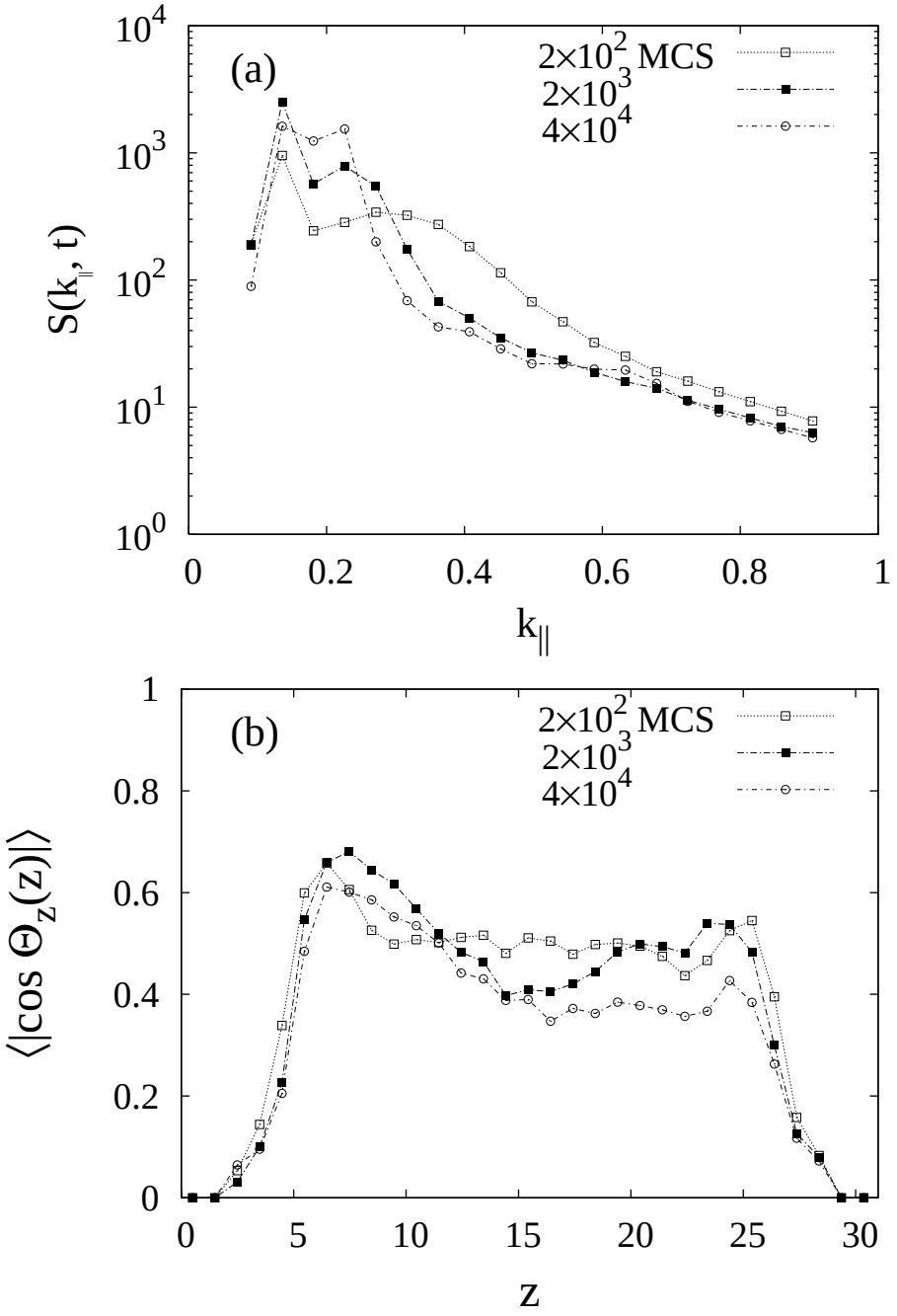

Figure 5.25: (a) Circularly and z-averaged structure factor and (b) $\langle|\cos\Theta(z,t)|\rangle$ from the same simulation data as in Fig. 5.24.

further into the film and gets located at the center of the film. Values of $\langle|\cos\Theta(z,t)|\rangle$ at the substrate become higher and a second peak above 0.5 appears at the neutral wall, see Fig. 5.25b, reflecting a tendency of some molecules at the wall to perpendicular orientation. The same tendency is observed as a small third peak of $S(k_y,z,t)$ at $k_y = k_p$ in the vicinity of the neutral wall, Fig. 5.24b. However, a bulk-like ordering near the neutral wall, visible as a broad peak of

the integrated structure factor $S(k_\parallel, t)$ at 200 MCS in Fig. 5.25a, develops further (2000 MCS) and starts to interfere with the checkerboard structure at the times $t > 2000$ MCS.

As a result, at the final time $t = 4 \cdot 10^4$ MCS, the checkerboard structure is partially destroyed so that the molecules acquire parallel orientation in the interval of z from the neutral wall up to $z \simeq 12$, see Fig. 5.25b, and perpendicular lamellae with the bulk periodicity λ are dominant in that region of the film, see Figs. 5.24c and 5.25a. The molecules at the substrate lose a little their perpendicular orientation, see Fig. 5.25b, $t = 4 \cdot 10^4$ MCS, where the maximum of $\langle|\cos\Theta(z,t)|\rangle$ becomes decreased and shifted closer to the substrate but still maintain the checkerboard structure.

In the film with $L_p/\lambda = 2.0$ (the film thickness $L_z = \lambda$ and the lateral dimensions $L_x = L_y = 2L_p$), one can see quite similar behavior of the quantities $S(k_y, z, t)$, $S(k_\parallel, t)$, and $\langle|\cos\Theta(z,t)|\rangle$ at the early time $t = 200$ MCS, Figs. 5.26a and 5.27. The lower substrate acts locally as an homogeneous A- or B-attractive wall forcing the neighbouring molecules to perpendicular orientation (a peak of $\langle|\cos\Theta(z,t)|\rangle$ in the Fig. 5.25)b and causing a modulation of the A-monomer density in register with the pattern, Fig. 5.26a and 5.27a.

At the time $t = 2000$ MCS the checkerboard structure is well pronounced throughout the entire film; at that time the structure factor $S(k_y, z, t)$, Fig. 5.26b, shows a third peak at the neutral wall ($k_y = k_p$) which has a higher magnitude than that in the prevous case $L_p/\lambda = 1.5$, see Fig. 5.24b. The quantity $\langle|\cos\Theta(z,t)|\rangle$, Fig. 5.27b, also shows two peaks reflecting a perpendicular ordering of the molecules at both the substrate and the opposite wall, the peak at the neutral wall being more pronounced than the same peak in Fig. 5.25b.

The bulk-like ordering close to the neutral wall is also present, visible as a broad peak in the integrated structure factor at the times 200 and 2000 MCS in Fig. 5.27a. This spontaneous ordering interferes with the checkerboard structure in the same way as in the case $L_p/\lambda = 1.5$, forcing molecules near the neutral wall to adopt parallel orientation to form perpendicular lamellae with the periodicity λ at later times $t > 2000$ MCS. This is reflected by some decrease of the peak of $\langle|\cos\Theta(z,t)|\rangle$ at the neutral wall, see Fig. 5.27a ($t = 4 \cdot 10^4$), which is still well pronounced as compared to Fig. 5.25b, and also by a further increase of the second peak of the quantity $S(k_\parallel, t)$ located at $k_y = 2\pi/\lambda$, Fig. 5.25a.

However, the third peak of $S(k_y, z, t)$ at $k_y = k_p$ remains and even increases a little at the neutral wall (Fig. 5.24c) although the minimum between the second and the third peak becomes higher reflecting some distortion of the layer of the checkerboard structure adjacent to the wall.

When the thickness of the film is increased up to $L_z = 1.5\lambda$, we observe quite similar behavior of the integrated structure factor at all the times, see Fig. 5.28a. Although the checkerboard structure is well developed up to $z \simeq 31$, see Fig. 5.28b where the quantity $\langle|\cos\Theta(z,t)|\rangle$ shows two peaks, it cannot force the molecules at the neutral wall to adopt the perpendicular orientation. Istead, they prefer to be oriented parallel to the wall with values of $\langle|\cos\Theta(z,t)|\rangle$ close to 0.4, forming a layer of perpendicular lamellae with the bulk periodicity seen as the second peak of the structure factor in Fig. 5.28a.

It is interesting to note that Wang et al [Wan00b] studied the microphase separation and in particular the incommensurability effects in films with patterned walls by means of Monte Carlo simulations of lattice polymers. They also reported the checkerboard structure when the incommensurability becomes large $L_p/\lambda = 1.5$ and 2.0. However, they were interested in the equilibrated structures and paid no attention to the pattern transfer kinetics.

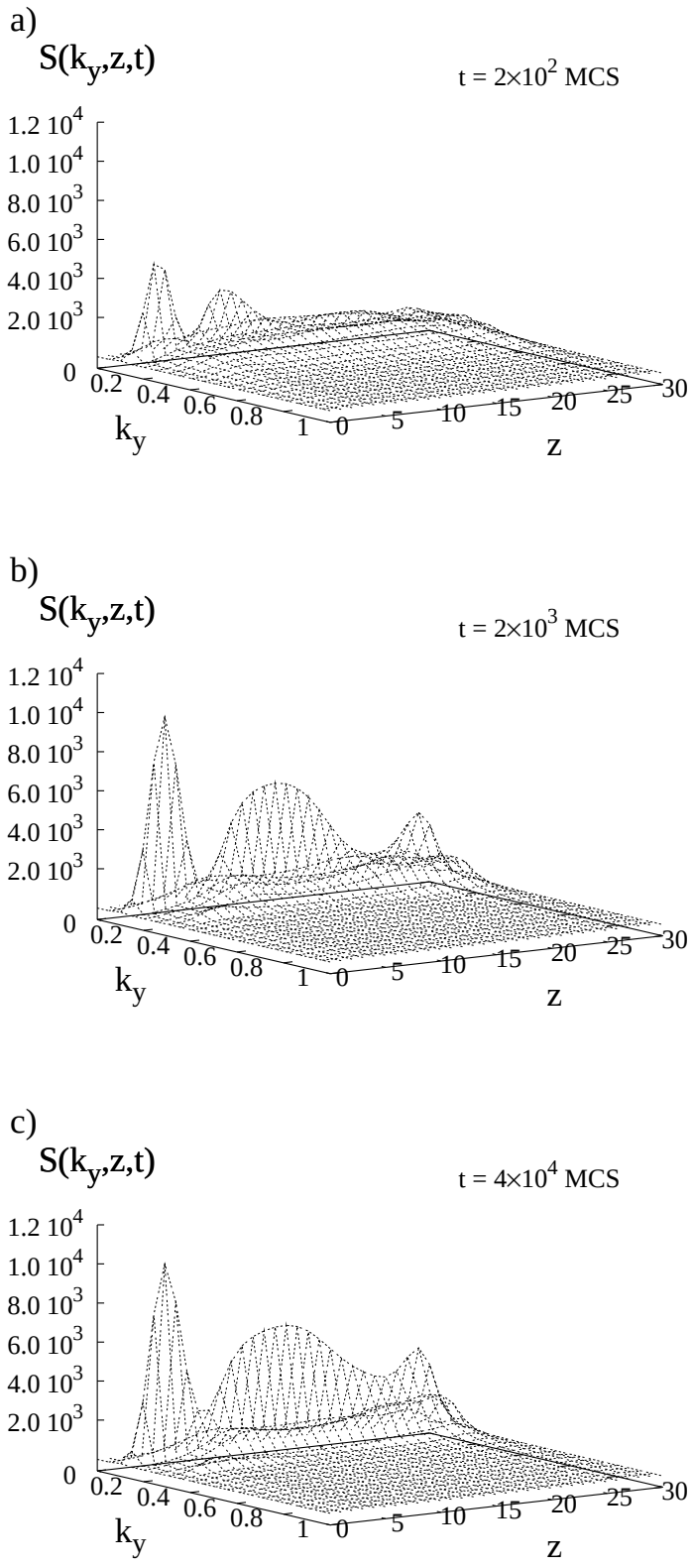

Figure 5.26: Same as Fig. 5.14, but $L_p/\lambda = 2.0$, and $t = 4 \times 10^4$ MCS in (c).

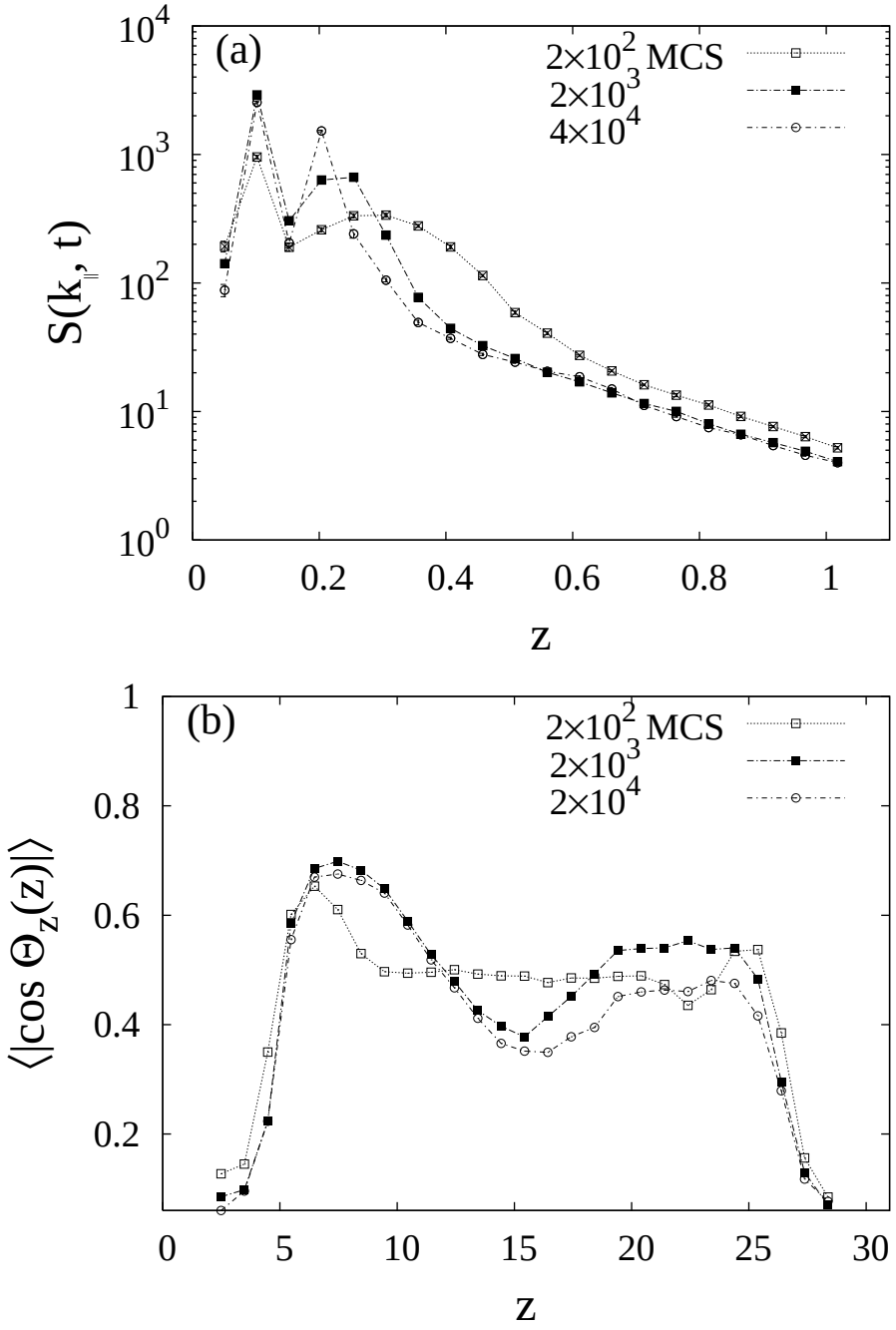

Figure 5.27: (a) Circularly and z-averaged structure factor and (b) $\langle|\cos\Theta(z,t)|\rangle$ from the same simulation data as in Fig. 5.26.

5.4 Summary

In this section we studied the microphase separation in thin films of diblock copolymers. When the walls of the film are homogeneous and neutral, the perpendicular lamellar phase with the bulk period λ and a local order developes due to parallel alignment of molecules at the walls. If

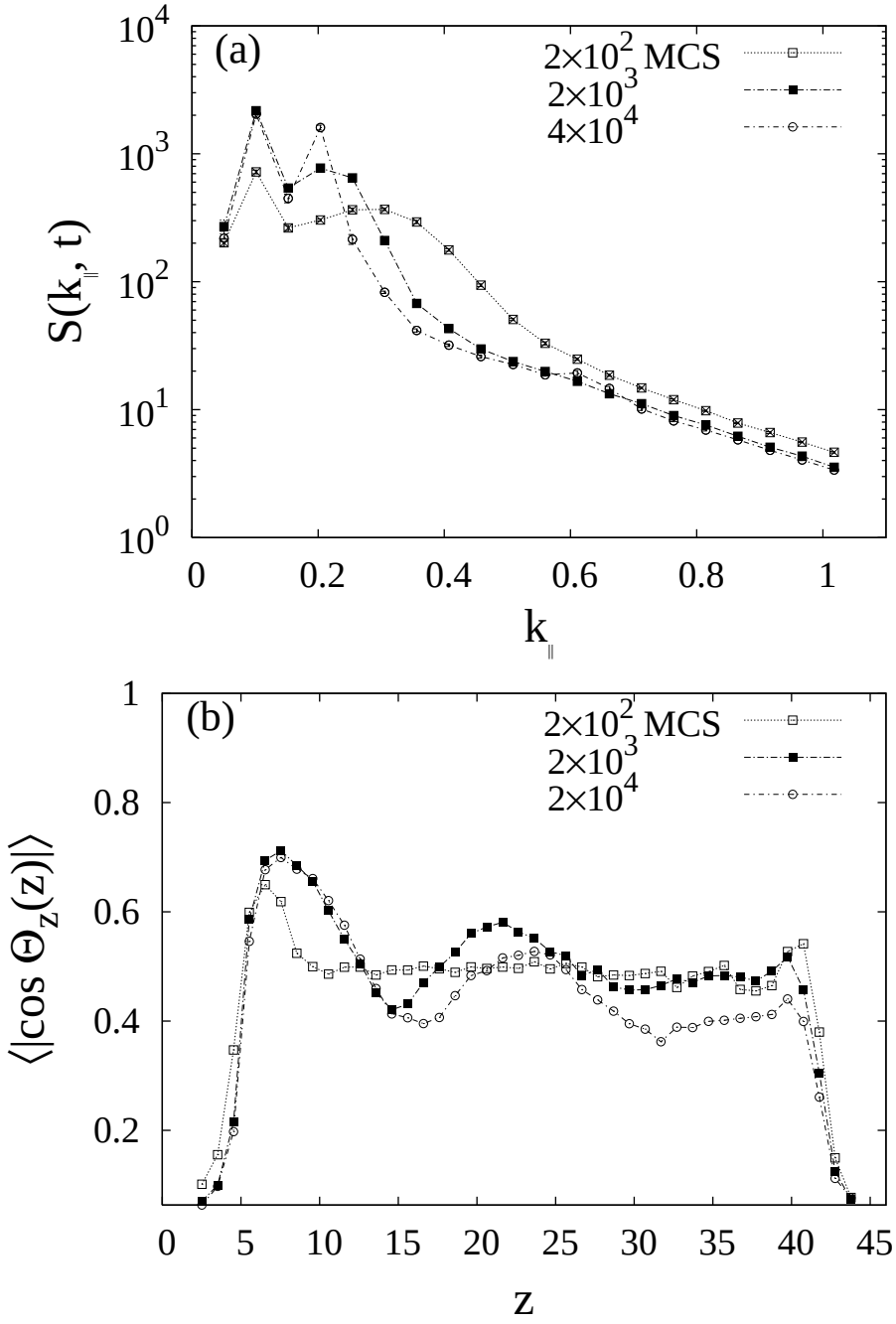

Figure 5.28: Same as in Fig. 5.27 but in the film of thickness $L_z = 1.5\lambda$.

one or both of the walls are made attractive to one component of the molecules, the microphase separation leads to parallel lamellae with global order.

To obtain globally ordered perpendicular lamellae, we patterned one of the walls with periodically alternating A and B-attractive stripes with the period $L_p = \lambda$. If the pattern periodicity differs from λ, bulk-like ordering away from the substrate occurs leading to a mixed structure which consists of perpendicular lamellae with the period L_p near the substrate and perpen-

dicular lamellae with the bulk period λ in the rest of the film. The checkerboard structure is observed in films with large incommensurability $L_p/\lambda = 1.5$ and 2.0. The kinetics of the pattern transfer and its interference with the bulk-like ordering was studied with the help of the time dependent structure factor.

6 Diffusion through Polymer Networks: Dynamic Percolation Approach

The primary goal of this section is to describe diffusion of a tracer particle in a dynamically disordered polymer network. As explained in the introduction (Section 1.9), this is a fundamental problem in understanding ion transport in polymer electrolytes. The tracer motion is intrinsically related to the random reorganisations of the host medium which occur on the same time scale as the atomic hopping which makes direct study a very complicated task. One approach to understanding of the dynamic-disorder transport was proposed by Druger [Dru85] within the dynamic percolation (DP) theory which generalizes the well-known problem of a random walk in a frozen percolating network to networks undergoing temporal renewals. Druger assumed the renewal behavior of the host medium to obey Poisson statistics with the renewal rate λ regarded as a phenomenological parameter.

Subsequently, this theory was generalized to include temporal correlations between renewals through some waiting time distribution $\psi(t)$ [Dru88]. This aspect of non-Poisson renewals turned out to be essential when considering tracer diffusion through a fluctuating polymer network as a DP-process [Dür02], as the polymer chain motion is characterized by a wide range of relaxation times (see for example the Rouse model described in Section 1.2). In an attempt to apply that formalism [Dru88] to polymer electrolytes, Duerr et al. designed a way how to derive $\psi(t)$ from polymer chain density fluctuations near a fixed tracer atom. In comparison with Monte Carlo simulations based on the Verdier-Stockmayer algorithm, they showed that the DP theory reproduces with a good quantitative agreement the tracer diffusion in systems up to moderate polymer densities. To test the theory against dense systems we employ here the fluctuation site-bond (FSB) algorithm developed recently [Schu05].

The structure of this section is two-fold. First, we present detailed simulation results for tracer diffusion in an athermal system of lattice chains, with emphasis on high densities [Kar06]. Second, we discuss the applicability of the additional coarse-graining step based on the DP theory, and compare both methods. In Section 6.1 we describe our model and review very briefly the FSB algorithm. In turn we discuss explicit results for tracer diffusion of point-like particles embedded in the polymer matrix. Section 6.2 explains our procedure to extract from polymer dynamics the waiting time distribution $\psi(t)$, which is used as input for the DP-model. Tracer correlation factors and the dynamic diffusivity are then calculated and compared with full simulations. Results are summarized and discussed in Section 6.3.

6.1 Model and Kinetic Monte Carlo Simulation

In distinction to the standard Verdier-Stockmayer [Ver62] and bond fluctuation method [Bin95] for lattice chains, we employ here the fluctuation site-bond algorithm that has been developed

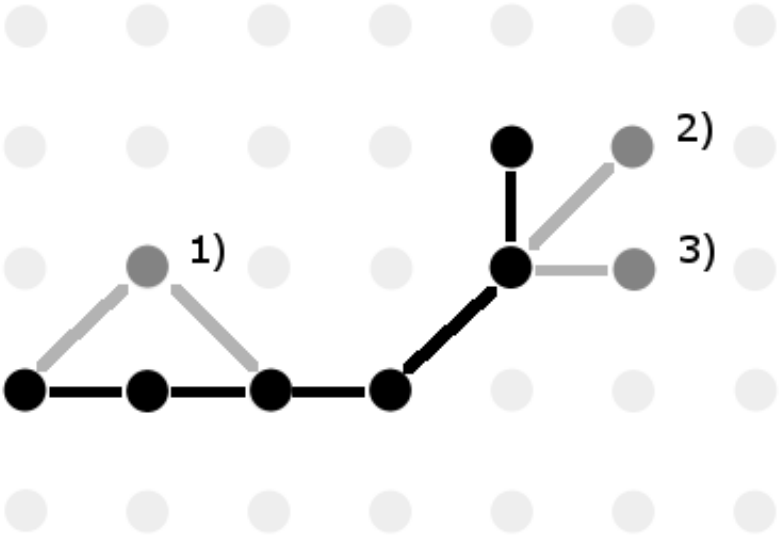

Figure 6.1: Possible moves in the fluctuation site-bond (FSB) algorithm [Schu05] used in simulations. Light circles are vacant sites of the underlying simple cubic lattice whereas sites occupied by the chain beads are depicted by black circles connected by black bonds. The bond length can be equal to 1 and $\sqrt{2}$. Three possible moves are shown as grey circles connected by grey links with the neighboring beads: in moves 1) and 2), the successive beads are connected by second–neighbor lattice bonds of the lattice and in 3) the link lies on the nearest-neighbor bond of the lattice.

recently [Schu05]. Polymer chains are built of beads that occupy the sites of a $d = 3$-dimensional simple-cubic substrate lattice of unit spacing. Successive beads are connected either by nearest-neighbor or second-neighbor lattice bonds with bond lengths 1 and $\sqrt{2}$, respectively. A bead can move along a nearest-neighbor bond, provided the target site is vacant and the move does not violate bond restrictions. Possible moves of the FSB algorithm are presented in Fig. 6.1 for the 2–d case. Actually, the algorithm can be based on bead or vacancy moves. In the case of vacancy moves, advantageous at high densities, an elementary step consists of an attempted exchange of a randomly selected vacancy with a nearest-neighbor bead; the move is accepted if it conforms with bond restrictions for that bead. These rules enable us to equilibrate systems with a concentration c of occupied sites up to $c \sim 0.95$.

The time in the vacancy based simulations scales with that of the simulations based on bead moves as follows. When moving the vacancies, one MCS consists of N_v attempts, where N_v is the number of vacancies in the simulation box. In the opposite case of moving the beads, one MCS consists of N_b attempts with N_b being the total number of beads. However, in the case of the bead moves, all the beads which neighbor the vacancies will on average be attempted and so one MCS would lead on average exactly to the same number of particle moves as when moving the vacancies. Because of this, one MCS with attempting beads is equivalent to one MCS with attempting vacancies, and the time is the same in both types of simulation.

Ergodicity of this algorithm has been demonstrated in three and even in two dimensions.

For details on the equilibration and subsequent equilibrium chain dynamics we refer to the original work [Schu05]. To the system of chains of common length (number of beads $r \geq 2$) we add tracer particles which perform nearest-neighbor hops among the lattice sites. Hard core interactions among beads and tracers are taken into account by the standard site exclusion principle (Fermionic lattice gas). Allowed exchange processes of a vacancy with a nearest-neighbor occupied site have constant a priori probability, independent of whether the exchange is with a tracer or a polymer bead. Typically we consider systems of linear size $L = 21$ with periodic boundary conditions, containing a variable number M of chains so that $c \simeq Mr/L^3$. For the concentration of tracer particles we use a small value $c_t < 10^{-2}$ so that tracer atoms move independently from each other.

As usual, the frequency-dependent tracer diffusivity is given by the Laplace transform of the mean-square displacement according to

$$\hat{D}(s) = \frac{s^2}{6} \int_0^\infty dt e^{-st} \left\langle r^2(t) \right\rangle \,, \tag{6.1}$$

with $s = -i\omega + 0^+$, and the long-time diffusion constant D is obtained from (6.1) in the limit $\omega \to 0$. It is convenient to separate in the result for D the average effect of site blocking by a factor $1 - c$, so that we write

$$D = D_0 \, (1 - c) \, f(c, r) \,. \tag{6.2}$$

This defines the tracer correlation factor $f(c, r)$ which will depend also on the chain length r. D_0 denotes the diffusion constant of a tracer in an otherwise empty lattice: $D_0 = \Gamma a^2$, with $\Gamma = 1/6$ being the bare hopping rate in the simple cubic lattice and $a = 1$ the lattice constant. Note that irrespective of the chain connectivity the short-time diffusion constant is simply given by $D_0(1 - c)$.

Using the algorithm described above, simulations of the full system [Kar06] yield correlation factors f as displayed in Fig. 6.2. Different sets of data points refer to different chain lengths r. The special case $r = 1$ corresponds to a system with nonconnected beads, which is identical to the conventional hard-core lattice gas of point-like particles. In that case f is given to a high degree of accuracy by the approximate expression, see [Nak80], [Tah83], and [Die85]:

$$f(c, 1) = \frac{1 + \langle cos\theta \rangle}{1 - [(3c - 2)/(2 - c)] \, \langle cos\theta \rangle} \,, \tag{6.3}$$

with $\langle cos\theta \rangle$ characterizing the average directional change in two consecutive steps of the tracer due to the presence of one bead. For a simple-cubic lattice $\langle cos\theta \rangle = -0.209$. This expression is represented in the figure by the continuous line. In distinction to calculations with the Verdier-Stockmayer algorithm [Ver62], data sets for dimers ($r = 2$) and chains up to a length $r = 20$ always fall below the case $r = 1$, but show a smooth approach to the continuous line as $c \to 0$. On the contrary, going to high densities, $f(c, r)$ markedly drops down, especially for the longer chains. When $r = 10$ or larger, we find values significantly smaller than 0.1 for densities $c \geq 0.9$. Note that we do not expect the correlation factor to vanish as long as $c < 1$. On account of $D/\hat{D}(\infty) = f$, the above results indicate significant dispersion in the frequency-dependent diffusivity. For a discussion of dynamic diffusion, we introduce the time-dependent diffusion constant $D(t) = \langle r^2(t) \rangle / 6t$ with $D = \lim_{t \to \infty} D(t)$. As shown in Fig. 6.3, an extended transient regime between short-time and long-time diffusion indeed

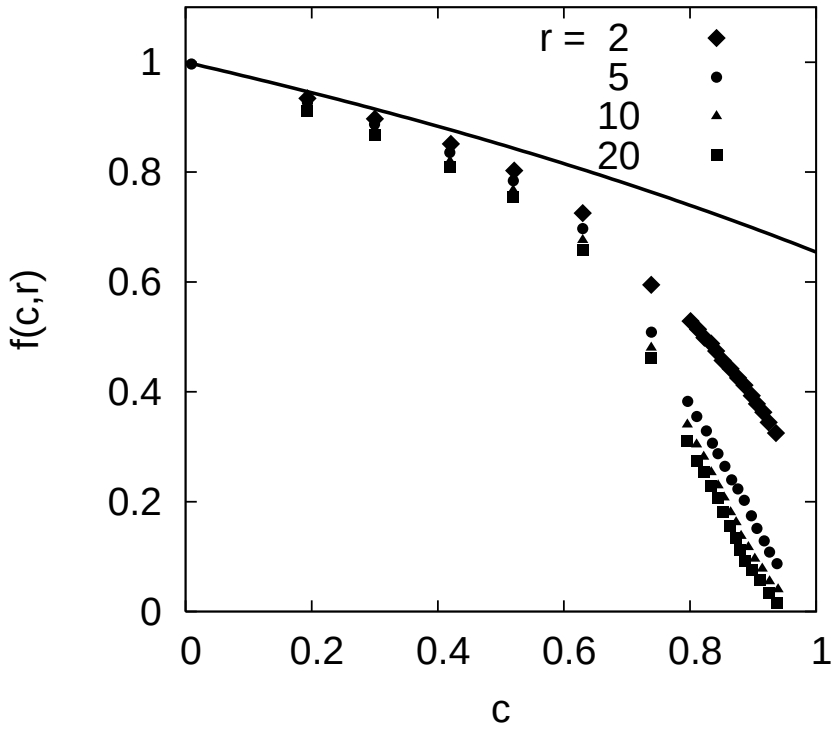

Figure 6.2: Simulated tracer correlation factor f versus concentration c for different chain lengths $r = 2, 5, 10$ and 20. For comparison we also show by the full line the correlaton factor of the hard core lattice gas ($r = 1$) according to Eq. (6.3) (after [Kar06]).

develops at high concentrations, characterized by effective power-laws $D(t) - D \sim t^{-p}$. The exponent p seems to be nearly c-independent and has values $p \sim 0.5$, with a slight tendency to decrease for the longer chains. Thus it appears from Fig. 6.3 that slow chain dynamics in the high concentration range induces features of anomalous tracer diffusion before $D(t)$ reaches its asymptotic long-time limit.

6.2 Dynamic Percolation Concept

The DP-model introduced by Druger and coworkers [Dru85], [Dru88] deals with a random walk of a tracer in a percolative environment, where disorder configurations seen by the tracer as opened and blocked sites of the lattice are globally renewed in time according to some waiting time distribution $\psi(t)$. Configurations before and after a renewal event are uncorrelated. It was shown that the actual type of disorder enters only via the mean-square displacement $\langle r^2(t)\rangle_0$ in the absence of renewals [Dru88]. The second basic input quantity is the distribution $\psi(t)$. Except for the $\omega \to 0$ limit it appears that the general results for $\hat{D}(\omega)$ derived in [Dru88] have hardly been exploited in the literature [Zon01]. For symmetric jump rates of the walker, $\hat{D}(\omega)$

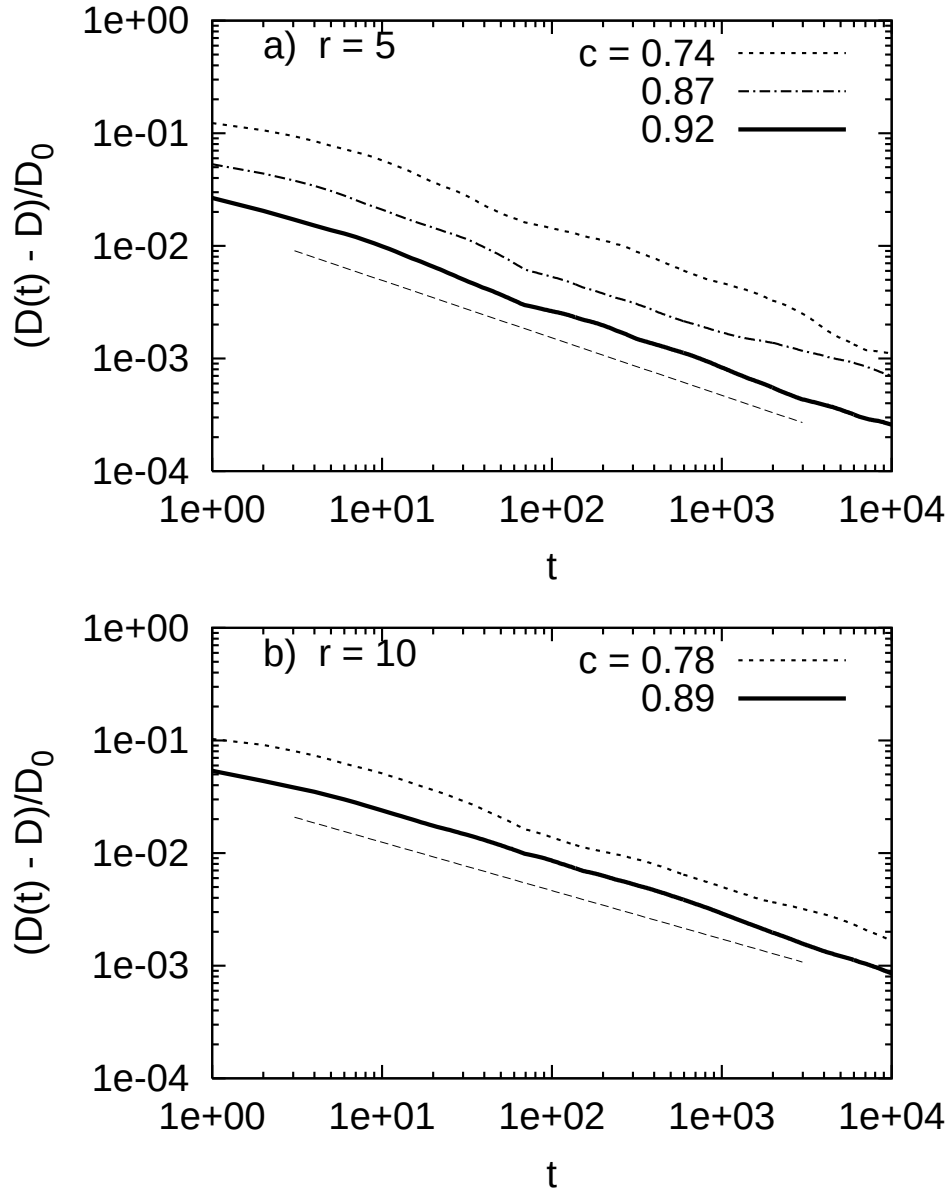

Figure 6.3: Double-logarithmic plot of $D(t) - D$ versus time for different concentrations: (a) $r = 5$; (b) $r = 10$. The dashed straight lines have slopes $p = 0.51(a)$, and $p = 0.45(b)$ (after [Kar06]).

can be written in the form

$$\hat{D}(\omega) = \frac{1}{6} \int_0^\infty dt e^{i\omega t} \left\langle r^2(t) \right\rangle_0 \left(\frac{d}{dt} + i\omega \right)^2 \Phi(t) \,, \tag{6.4}$$

where $\Phi(t)$ denotes the unconditioned probability that no renewal occurs in the time interval $[0, t]$.

We define through $\phi(t)$ the probability density for the first renewal event to take place at

time $t > 0$. Then the probability $\Phi(t)$ for no renewal in $[0, t]$ is connected with $\phi(t)$ through

$$\Phi(t) = 1 - \int_0^t dt' \phi(t') \,. \tag{6.5}$$

Following Refs. [Dru88] and [Fel68] that

$$-\frac{d\phi}{dt} = \lambda \psi(t) \,, \tag{6.6}$$

where $\lambda^{-1} = \int_0^\infty dt\, t\psi(t)$ is the mean time between two consecutive renewals, we relate the function $\Phi(t)$ to the waiting time distribution $\psi(t)$ by

$$\psi(t) = \lambda^{-1} \frac{d^2\Phi(t)}{dt^2} \,. \tag{6.7}$$

As $\omega \to 0$ in (6.4) one obtains for the diffusion constant

$$D = \frac{\lambda}{6} \int_0^\infty dt \left\langle r^2(t) \right\rangle_0 \psi(t) \,. \tag{6.8}$$

Eq. (6.8) expresses the main idea of the DP-model that the study of the complicated motion of the tracer in dynamically disordered enviroment can be divided into two much simpler tasks of the mean square displacement of the walking tracer in a frozen network $\langle r^2(t)\rangle_0$ and the statistical nature of the structural reorganizations of the host medium which, as shown below, yields the quantity $\psi(t)$.

For illustration, consider the example of Poisson-type renewals described by $\Phi(t) = e^{-\lambda t}$, in a lattice system with a high concentration of blocked sites, such that sites accessible to the walker do not percolate so that its motion is restricted to some limited volume of the system. Assuming that the mean square displacement of the walker obeys $\langle r^2(t)\rangle_0 = r_0^2(1-e^{-\gamma t})$, where γ is a rate constant for the approach to saturation at long times and r_0 is the linear size of the volume accessible to the walker, we obtain from (6.4)

$$\hat{D}(\omega) = \frac{r_0^2}{6}\gamma \left(1 - \frac{\gamma}{\lambda + \gamma - i\omega}\right) \tag{6.9}$$

with its zero frequency limit $D = (r_0^2/6)\lambda\gamma/(\lambda+\gamma)$. Eq. (6.9) shows that the frequency scale for dispersive transport is given by a combination of the rate constants λ and γ.

In our actual case of particle diffusion through a dense polymer network we expect that both quantities $\langle r^2(t)\rangle_0$ and $\Phi(t)$ are governed by broad spectra of relaxation rates. A combination of the two spectra will then enter $\hat{D}(\omega)$, as suggested by the form of Eq. (6.9). The end result for $\hat{D}(\omega)$ obtained with the help of (6.14) and (6.15) is given by Eq. (6.16).

To implement the DP approach to the tracer particle diffusion in our lattice chain model, one has to find out how to extract the waiting time distribution $\psi(t)$ from the model dynamics. Following Dürr [Dür02], we note first that the quantity $\psi(t)$ governs local renewal behaviour of the temporal distribution of pathway openings and closings seen by a fixed tracer. Such behaviour is reflected by the occupation correlation function $\langle n_i(t)n_i(0)\rangle$ of a site i adjacent to the fixed tracer. One can write

$$\langle n_i(t)n_i(0)\rangle = \Phi(t)\,\langle n_i(t)n_i(0)\rangle + (1-\Phi(t))\,\langle n_i(t)n_i(0)\rangle \,. \tag{6.10}$$

The first term in (6.10) can be thought of as accounting for the case when with the probability $\Phi(t)$, the system undergoes no renewal during the interval $[0,t]$. The occupation $n_i(t)$ remains the same as at the initial time $t=0$ and $n_i(t)n_i(0) = (n_i(0))^2 = n_i(0)$ because $n_i(t) = 0$ or 1. Then, the second term reflects the situation where with probability $1-\Phi(t)$, one or more renewals happen within $[0,t]$. The occupations $n_i(t)$ and $n_i(0)$ become uncorrelated so that $\langle n_i(t)n_i(0)\rangle = \langle n_i(t)\rangle \langle n_i(0)\rangle = c^2$.

Combining these results, we rewrite (6.10) as

$$\langle n_i(t)n_i(0)\rangle = c\,[\Phi(t) + c\,(1-\Phi(t))] \tag{6.11}$$

or finally

$$\Phi(t) = \frac{\langle n_i(t)n_i(0)\rangle - c^2}{c(1-c)}\,. \tag{6.12}$$

Obviously, at the initial time $t=0\,,\ n_i(0)n_i(0) = 1$ if the site is occupated and 0 otherwise which makes $\langle n_i(0)n_i(0)\rangle = c$ and $\Phi(t)|_{t=0} = 1$ (the possibility for two simultanuous renewals is 0). At large times $t\to\infty$, $n_i(t)$ and $n_i(0)$ become uncorrelated $\langle n_i(t)n_i(0)\rangle = \langle n_i(t)\rangle \langle n_i(0)\rangle = c^2$ so that $\Phi(t) = 0$.

With the help of (6.7), (6.12), the waiting time distribution becomes

$$\psi(t) = [\lambda c(1-c)]^{-1}\,\frac{d^2}{dt^2}\,\langle n_i(t)n_i(0)\rangle\ . \tag{6.13}$$

Note that after inserting of (6.13) into Eq. (6.8) the prefactor $[\lambda c(1-c)]^{-1}$ drops out.

For a quantitative evaluation of Eqs. (6.4) and (6.8) in our polymer model two complementary simulations are necessary. The first is straightforward simulation of the tracer motion when chains are frozen, which yields $\langle r^2(t)\rangle_0$. Second, chain motions have to be mapped onto renewal events in the DP-model according to Eq. (6.13). Fig. 6.4 shows functions $\Phi(t)$, see Eq. (6.12), for different chain lengths r at the concentration $c = 0.84$, which lies significantly above the r-dependent percolation threshold of frozen chains [Dür02]. Successively slower, highly non-exponential decay behaviors are observed upon increasing r. When applying the DP-concept to diffusion through a fluctuating polymer matrix it is therefore essential to take into account the non-Poisson character of renewals.

In order to perform the integration in (6.4), simulation data for $\Phi(t)$ were fitted in terms of a sum of N exponentials

$$\Phi(t) = \sum_{j=1}^{N} a_j \exp(-\lambda_j t)\,, \tag{6.14}$$

where a_j and the relaxation times λ_j are to be found from the fit. The constants a_j obey a normalization condition at $t=0$ that $\sum_{j=1}^{N} a_j = 1$. In Fig. 6.5 we plot the distribution function $\Phi(t)$ for the chain length $r = 10$ and at the concentration $c = 0.84$ fitted with Eq. (6.14) in the time interval $[0, 1000]$ with $N = 1, 2, 3$ and 4 (for convenience the interval $[0, 100]$ is only shown). As seen, the four exponential fit very nicely reproduces the simulation data. Similar fits performed for other chain lengths and monomer concentrations also found the four exponential fit to be in nice agreement with the simulation data.

In Fig. 6.6 we show the function $\Phi(t)$ for the chain length $r = 10$ and various concentrations of the beads c . As in [Dür02], we observe a non-monotonous character in the dependence of $\Phi(t)$

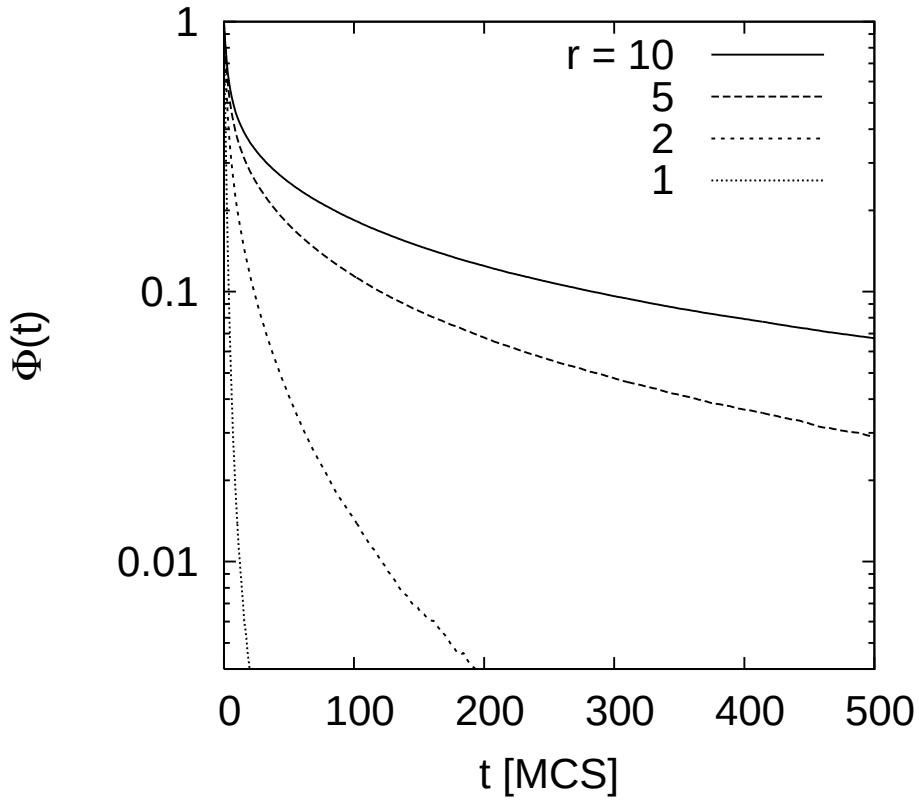

Figure 6.4: The probability $\Phi(t)$ for no renewal event within the time interval $[0, 1]$ for different chain lengths r at a concentration $c = 0.84$. The data are obtained by simulating the occupation correlation function $\langle n_i(t)n_i(0)\rangle$ of a site i next to the fixed tracer, see Eq. (6.12) (after [Kar06]).

on c. Going from lower to higher concentrations, $\Phi(t)$ has a faster relaxation at intermediate concentrations (about 0.4) but slows down further towards high densities, see the case $c = 0.84$ in the figure. As in [Dür02], we connect this non-monotonous behavior to the fact that at intermediate concentrations the monomer density as seen from the tracer is homogeneous and therefore suppresses large fluctuations.

In Fig. 6.7 the mean square displacement $\langle r^2(t)\rangle_0$ of a tracer in a frozen environment of chains with the length $r = 10$ is plotted at different concentrations of beads. The quantity $\langle r^2(t)\rangle_0$ shows a crossover from diffusive behavior at dilute concentrations where $\lim_{t\to\infty}\langle r^2(t)\rangle_0 = 6Dt$ ($c = 0.09$ in the figure) to a localized random walk in dense systems where $\lim_{t\to\infty}\langle r^2(t)\rangle_0 = r_0^2$ ($c = 0.84$). An estimation of the chain length dependent critical concentrations c_{crit} of monomer percolation within a system of frozen chains is beyond the scope of this study. In [Dür02], c_{crit} was estimated for various chain lengths and shown to increase with r. $\langle r^2(t)\rangle_0$ is also plotted in Fig. 6.7 for hard core gas $r = 1$ at $c = 0.41$ and is found to be very similar to $\langle r^2(t)\rangle_0$ of the system $r = 10$ at the same concentration.

We fit the mean square displacement in dense systems $c > c_{crit}$ with a sum of M exponentials:

$$\left\langle r^2(t)\right\rangle_0 = \sum_{k=1}^{M} r_k^2\left(1 - \exp(-\gamma_k t)\right) , \tag{6.15}$$

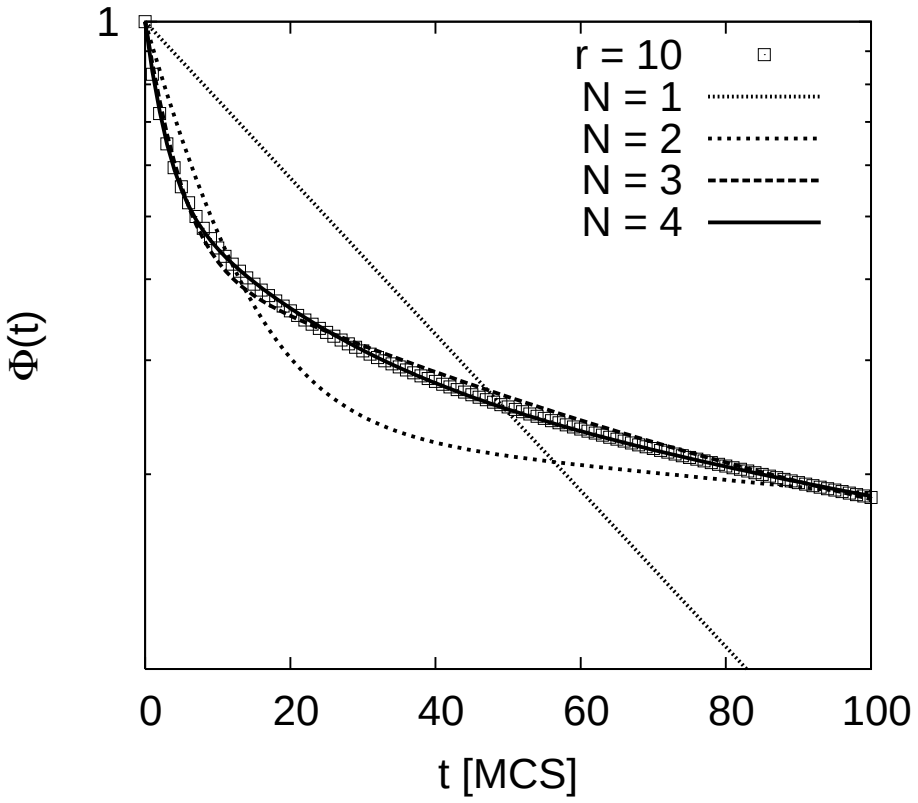

Figure 6.5: The probability for no renewal $\Phi(t)$ calculated with Eq. (6.12) (squares) and exponential fits (6.14) to the data with $N = 1, 2, 3$, and 4 for the chain length $r = 10$ at a concentration $c = 0.84$. The four exponential fit is seen to best represent the simulation results (after [Kar06]).

where r_k^2 and relaxation rates γ_k are fitting parameters.

$M = 3$ exponentials are sufficient in all cases studied in this work as seen from the perfect agreement with the data shown in Fig. 6.8 for the chain length $r = 10$ and $c = 0.84$. The curve perfectly fits the data so that one cannot distinguish between them and therefore (6.15) can be used in Eq. (6.4) to numerically evaluate the frequency-dependent tracer diffusivity in dynamically-disordered host. With the help of (6.14) and (6.15), (6.4) reads

$$\hat{D}(\omega) = \frac{1}{6} \sum_{j,k} a_j r_k^2 \left[\gamma_k - \frac{\gamma_k^2}{\lambda_j + \gamma_k} \, \frac{1}{1 - i\omega(\lambda_j + \gamma_k)^{-1}} \right] \tag{6.16}$$

or

$$\hat{D}(\omega) = \hat{D}(\infty) + \sum_{j,k} \frac{D - \hat{D}(\infty)}{1 - i\omega\tau_{jk}} \,, \tag{6.17}$$

where $\tau_{jk} = (\lambda_j + \gamma_k)^{-1}$ ($j = 1, ..., 4$ and $k = 1, ..., 3$) are the relaxation times of the diffusivity, $D \equiv \hat{D}(0) = 1/6 \sum_{j,k} a_j r_k^2 \lambda_j \gamma_k / (\lambda_j + \gamma_k)$ is the long-time diffusivity, and $\hat{D}(\infty) = 1/6 \sum_{j,k} a_j r_k^2 \gamma_k$ is the diffusion constant at initial times. (6.16) is a non-Poisson analog of the Eq. (6.9).

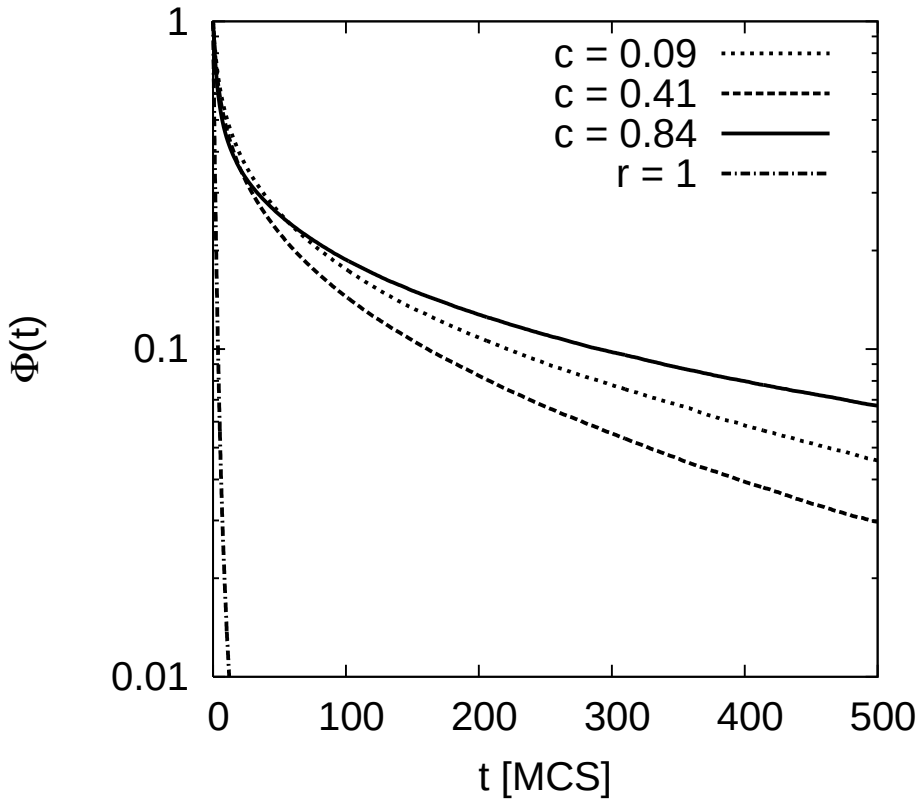

Figure 6.6: Function $\Phi(t)$, see Eq. (6.12) for the chain length $r = 10$ at three concentrations $c = 0.09, 0.41$, and 0.84 . Also the c-independent $\Phi(t)$ is shown for hard-core lattice gas ($r = 1$) (after [Kar06]).

The real part of 6.17 gives

$$Re\hat{D}(\omega) = \hat{D}(\infty) + \sum_{j,k} \frac{D - \hat{D}(\infty)}{1 + \omega^2 \tau_{jk}^2} \,. \tag{6.18}$$

The following fit was used for the mean-square displacement in dilute systems with $c < c_{crit}$:

$$\left\langle r^2(t) \right\rangle_0 = r_1^2 \left(1 - \exp(-\gamma t)\right) + r_2^2 t \,, \tag{6.19}$$

which reproduces the diffusive behaviour at long times.

Concentration-dependent correlation factors obtained from Eq. (6.2) and the $\omega = 0$ limit of (6.4) using the fits (6.14), (6.15) or (6.19) are plotted in Fig. 6.9. While there is quantitative agreement with Eq. (6.3) in the case $r = 1$, only resonable agreement with the full simulation data in Fig. 6.2 is observed up to moderate densities for $r > 1$. There is a strong systematic deviation from the full simulation data at densities close to 1, where the drop in $f(c)$ with increasing c is less pronounced than that in Fig. 6.2.

We argue that the deviations between full and DP-simulations at higher c may be due to the following facts.

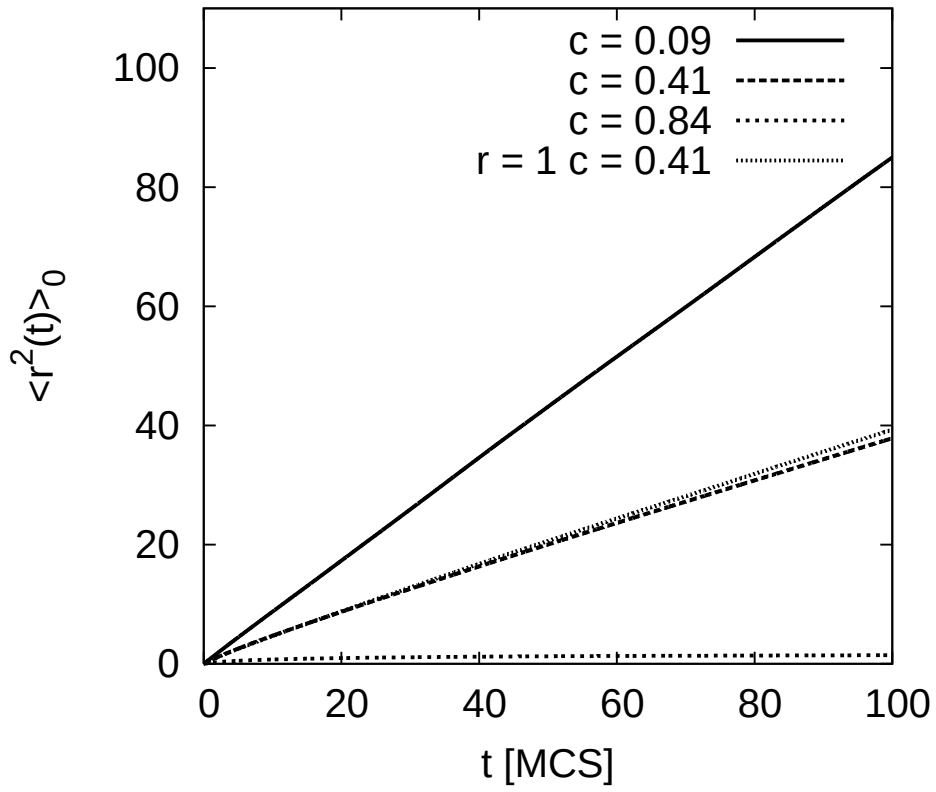

Figure 6.7: Mean square displacement $\langle r^2(t)\rangle_0$ of a tracer in a frozen network of chains with the length $r = 10$. Monomer concentrations are as in Fig. 6.6. For $c = 0.41$ a comparison is made with the case $r = 1$ (after [Kar06]).

i) In mapping the model dynamics onto the DP-approach, see (6.12), the renewal dynamics of the pathway openings and closings as seen by the fixed tracer is not fully reflected by considering the first nearest-neighbor shell. In Fig. 6.10, the tracer initially located at the site a, may hop over to the site b belonging to the second nearest-neighbor shell. When we consider the renewal events in the first nearest-neighbor shell only, we assume that the sites of the second shell are not occupied. Obviuosly, the effect of the second shell becomes enhanced at higher densities c. The values of the correlation factor calculated within Eq. (6.12) might get decreased when taking into account the renewal dynamics of the second shell.

ii) The site occupations of the first nearest-neighbor shell around the fixed tracer are assumed to be uncorrelated. While this assumption is true to some degree in the model based on the Verdier-Stockmayer algorithm of [Dür02], it obviously gets broken in our chain model using the FSB method, where the chain links are of two types $(0, 0, 1)$ and $(0, 1, 1)$, see Fig. 6.10. In the figure, the occupation of the site 2 gets strongly correlated with that of the site 1 when there are two adjacent beads of the same chain located on these sites.

Larger values of the correlation factor at higher densities means that there is less dispersion in the frequency-dependent diffusivity $D(\omega) = \lim_{\epsilon\to 0} Re\hat{D}(-i\omega + \epsilon)$ calculated from Eq. (6.4) when compared with full simulations. Nevertheless, Fig. 6.11 display an intermediate regime,

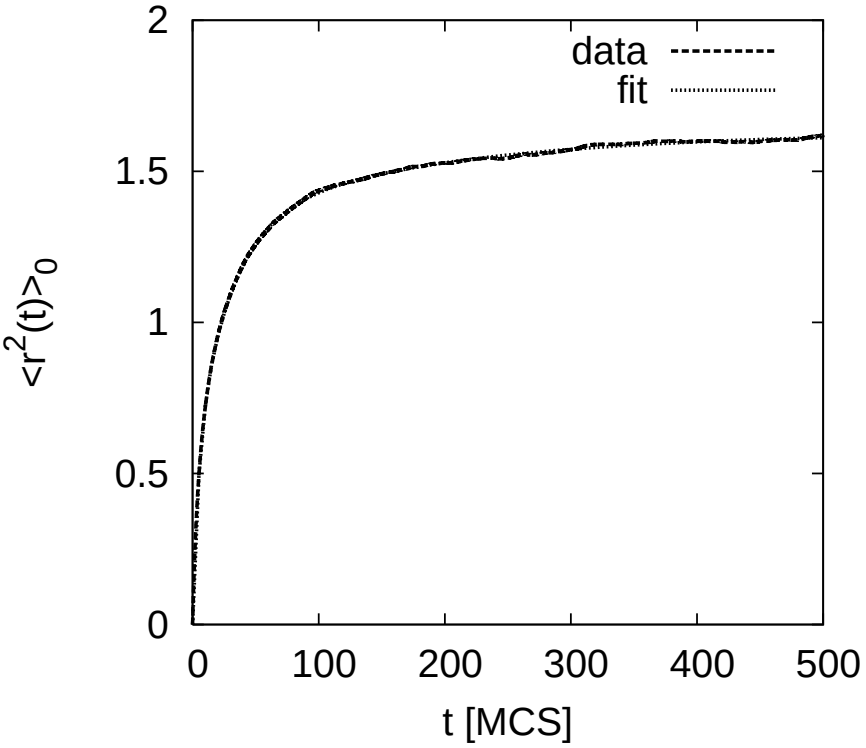

Figure 6.8: Three exponential fit (6.15) of the mean square displacement $\langle r^2(t)\rangle_0$ of a tracer in a frozen network of chains with the length $r = 10$ at a concentration $c = 0.84$ (after [Kar06]).

resembling a power law, in the quantity $D(\omega) - D$ between the high-frequency plateau and the low-frequency behavior $D(\omega) - D \sim \omega^2$. However, its appearance seems to be connected with the percolation transition near c $\simeq 0.75$ induced by the system of frozen chains and the associated anomalous behavior of $\langle r^2(t)\rangle_0$ entering Eq. (6.4). Obviously, the DP-scheme does not account for our findings displayed in Fig. 6.3, where power-law regimes get most pronounced at the highest concentrations. In such cases large-scale rearrangements in the polymer network are expected to be necessary in order to allow the random walker to escape its instantaneous cage. This aspect and the associated memory effects are not taken into account by the DP-scheme contained in Eqs. (6.4) and (6.12).

6.3 Summary and Discussion

Tracer diffusion through dense systems of lattice polymers was studied using the FSB Monte Carlo algorithm. This technique allowed us to concentrate on the high-density regime, where we observe tracer correlation factors f much smaller than unity and strongly dispersive transport. These findings served as a reference in our comparison with corresponding results from DP-theory, with fair agreement between both methods up to moderate densities.

Clearly, the DP-theory requires much less computational effort than full simulations. An earlier study of tracer diffusion through a polymer host within the DP-concept was based on

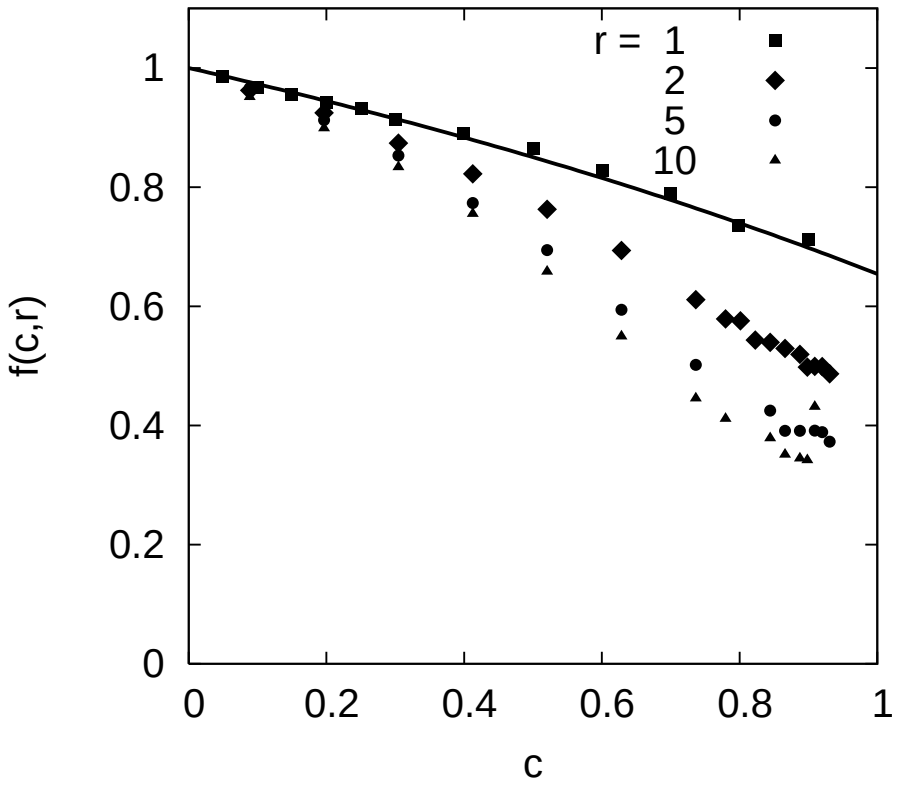

Figure 6.9: Correlation factor f versus concentration c for chain lengths $r = 1, 2, 5$ and 10 as obtained from DP-theory. The full line corresponds to Eq. (6.3) (after [Kar06]).

the Verdier-Stockmayer algorithm for moves of lattice chains and led to an almost quantitative agreement with simulations [Dür02].

The presently used FSB-algorithm allows neighboring beads in a chain to be connected either by vectors parallel to the cubic axis or, in addition, by diagonal vectors of the type $(0, 1, 1)$ on the underlying simple cubic lattice. This introduces two important modifications relative to the standard Verdier-Stockmayer algorithm, which are most easily explained by considering just dimers: (i) when the walker encounters a dimer, screening of the more remote bead by the more adjacent bead becomes less effective in the FSB algorithm. Hence, values for f are decreased in the present case relative to Ref. [Dür02]. This aspect is correctly described by the DP-concept of Section 6.2; (ii) one dimer can simultaneously occupy two nearest-neighbor sites of a tracer. This introduces stronger correlations within the first shell of sites surrounding the tracer. On the other hand, the relation (6.12), which is the basic assumption of our DP-concept applied to polymers, does not account for any correlations among those sites and therefore becomes less reliable in combination with the FSB-algorithm. This may explain part of the deviations between Figs. 6.11 and 6.3.

An improved theory in the DP-spirit therefore should take into account spatial correlations among beads in the nearest-neighbor shell surrounding the tracer. Clearly, the present model of athermal chains is too simple to describe tracer motion in some real material. Nevertheless, the

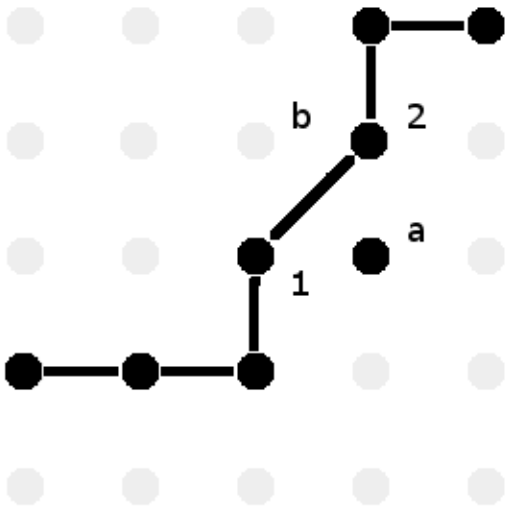

Figure 6.10: Fixed tracer particle (black circle) surrounden by chain monomers (black circles connected by black bonds) in the FSB model. The chain beads 1 and 2 occupy two sites of the first nearest-neighbor shell around the tracer. In the full FSB simulation, the tracer can hop over from site a to site b belonging to the second nearest-neighbor shell.

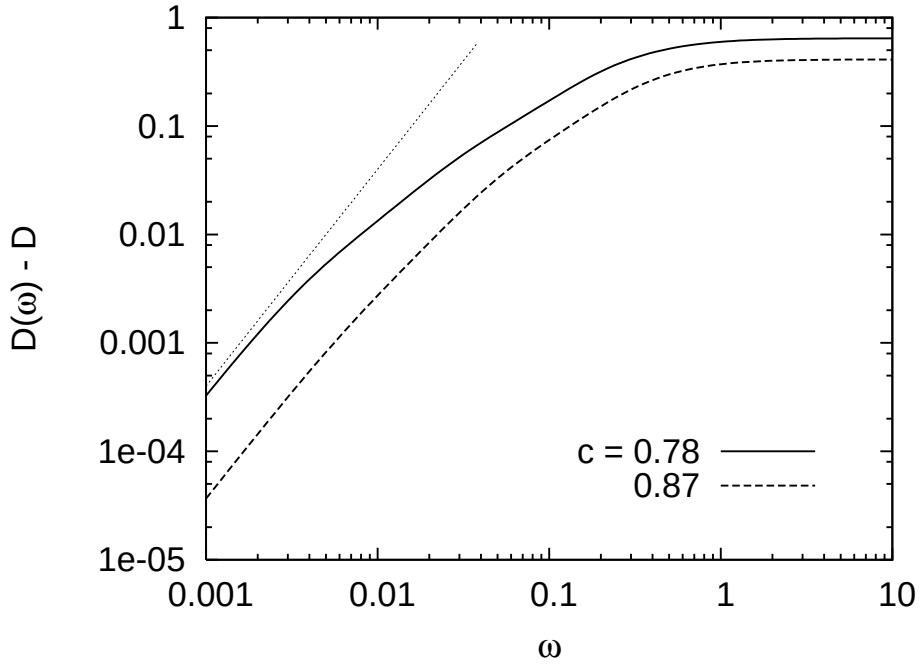

Figure 6.11: Double-logarithmic plot of the frequency-dependent diffusivity according to the DP-scheme for chains of length $r = 10$ and two different concentrations. The dotted straight line corresponds to the low-frequency behavior $D(\omega) - D \sim \omega^2$ (after [Kar06]).

effective power-laws in the time-dependent diffusion constant $D(t)$ obtained from simulations constitute an interesting feature of our model, which may be compared with the anomalous ion diffusion found in recent ac-transport measurements on polymer electrolytes [Mar05] and [Not02]. Contrary to dispersive ion transport in glasses, mainly caused by the disordered energy landscape produced by the glass structure, the present mechanism is based solely on slow rearrangements of free volume, i.e. of sites accessible to the tracer, in cases where the total free volume is small.

7 Summary and Outlook

In this work we explored whether a highly coarse grained representation of diblock copolymer melts within the frame of the Gaussian disphere model (GDM) was capable to capture essential long-time kinetic and dynamic features of copolymer systems in the bulk and in confined geometries.

In this model a diblock copolymer is mapped onto two soft spheres with fluctuating radii of gyration and distance vector between their centers of mass serving as the only internal degrees of freedom of the particle. The input quantities of the model are conditional distribution functions for both the radii and the distance as well as monomer number densities of the two blocks for a given shape of the soft particle. These functions were derived in the previous work of Eurich [Eudiss] within an underlying Gaussian model of the polymer chain and have simple analytical expressions. The kinetics of the system of soft particles was driven by a discrete time Monte-Carlo algorithm.

Firstly the model was tested against bulk properties of diblock copolymer melts. In the disordered melt, formation of A and $B-$ rich regions was observed when increasing the interaction parameter between the two incompatible components of the molecule. Above the order-disorder transition point (ODT), lamellar, cylindrical and bcc structures were found depending on the copolymer composition. The position of the ODT for symmetrical chains was shown to be shifted towards higher values of the interaction parameter when decreasing the polymerization degree. In the strong segregation regime, the lamellar periodicity was shown to scale with the polymerisation degree with the exponent being a little higher than the theoretical prediction [Oht86]. It turned out that the model is less sensitive to finite size effects than lattice chain models for block copolymers. Near the ODT, the motion of the center of mass of the individual particles was found getting suppressed by the microphase ordering so that two-dimensional diffusion was observed in the ordered lamellar phase.

After the model has proved successful in reproducing essential bulk properties of the diblock copolymer systems, microphase separation was studied in thin films. It was shown that the particles' alignment near homogeneous neutral walls induced perpendicular lamellae with a local order throughout the film. When the walls were attractive to one of the component, parallel lamellae were observed to form.

Global order of perpendicular lamellae was achieved when one of the walls was patterned with alternating attractive stripes with the periodicity commensurate to the lamellar periodicity in the bulk. In this case the substrate pattern fully penetrated the film supressing bulk like ordering in the center of the film. The influence of commensurability effects and of the film thickness on the pattern penetration as well as the kinetics of the ordering were studied with the help of the lateral structure factor of one component.

In summary, the soft particle model for diblock copolymers turned out to be an effective and successful tool in describing the microphase separation of dense diblock copolymer melts both in the bulk and film geometries with film thicknesses larger than a few times the radius of gyration.

The model is expected to loss reability when studying ordering processes in thinner films. In this case the assumed sphericity of individual blocks does not account for the molecules' distortion under confinement, where they get compressed in the direction perpendicular to the wall and elongated in the lateral directions. A more reliable description of the molecule could be achieved in the spirit of Eurichs work [Eur02] by allowing ellipsoidal block shapes. With such a model one could take advantage of the fast equilibration times in the GDM, thereby retaining the more detailed description of the ellipsoid model.

In another extension of the model, one could incorporate an additional term in the free energy that suppresses fluctuations of the total monomer density [Mül05b] and hence reduces the compressibility. Further reducing the overall compressibility by that method may turn out advantageous, in particular, in thin films studies.

Moreover, the GDM and extensions thereof in terms of strings of soft spheres may become of interest in a semiquantitative description of more complex molecules, including chain-like segmented or branched copolymers, or copolymers carrying reactive groups [Kra02]. To develop such generalized models and to explore their applicability to more complicated chain structures appearing for amphiphilic block copolymers in solution [Sev05], [Une07] remain a challenging problem.

Finally, aiming at a description of ion transport in polymer electrolytes, diffusion of tracer particles in a dynamically disordered polymer network was studied within the dynamic percolation approach introduced by Druger [Dru85]. The problem is complicated by the fact that the reorganisations of the host medium occur on the same time scale as the tracer hopping which offers another challenge for a coarse grained description. Dürr et al. suggested to split this problem up into two simpler tasks: *i*) the tracer motion in a frozen percolation enviroment and *ii*) determining the waiting time distribution for the first renewal event from local polymer density fluctuations in the vicinity of a frozen tracer [Dür02]. These authors have shown, using the Verdier-Stockmayer algorithm, that up to moderate densities the calculated tracer correlation factors were in good agreement with results from the full simulation.

In the present work a recently developed flucluation site-bond Monte Carlo algorithm was employed which enabled us to test the dynamic percolation approach at higher polymer densities. The method was shown to produce values for the tracer correlation factor substantially smaller than unity, but they were still higher than those obtained in the full simulation. An intermediate regime in the time depedent diffusion constant was found which separated the initial time behavior of this quantity from the long-time behavior and favorably compares with recent experiments on polymer electrolytes [Mar05], [Not02].

A Structure Factor in the Diblock Copolymer Melt

Let us define the Fourier transform of the A-monomer density $\varrho_A(\vec{r})$ in the diblock copolymer melt as

$$\tilde{\varrho}_A(\vec{k}) = \int_V d^3r \varrho_A(\vec{r}) e^{-i\vec{k}\vec{r}}\,, \tag{A.1}$$

with V being the volume of the simulation box with the periodic boundary conditions in three dimensions. The inverse Fourier transform of $\varrho_A(\vec{r})$ is then

$$\varrho_A(\vec{r}) = \int \frac{d^3k}{(2\pi)^3} \tilde{\varrho}_A(\vec{k}) e^{i\vec{k}\vec{r}}\,, \tag{A.2}$$

where the integration is carried out over the first Brillouin zone.

The ordinary 3-d structure factor reads

$$S(\vec{k}) = \frac{1}{MN_A} \left\langle \left| \tilde{\varrho}_A(\vec{k}) \right|^2 \right\rangle = \frac{1}{\varrho_{A,0}} \int_V d^3r \left\langle \varrho_A(\vec{r}) \varrho_A(0) \right\rangle e^{i\vec{k}\vec{r}} \tag{A.3}$$

where the density-density correlation function can also be expressed via the Fourier transform of the structure factor

$$\left\langle \varrho_A(\vec{r}) \varrho_A(0) \right\rangle = \varrho_{A,0} \int \frac{d^3k}{(2\pi)^3} \left\langle \left| \tilde{\varrho}_A(\vec{k}) \right|^2 \right\rangle e^{i\vec{k}\vec{r}}\,. \tag{A.4}$$

Here M is the total number of molecules in the system, N_A the number of A-monomers in the molecule, $\varrho_{A,0} \equiv \frac{MN_A}{V}$ is the mean A-monomer density and one integration in (A.3) is carried out due to translational invariance hold in the disordered melt. Here and below $\langle ... \rangle$ means averaging over all configurations of the system (statistical averaging). For convinience we omit also the symbol A in the structure factor $S(\vec{k})$.

The density $\varrho_A(\vec{r})$ consists of terms caused by individual molecules

$$\varrho_A(\vec{r}) = \sum_{j=1}^{M} \varrho_A^{(j)}(\vec{r} - \vec{r}_j^{\,A} | R_j^A)\,, \tag{A.5}$$

where the conditional monomer density $\varrho_A^{(j)}(\vec{r}|R_j^A)$ of the A-block of the j-th molecule is defined as in Eq. (2.12), which in our case reads

$$\varrho_A^{(j)}\left(\vec{r} - \vec{r}_j^{\,A} | R_j^A\right) = \frac{N_A}{[R_j^A]^3} \left(\frac{3}{2\pi}\right)^{3/2} \exp\left(-\frac{3}{2} \frac{(\vec{r} - \vec{r}_j^{\,A})^2}{[R_j^A]^2}\right)\,, \tag{A.6}$$

with R_j^A being the radius of gyration of the corresponding block and $\vec{r}_j^{\,A}$ the position of its center of mass.

Substitution of (A.5) and (A.6) into the Fourier transform (A.1) produces

$$\tilde{\varrho}_A(\vec{k}) = \sum_{j=1}^{M} \frac{N_A}{[R_j^A]^3} \left(\frac{3}{2\pi}\right)^{3/2} \int d^3 r'_j \exp\left(-\frac{3}{2}\frac{\vec{r}_j^{\,\prime 2}}{[R_j^A]^2}\right) e^{-i\vec{k}(\vec{r}_j' + \vec{r}_j^{\,A})}\,, \tag{A.7}$$

where a new variable $\vec{r}_j^{\,\prime} = \vec{r} - \vec{r}_j^{\,A}$ was introduced.

A Fourier transform of a Gaussian function is again a Gaussian function

$$\int_{-\infty}^{+\infty} dx\, \exp\left(-\frac{x^2}{2\sigma^2}\right) e^{-i\,kx} = \sqrt{2\pi\sigma^2}\exp\left(-\frac{\sigma^2 k^2}{2}\right), \tag{A.8}$$

so that

$$\tilde{\varrho}_A(\vec{k}) = N_A \sum_{j=1}^{M} \exp\left(-\frac{[R_j^A]^2 k^2}{6}\right) e^{-i\,\vec{k}\vec{r}_j^{\,A}}\,. \tag{A.9}$$

Using (A.9) in Eq. (A.4), one can finally obtain for the structure factor

$$S(\vec{k}) = \frac{N_A}{M}\left\langle \sum_{j,l=1}^{M} \exp\left[-\frac{1}{6}\left([R_j^A]^2 + [R_l^A]^2\right) k^2\right] \exp\left(-i\,\vec{k}\left(\vec{r}_j^{\,A} - \vec{r}_l^{\,A}\right)\right)\right\rangle \tag{A.10}$$

Note that according to (A.10), $S(\vec{k}) \sim N_A$, i.e. the number of A-monomers in the molecule. Expression (A.10) was used to calculate the structure factor in section 3.

B Lateral Structure Factor in Slab Geometries

When studying the microphase separation in slab geometries like a system confined between two walls located at $z = 0$ and $z = L_z$ (see section 5), the space correlations of the A-monomer number density $\varrho_A(\vec{r})$ within the plane (x, y) are of interest. In this section we will be concerned with the lateral structure factor $S(\vec{k}_\parallel, z)$ defined as

$$S(\vec{k}_\parallel, z) = C \left\langle \tilde{\varrho}_A(\vec{k}_\parallel, z)\tilde{\varrho}_A(-\vec{k}_\parallel, z)\right\rangle , \tag{B.1}$$

where the quantity $\tilde{\varrho}_A(\vec{k}_\parallel, z)$ is the Fourier transform of $\varrho_A(\vec{r})$ with respect to the cartesian coordinates x and y :

$$\tilde{\varrho}_A(\vec{k}_\parallel, z) = \int_V d^2r_\parallel \varrho_A(\vec{r})e^{-i\vec{k}_\parallel\vec{r}_\parallel} , \tag{B.2}$$

with $\vec{r}_\parallel = (x, y)$, and $\vec{k}_\parallel = (k_x, k_y)$ being two-dimensional vectors, $\vec{r} = (\vec{r}_\parallel, z)$, $\vec{k} = (\vec{k}_\parallel, k_z)$. We define the constant C in Eq. (B.1) in such a way that the lateral structure factor $S(\vec{k}_\parallel, z)$ becomes independent of the slab thickness L_z in the limit $L_z \to \infty$, i.e. for a bulk system. As in the previous section, we omit the symbol A in the notation of $S(\vec{k}_\parallel, z)$.

To determine the constant C, we express the lateral structure factor through the L_z independent full structure factor $S(\vec{k})$, Eq. (A.3). We proceed with the equation

$$\left\langle \tilde{\varrho}_A(\vec{k}_\parallel, z)\tilde{\varrho}_A(-\vec{k}_\parallel, z)\right\rangle = \int d^2r_\parallel \int d^2r'_\parallel \left\langle \varrho_A(\vec{r}_\parallel, z)\varrho_A(\vec{r}'_\parallel, z)\right\rangle e^{-ik_\parallel\left(\vec{r}_\parallel-\vec{r}'_\parallel\right)} . \tag{B.3}$$

Due to the translational invariance of the disordered melt, the quantity $\left\langle \varrho_A(\vec{r}_\parallel, z)\varrho_A(\vec{r}'_\parallel, z)\right\rangle$ is z-independent so that

$$\left\langle \tilde{\varrho}_A(\vec{k}_\parallel, z)\tilde{\varrho}_A(-\vec{k}_\parallel, z)\right\rangle = \int d^2r_\parallel \int d^2r'_\parallel \left\langle \varrho_A(\vec{r}_\parallel - \vec{r}'_\parallel, 0)\varrho_A(0, 0)\right\rangle e^{-ik_\parallel\left(\vec{r}_\parallel-\vec{r}'_\parallel\right)} , \tag{B.4}$$

or using Eq. (A.4)

$$\left\langle \tilde{\varrho}_A(\vec{k}_\parallel, z)\tilde{\varrho}_A(-\vec{k}_\parallel, z)\right\rangle = \int d^2r_\parallel \int d^2r''_\parallel \frac{\varrho_{A,0}}{MN_A} \int \frac{d^3q}{(2\pi)^3} \left\langle |\tilde{\varrho}_A(\vec{q})|^2\right\rangle e^{i\vec{q}\left(\vec{r}''_\parallel,0\right)}e^{-i\vec{k}_\parallel\vec{r}''_\parallel} , \tag{B.5}$$

where $\vec{r}''_\parallel = \vec{r}_\parallel - \vec{r}'_\parallel$ and $\vec{q} = \left(\vec{q}_\parallel, 0\right)$ is a vector in the $d = 3$ k-space.

The last expression can further be modified with the help of $\int d^2r''_\parallel \exp\left(i\left(\vec{q}_\parallel - \vec{k}_\parallel\right)\vec{r}''_\parallel\right) = (2\pi)^2\delta\left(\vec{q}_\parallel - \vec{k}_\parallel\right)$ with $\delta(...)$ being the delta-function which leads to

$$\left\langle \tilde{\varrho}_A(\vec{k}_\parallel, z)\tilde{\varrho}_A(-\vec{k}_\parallel, z)\right\rangle = \frac{1}{L_z}\int_{-\infty}^{\infty} \frac{dk_z}{2\pi} \left\langle \left|\tilde{\varrho}_A(\vec{k}_\parallel, k_z)\right|^2\right\rangle , \tag{B.6}$$

where $A\varrho_{A,0} = M/L_z$ was used with $A = \int d^2r_\parallel$ being the lateral slab surface. Remembering the definition of the full structure factor, see (A.3), we have finally

$$\frac{L_z}{M}\left\langle \tilde{\varrho}_A(\vec{k}_\parallel, z)\tilde{\varrho}_A(-\vec{k}_\parallel, z)\right\rangle = \int_{-\infty}^{\infty}\frac{dk_z}{2\pi}S\left(\vec{k}_\parallel, k_z\right) . \tag{B.7}$$

The right side of the last equation is independent of the slab thickness L_z, which suggests to adopt the definition

$$S(\vec{k}_\parallel, z) = \frac{L_z}{M}\left\langle \tilde{\varrho}_A(\vec{k}_\parallel, z)\tilde{\varrho}_A(-\vec{k}_\parallel, z)\right\rangle . \tag{B.8}$$

for the lateral structure factor for finite L_z; Eq. (B.7) ensures that it becomes L_z-independent in the bulk limit for a given total monomer concentration.

C Directionally Averaged Structure Factor

This appendix deals with the spherical averaging of the structure factor $S(\vec{k})$ defined through the A-monomer density in Eq.(A.3) of Appendix A. The spherically averaged structure factor is widely used in section 3 when studying bulk properties of the diblock copolymers in disordered and ordered states. We will consider sinusoidal modulations of the A-monomer density

$$\varrho_A(\vec{r}) = A\cos\left(\vec{q}\,\vec{r}\right) = \frac{A}{2}\left(e^{i\vec{q}\,\vec{r}} + e^{-i\vec{q}\,\vec{r}}\right) \tag{C.1}$$

where A is the amplitude, $|\vec{q}| \equiv \sqrt{q_x^2+q_y^2+q_z^2} = \frac{2\pi}{\lambda}$, λ the wave length. The Fourier transform Eq. (A.1) of the A-monomer density reads for the modulations of the type (C.1)

$$\tilde{\varrho}_A(\vec{k}) = (2\pi)^3\,\frac{A}{2}\left[\delta(\vec{q}+\vec{k}) + \delta(\vec{q}-\vec{k})\right] . \tag{C.2}$$

The structure factor

$$S(\vec{k}) = \frac{1}{MN_A}\left\langle \tilde{\varrho}_A(\vec{k})\tilde{\varrho}_A(-\vec{k})\right\rangle = (2\pi)^6\left(\frac{A}{2}\right)^2\frac{1}{MN_A}\left[\delta(\vec{q}+\vec{k}) + \delta(\vec{q}-\vec{k})\right] \tag{C.3}$$

shows two delta-like peaks located at $\vec{k} = \pm\vec{q}$. The directional averaging of the structure factor defined as

$$S(k) = \int d^3k'\, S(\vec{k}')\delta\left(k - \sqrt{k_x'^2 + k_y'^2 + k_z'^2}\right) \tag{C.4}$$

leads to

$$S(k) = 2\,(2\pi)^6\left(\frac{A}{2}\right)^2\frac{1}{MN_A}\delta\left(k - |\vec{q}|\right) . \tag{C.5}$$

The spherical averaging of the structure factor eliminates any angle dependence but leaves the delta peak at the same period $q = \sqrt{q_x^2+q_y^2+q_z^2}$.

D Diffusion in the Lamellar Phase

The diffusion of a diplock copolymer molecule in the lamellar phase well ordered along the z-axis can roughly be modelled as a random motion of a point-like Brownian particle in a periodic potential with periodicity L. The diffusion constant of such motion is predicted to obey the following formula

$$D = \frac{D_0}{\left\langle e^{-\beta V_{eff}} \right\rangle \left\langle e^{+\beta V_{eff}} \right\rangle} . \tag{D.1}$$

Here D_0 is the diffusivity in the otherwise homogeneous host medium and $V_{eff} \equiv V_{eff}(z)$ is an effective periodic potential defined via the measured z-dependent density $\varrho(z) = const\ e^{-\beta V_{eff}(z)}$. The brackets $\langle ... \rangle$ mean here an averaging over a period L:

$$\left\langle e^{-\beta V_{eff}} \right\rangle = \frac{1}{L} \int_0^L dz e^{-\beta V_{eff}} . \tag{D.2}$$

Eq. (D.1) is exact for diffusion of one Brownian particle, see [Die77]. It can be used for describing an ensemble of interacting Brownian particles so far as V is considered as a "potential of mean force", i.e. if V is defined through $\varrho(z)$ as above, [Die86]. This concept of introducing an effective potential into the formula for D is an approximation based on a factorization treatment of the many-particle Smoluchowski equation.

Alternatively, we can write

$$D = \frac{D_0}{\langle \varrho(z) \rangle \left\langle \varrho^{-1}(z) \right\rangle} , \tag{D.3}$$

where the prefactors of $\varrho(z)$ cancel.

To make some estimations with (D.3), we will consider the simplest case of a sinusoidal density wave in the z-direction corresponding to weakly segregated lamellar phase

$$\varrho(z) = A + B \cos(k^* z) , \tag{D.4}$$

where $k^* = 2\pi/L$ and $0 < B < A$ are some constants, A is the average value of $\varrho(z)$ and B the amplitude of fluctuations about the average.

Accordingly,

$$\langle \varrho(z) \rangle = A \tag{D.5}$$

and

$$\left\langle \varrho^{-1}(z) \right\rangle = \frac{1}{\pi A} \int_0^\pi \frac{d\phi}{1 + \alpha \cos\phi} , \tag{D.6}$$

where $\alpha = B/A < 1$ and $\phi = k^* z$. With the help of

$$\frac{1}{\pi} \int_0^\pi \frac{d\phi}{1 + \alpha \cos\phi} = \frac{1}{\sqrt{1 - \alpha^2}} \tag{D.7}$$

the diffusion constant (D.3) reads

$$D = D_0\sqrt{1-\alpha^2} \tag{D.8}$$

or finally

$$D = D_0\sqrt{1-(B/A)^2}\,. \tag{D.9}$$

Note that in the limit $B/A \to 1$ where there are almost no particles near the minima in the density, the diffusion coefficient behaves as $D \simeq \sqrt{2\,(1-B/A)}$.

Bibliography

[Aus90] D. Ausserre, D. Chatenay, G. Coulon, and B. Collin, J. Phys. **51**, 2571 (1990).

[Bal91] A. C. Balazs, K. L. Huang, P. McElwain, and J. E. Brady, Macromolecules **24**, 714 (1991).

[Bar91] J.-L. Barrat and G. H. Fredrickson, Macromolecules **24**, 6378 (1991).

[Bas95] J. Baschnagel and K. Binder, Macromolecules **28**, 6808 (1995).

[Bas00a] J. Baschnagel, K. Binder, P. Doruker, A. A. Gusev, O. Hahn, K. Kremer, W. L. Mattice, F. Müller–Plathe, M. Murat, W. Paul, S. Santos, U. W. Suter, and V. Tries, Advances in Polymer Science **152**, 41 (2000).

[Bas00b] J. Baschnagel, K. Binder, and A. Milchev, "Mobility of Polymers Near Surfaces" in *Polymer Surfaces, Interfaces and Thin Films*, ed. A. Karim and S. Kumar, World Scientific, Singapore (2000).

[Bat88] F. S. Bates, J. H. Rosedale, G. H. Fredrickson, and C. J. Glinka, Phys. Rev. Lett. **61**, 2229 (1988).

[Bat99] F. S. Bates and G. H. Fredrickson, Phys. Today **52** (2), 32 (1999).

[Bin81] K. Binder, Z. Phys. B **43**, 119 (1981).

[Bin83] K. Binder, "Critical Behaviour at Surfaces" in *Phase Transitions and Critical Phenomena* **8**, ed. C. Domb and J. L. Lebowitz, London Academic Press (1983).

[Bin91] H. Fried and K. Binder, J. Chem. Phys. **94**, 8349 (1991).

[Bin94] K. Binder, Adv. Pol. Science **112**, 181 (1994).

[Bin95] K. Binder, "Monte-Carlo and Molecular Dynamics Simulations in Polymer Science" (Oxford University Press, 1995), chapter 1.

[Böl98] M. Böltau, S. Walheim, J. Mlynek, G. Krausch, and U. Steiner, Nature **391**, 877 (1998).

[Bol01] P. G. Bolhuis, A. A. Louis, J. P. Hansen, and E. J. Meijer, J. Chem. Phys. **114**, 4296 (2001).

[Bra94] A. J. Bray, Adv. Phys. **43**, 357 (1994).

[Cha91] A. Chakrabarty, R. Toral, and J. G. Gunton, Phys. Rev. A **44**, 6503 (1991).

[Cha98] A. Chakrabarti and H. Chen, J. Polym. Sci. B **36**, 3127 (1998).

[Cou90] G. Coulon, B. Collin, D. Ausserre, D. Chatenay, and T. P. Russell, J. Phys. **51**, 2801 (1990).

[Die77] W. Dieterich, I. Peschel, and W. Schneider, Z. Phys. B **27**, 177 (1977).

[Die85] W. Dieterich, J. Stat. Phys. **39**, 583 (1985).

[Die86] U. Thomas and W. Dieterich, Z. Phys. B: Condens. Matter **62**, 287 (1986).

[Doi96] M. Doi, "Introduction to polymer physics" Clarenden Press, Oxford (1996).

[Dru85] S. D. Druger, M. A. Ratner, and A. Nitzan, Phys. Rev. B **31**, 3939 (1985).

[Dru88] S. D. Druger and M. A. Ratner, Phys. Rev. B **38**, 12589 (1988).

[Dür02] O. Dürr, T. Volz, and W. Dieterich, J. Chem. Phys. **117**, 441 (2002).

[Dür04] O. Dürr, W. Dieterich, and A. Nitzan J. Chem. Phys. **121**, 12732 (2004).

[Edw05] E. W. Edwards, M. P. Stoykovich, M. Mller, H. H. Solak, J. J. De Pablo, and P. F. Nealey, J. Polym. Sci., Part B: Polym. Phys. **43**, 3444 (2005).

[Eur01] F. Eurich and P. Maass, J. Chem. Phys. **114**, 7655 (2001).

[Eur02] F. Eurich, P. Maass, and J. Baschnagel, J. Chem. Phys. **117**, 4564 (2002).

[Eudiss] F. Eurich, "Coarse-grained models for the kinetics of polymeric systems", thesis, Universität Konstanz (Verlag im Internet GmbH, Berlin, 2002).

[Fel68] W. Feller, "An Introduction to Probability Theory and Its Applications", Wiley, New York, Vol. 2, p. 369 (1998).

[Fis98] H. P. Fischer, P. Maass, and W. Dieterich, Europhys. Lett. **4**2, 49 (1998); Phys. Rev. Lett. **7**9, 893 (1997).

[Flo50] P. J. Flory and W. R. Krigbaum, J. Chem. Phys. **1**8, 1086 (1950).

[Fre87] G. H. Fredrickson and E. Helfand, J. Chem. Phys. **87**, 697 (1987).

[Geh92] M. D. Gehlsen, J. H. Rosedale, F. S. Bates, C. D. Wignall, and K. Almdal, Phys. Rev. Lett. **68**, 2452 (1992).

[deGen] P. G. de Gennes, "Scaling Concepts in Polymer Physics", Cornell University Press (1988).

[Gra91] F. M. Gray, Solid Polymer Electrolytes, VCH Publishers, New York, 1991.

[Gre96] G. S. Grest, M.-D. Lacasse, K. Kremer, and A. M. Gupta, J. Chem. Phys. **105**, 10583 (1996).

[Gro98] R. D. Groot and T. J. Madden, J. Chem. Phys. **108**, 8713 (1998).

[Gro99] R. D. Groot, T. J. Madden, and D. J. Tildesley, J. Chem. Phys. **110**, 9739 (1999).

[Gus93] A. A. Gusev, S. Arizzi, and U. W. Suter, J. Chem. Phys. **99**, 2221 (1993).

[Hab00] C. Haber, S. A. Rulz, and W. Wirtz, PNAS **97**, 10792 (2000).

[Ham99] I. W. Hamley, J. P. A. Fairclough, A. J. Ryan, S.-M. Mai, and C. Booth, Phys. Chem. **1**, 2097 (1999).

[Har98] C. Harrison, M. Park, P. Chaikin, R. A. Register, D. H. Adamson, and N. Yao, Macromolecules **31**, 2185 (1998).

[Hei97] J. Heier, E. J. Kramer, S. Walheim, and G. Krausch, Macromolecules **30**, 6610 (1997).

[Hei99] J. Heier, J. Genzer, E. J. Kramer, F. S. Bates, S. Walheim, and G. Krausch, J. Chem. Phys. **111**, 11101 (1999).

[Hei00] J. Heier, E. J. Kramer, J. Groenewold, and G. F. Fredrickson, Macromolecules **33**, 6060 (2000).

[Hof97a] A. Hoffmann, J.-U. Sommer, and A. Blumen, J. Chem. Phys. **106**, 6709 (1997).

[Hof97b] A. Hoffmann, J.-U. Sommer, and A. Blumen, J. Chem. Phys. **107**, 7559 (1997).

[Hua98] E. Huang, T. P. Russell, C. Harrison, P. M. Chaikin, and R. A. Register, Macromolecules **31**, 7641 (1998).

[Hua99] E. Huang, S. Pruzinsky, T. P. Russel, J. Mays, and C. J. Hawker, Macromolecules **32**, 5299 (1999).

[Kan90] M. G. Kanatzidis, Chem. Eng. News, **68**, 36 (1990).

[Kar06] B. M. Schulz, A. Karatchentsev, M. Schulz, and W. Dieterich, J. Noncryst. Solids, **352**, 5136 (2006).

[Kar07] F. Eurich, A. Karatchentsev, J. Baschnagel, W. Dieterich, and P. Maass, J. Chem. Phys. **127**, 134905 (2007).

[Kel96] G. J. Kellogg, D. G. Walton, A. M. Mayes, P. Lambooy, and T. P. Russel, Phys. Rev. Lett. **76**, 2503 (1995).

[Kho94] A. Y. Grosberg and A. R. Khokhlov, "Statistical Physics of Macromolecules", AIP Press, New York (1994).

[Kon95] N. Koneripally, N. Singh, R. Levicky, F. S. Bates, P. D. Gallapher, and S. K. Satija, Macromolecules **28**, 2897 (1995)

[Kra02] I. Krakovsky, J. Plestil, J. Baldrian, and M. Wübbenhorst, Polymer **43**, 4989 (2002).

[Kre01] T. Kreer, J. Baschnagel, M. Mueller, and K. Binder, Macromolecules **34**, 1105 (2001).

[Kuh34] W. Kuhn, Kolloid-Zeitschrift **68**, 2 (1934).

[Lam94] P. Lambooy, T. P. Russel, G. J. Kellogg, A. M. Mayes, P. D. Callagher, and S. K. Satija, Phys. Rev. Lett. **76**, 2899 (1995).

[Lee02] J. J. deJonge, A. van Zon, and S. W. de Leeuw, Solid State Ionics **147**, 349 (2002).

[Lei80] L. Leibler, Macromolecules **13**, 1602 (1980)

[Lik01] C. N. Likos, Physics Reports **348**, 267 (2001).

[Lud05] S. Ludwigs, G. Krausch, R. Magerle, A. V. Zvelindovsky, and G. Sevink, Macromolecules **38**, 1859 (2005).

[Man97] P. Mansky, T. P. Russell, C. J. Hawker, J. Mays, D. C. Cook, and S. K. Satija, Phys. Rev. Lett. **79**, 237 (1997).

[Mar05] M. Marzantowicz, J. R. Dygas, and W. Jenninger, I. Alig, Solid State Ionics **176**, 2115 (2005).

[Mas06] Y. Masubuchi, G. Ianniruberto, F. Greco, and G. Marruccci, J. Noncryst. Solids, **352**, 5001 (2006).

[Mat02] M. W. Matsen, J. Phys.: Condens. Matter **14**, R21 (2002).

[Mül05a] M. Müller and F. Schmid, Adv. Polym. Sci. **185**, 1 (2005).

[Mül05b] M. Müller and G. D. Smith, J. Polym. Sci., Part B: Polym. Phys. **43**, 934 (2005).

[Mur98a] M. Murat and K. Kremer, J. Chem. Phys. **108**, 4340 (1998).

[Mur98b] M. Murat, G. S. Grest, and K. Kremer, Europhys. Lett. **42**, 401 (1998).

[Mur99] M. Murat, G. S. Grest, and K. Kremer, Macromolecules **32**, 595 (1999).

[Nak80] K. Nakazato and K. Kitahara, Prog. Theor. Phys. **64**, 2261 (1980); R. A. Tahir-Kheli and R. J. Elliot, Phys. Rev. B **27**, 844 (1983), W. Dieterich, J. Stat. Phys. **39**, 583 (1985).

[Not02] V. Di Noto and M. Vittadello, Solid State Ionics **147**, 309 (2002).

[Oht86] T. Ohta and K. Kawasaki, Macromolecules **19**, 2621 (1986).

[Oon90] M. Bahiana and Y. Oono, Phys. Rev. A **41**, 6763 (1990).

[Pet98] D. Petera and M. Muthukumar, J. Chem. Phys. **109**, 5101 (1998).

[Pur97] S. Puri and H. L. Frisch, J. Phys.: Condens. Matter **9**, 2109 (1997).

[Rad96] L. H. Radzilowski, B. L. Carvalho, and E. L. Thomas, J. Polym. Sci. B **34**, 3081 (1996).

[Roc99] L. Rockford, Y. Liu, P. Mansky, T. P. Russell, M. Yoon, and S. G. J. Mochrie, Phys. Rev. Lett. **82**, 2602 (1999).

[Schu05] B. M. Schulz and M. Schulz, New J. Phys. **7**, 231 (2005).

[Schu02] A. J. Schultz, C. K. Hall, and J. Genzer, J. Chem. Phys. **117**, 10329 (2002).

[Sev05] G. J. A. Sevink and A. V. Zvelindovsky, Macromolecules **38**, 7502 (2005).

[Sol71] K. Solc, J. Chem. Phys. **5**5, 335 (1971).

[Sko98] T. A. Skotheim, R. L. Elsenbaumer, and J. F. Reynolds, "Handbook of Conducting Polymers", 2nd Ed., Dekker New York (1998).

[Sto03] S. O. Kim, H. H. Solak, M. P. Stoykovich, N. F. Ferrier, J. J. de Pablo, and P. F. Nealey, Nature **424**, 411 (2003).

[Tah83] R. A. Tahir–Kheli and R. J. Elliott, Phys. Rev. B **27**, 844 (1983).

[Tag93] H. Tang, I. Szleifer, and S. K. Kumar, J. Chem. Phys. **100**, 5367 (1993).

[Thu00] T. Thurn-Albrecht, R. Steiner, J. DeRouchey, C. M. Stafford, and E. Huang, Adv. Mater. **12**, 787 (2000).

[Zon01] A. van Zon and S. W. de Leeuw, Elechtrochim. Acta **46**, 1539 (2001).

[Yab04] G. Yabenko, E. I. Sambriski, M. A. Nemirovskaya, and M. Guenza, Phys. Rev. Lett. **93**, 257803 (2004).

[Yab05] G. Yabenko, E. I. Sambriski, and M. Guenza, J. Chem. Phys. **122**, 054907 (2005).

[Yan00] X. M. Yang, R. D. Peters, and P. F. Nealey, Macromolecules **33**, 9575 (2000).

[Une07] T. Uneyama, J. Chem. Phys. **126**, 114902 (2007).

[Ver62] P. H. Verdier and W. M. Stockmayer, J. Chem. Phys. **36**, 227 (1962).

[Wal94] D. G. Walton, G. J. Kellogg, A. M. Mayes, P. Lambooy, and T. P. Russell, Macromolecules **27**, 6225 (1994).

[Wan97] H. Wang, P. K. Kesani, N. P. Balsara, and B. Hammouda, Macromolecules **30**, 982 (1997)

[Wan00a] Q. Wang, Q. Yan, P. F. Nealy, and Juan J. de Pablo, J. Chem. Phys. **112**, 450 (2000).

[Wan00b] Q.Wang, Q. L. Yan, P. F. Nealey, and J. J. de Pablo, Macromolecules **33**, 4512 (2000).

Last Not Least...

Here I would like to thank all people who contributed to the success of this work.

Prof. Dr. Wolfgang Dieterich for a lot of confidence, for the supervision during my PhD work and for the valuable advices he always gave me. Also I would like to thank him for giving me an opportunity to do this PhD work in his group and the nice working atmosphere.

Prof. Dr. Philipp Maass for an interesting target setting and the fruitful discussions.

Dr. Frank Eurich for detailed information about his computer program and stimulating discussions.

Prof. Dr. Georg Maret and the International Graduate College for the financial support of my work as well as the possibility to take part in the conferences and IGK workshops in Grenoble and Strasbourg.

Prof. Dr. Jorg Baschnagel for hospitality during my stay in Strasbourg.

Our system administrators Stefan Heinrichs, Stefan Gerlach and Juan Zagorodny for maintaining the cluster.

Wittawas Manomaiwong for the program for virtualization of isosurfaces.

All people from P8 for a good time.

My mother and my wife for their support during all these years.